3-2022

Thermal Considerations for Film Cooling Materials With Anisotropic Thermal Conductivity

Carol E. Bryant

THERMAL CONSIDERATIONS FOR FILM COOLING MATERIALS WITH ANISOTROPIC THERMAL CONDUCTIVITY

DISSERTATION

Carol E. Bryant, Captain, USAF

AFIT-ENY-DS-22-M-281

DEPARTMENT OF THE AIR FORCE
AIR UNIVERSITY
AIR FORCE INSTITUTE OF TECHNOLOGY

Wright-Patterson Air Force Base, Ohio

AFIT-ENY-DS-22-M-281

THERMAL CONSIDERATIONS FOR FILM COOLING MATERIALS WITH ANISOTROPIC THERMAL CONDUCTIVITY

DISSERTATION

Presented to the Faculty

Department of Aeronautics and Astronautics

Graduate School of Engineering and Management

Air Force Institute of Technology

Air University

Air Education and Training Command

In Partial Fulfillment of the Requirements for the

Degree of Doctor of Philosophy in Aeronautical Engineering

Carol E. Bryant, BS, MS

Captain, USAF

March 2022

AFIT-ENY-DS-22-M-281

THERMAL CONSIDERATIONS FOR FILM COOLING MATERIALS WITH ANISOTROPIC THERMAL CONDUCTIVITY

Carol E. Bryant, BS, MS
Captain, USAF

Committee Membership:

Lt Col James L. Rutledge, PhD
Chair

Dr. Marc D. Polanka
Member

Dr. Marina B. Ruggles-Wrenn
Member

Maj Peter A. Saunders, PhD
Member

Dr. Andrew T. Lethander
Member

Abstract

Higher performance requirements and reduced core sizes are driving increases in turbine inlet temperature in gas turbine engines, surpassing the melting point of advanced materials. Because engines are getting hotter, newer materials, such as composites, are being introduced into the hot sections of gas turbine engines. Components in the hot section use film cooling to prevent melting. One unique aspect of some high-temperature composites is they have a bulk anisotropic thermal conductivity, therefore heat flow differs relative to traditional metallic components. Film cooling designs can be revolutionized by leveraging anisotropy in high-temperature materials. The purpose of this research is to examine thermal considerations for using materials with anisotropic thermal conductivity in film cooling designs.

There are three primary areas of study. The first examines anisotropy and its effect on a film cooling design. The next seeks to understand how to leverage anisotropy to improve cooling effectiveness. The last area of research is scaling anisotropic overall cooling effectiveness results obtained in a laboratory to engine conditions. The objectives are accomplished by computational fluid dynamics simulations on a film cooled flat plate and leading edge. A ceramic matrix composite material was used to represent anisotropic materials. Results show that leveraging anisotropy in film cooling designs can improve cooling effectiveness without changing any other aspect of the cooling architecture. The research also identifies ideal laboratory conditions and materials for well-scaled, film cooled experiments using isotropic and anisotropic material.

Acknowledgments

First and foremost, thank you to Lt Col Jay Rutledge for leading me through this research. Many thanks to AFRL/RQTT for sponsoring this project and to Dr. John Clark for use of his HIT funding. Dr. Andy Lethander, Natalia Posada, and Aaron Brown were invaluable in guiding me through all manner of testing. Thank you to Dr. Rolf Sondergaard and Dr. Chris Marks in RQTT for HPC hours. Brian Crabtree, Dean Harshman, and the entire AFIT shop deserve a huge thank you for creating my test articles. Thanks to RQX for their expertise: Dr. Allan Katz, Dr. George Jefferson, and Donna Ballard. Thank you to our industry partners for the material and technical expertise. And finally thank you to Capt Connor Weise, Capt Jacob Fischer, Capt Luke McNamara, Lt Col Matt Fuqua, and Marta Kernan for code, CAD, shared research, and more.

Carol Bryant

Table of Contents

Page

Nomenclature

ACR	=	advective capacity ratio, $c_{p,c}\rho_c U_c / c_{p,\infty}\rho_\infty U_\infty$
Bi	=	Biot number, hL/k_s
C	=	nondimensional parameter define in Eq. (6.2)
c_p	=	specific heat at constant pressure (J/kg-K)
D	=	leading edge diameter, (m)
d	=	hole diameter, (m)
DR	=	density ratio, ρ_c/ρ_∞
f	=	frequency (Hz)
h	=	heat transfer coefficient, (W/m^2-K)
I	=	momentum flux ratio, $\rho_c U_c^2/\rho_\infty U_\infty^2$
IR	=	infrared
k	=	thermal conductivity (W/m-K)
L	=	length, (m)
M	=	blowing ratio, $\rho_c U_c/\rho_\infty U_\infty$
NRMSD	=	Normalized residual mean standard deviation, $\sqrt{\frac{r_{Pr_c}^2+r_{Re_c}^2+r_{Pr_\infty}^2+r_\xi^2}{4}}$
Nu	=	Nusselt number, hL/k_f
P	=	pressure (Pa)
Pr	=	Prandtl number, $\mu c_p/k$
q	=	heat flux, (W/m^2)
Re	=	Reynolds number, $\rho U d/\mu$
r	=	radial surface distance, (m)

r = residual, $(y_{lab} - y_{eng})/y_{eng}$

St = Stanton number, $h/\rho U c_p$

s = surface distance from centerline, (m)

T = temperature, (K)

t = thickness, (m)

V = velocity (m/s)

VR = velocity ratio, U_c/U_∞

x = surface distance downstream, (m)

y = distance normal to surface into fluid, (m)

z = spanwise distance from hole centerline, (m)

Greek symbols

α = thermal diffusivity, (m^2/s)

β = angular spacing, (deg)

γ = injection angle, (deg)

$\Delta\phi$ = change in overall effectiveness, $(T_{s,baseline} - T_{s,modified}) \,/\, (T_\infty - T_c)$

ζ = local distance downstream oriented with material layers, (m)

ξ = χ scaling parameter, $\mu_\infty c_{p,\infty}/k_c$

η = adiabatic effectiveness, $(T_\infty - T_{aw})/(T_\infty - T_c)$

η = local distance perpendicular to material layers, (m)

v = spanwise distance oriented with material layers, (m)

μ = dynamic viscosity (N-s/m^2)

ν = vertical pitch between holes, (m)

θ	=	angular distance, (rad)
θ	=	nondimensional temperature, $(T_\infty - T)/(T_\infty - T_c)$
ρ	=	density (kg/m^3)
σ	=	standard deviation
ϕ	=	overall effectiveness, $(T_\infty - T_s)/(T_\infty - T_c)$
χ	=	coolant warming factor, $(T_\infty - T_{c,e})/(T_\infty - T_{c,i})$

Subscripts

0	=	without film cooling
∞	=	freestream
aw	=	adiabatic wall
c	=	coolant
e	=	exit
f	=	fluid
i	=	internal
LE	=	leading edge
ref	=	reference
s	=	surface
w	=	wall

This page is intentionally left blank

THERMAL CONSIDERATIONS FOR FILM COOLING MATERIALS WITH ANISOTROPIC THERMAL CONDUCTIVITY

1. Introduction

1.1. General Issue

The design of the next generation of gas turbine engines is being driven by the need for smaller engines that operate at higher temperatures. The need for a higher overall pressure ratio (OPR) reduces core size and increases the turbine inlet temperature, leading to higher temperatures in key parts. Temperatures in the hot section of an engine surpass the melting temperatures of every metallic alloy. Complex, proprietary cooling schemes deliver pressurized coolant to keep the exotic alloys from melting. However, the coolant air used bypasses the combustor, thereby decreasing engine performance. The goal for designers is to maximize turbine inlet temperature and minimize coolant bleed air.

Newer materials such as ceramic matrix composites (CMC) have much higher melting points than traditional metallic alloys, as well as high strength and creep resistance. Many engine companies such as General Electric [1], Rolls-Royce [2], Safran [3], and Honeywell [4] are heavily investing in research and development of ceramic composite materials for their engines. CMCs offer many performance advantages and have been tested at temperatures up to 1750 K, well above the melting point of Inconel 718, a nickel alloy commonly used for turbine components [5]. Even with high-temperature capabilities, many CMC parts will need to be cooled.

Bleed air cooling is accomplished via a complex system of internal and external cooling. Internal cooling methods cool the underside of a component by conducting heat through the material and result in a temperature reduction on the external surface. External or film cooling

protects the surface from the hot freestream gases by forming a protective layer of cool air on the surface.

CMCs are made by weaving fiber tows together into a fabric, stacking layers of fabric, and infiltrating them with a matrix. The result is a material made of several layers with high thermal conductivity, held together by a matrix with lower thermal conductivity. Therefore, a CMC part conducts heat differently from an identical part made from a metallic alloy. One underlying norm in cooling designs is the material used is isotropic, however composite materials have anisotropic thermal conductivity. Anisotropic k has not been considered a part of the design space. The optimal cooling design for a CMC part should consider this unique aspect. Additionally, it is difficult to conduct experiments at low temperatures that correctly predict the temperature of engine components with anisotropic thermal conductivity. There are multiple aspects of this problem that must be investigated to improve the fidelity of these temperature predictions.

1.2. Investigative Questions

Engineers who design film cooling schemes have several factors that can vary to produce the highest overall cooling effectiveness on a component. Coolant feed direction, backside impingement, hole placement, hole type, hole shape, and roughness are just a few of the myriad of knobs a designer can adjust to increase the coolant's effectiveness. Another tool can be added to this design space: thermal conductivity. To understand how anisotropy can be leveraged in film cooling, several questions must be answered.

1. **What is the effect of anisotropic thermal conductivity on a film cooled part?**

   First and foremost, the differences between isotropic and anisotropic parts must be identified. It must be shown that there is a meaningful difference for thermal management between heat conduction in a composite component compared to a metallic component.

2. **How can the thermal conductivity of a material be changed to improve the overall cooling effectiveness?**

   Next, it is necessary to understand how anisotropy can be leveraged to improve film cooling designs. The entire design space should be explored so the advantages and disadvantages of changing a material's thermal conductivity are understood.

3. **How do the results of a film cooling study of a CMC conducted at laboratory conditions scale to engine conditions?**

   Finally, it is also necessary to know how overall cooling effectiveness scales in anisotropic materials. The results of laboratory experiments must be scaled to gas turbine relevant conditions, or they are useless to a film cooling design. This is an area not well understood with isotropic materials either.

The answers to these three investigative questions are accomplished through the research objectives.

1.3. Research Objectives

The goal of this research is to examine thermal considerations for using materials with anisotropic thermal conductivity in film cooling applications. To accomplish this goal the following objectives have been set.

1. Characterize the effects of anisotropic thermal conductivity on overall cooling effectiveness.
2. Determine methods to increase the overall cooling effectiveness by varying the thermal conductivity tensor.
3. Identify scaling parameters and testing methodology for overall effectiveness experiments with isotropic and anisotropic thermal conductivity.

These objectives have been accomplished in the present work using analysis and computational fluid dynamics (CFD) simulations. By accomplishing these objectives, designers will have a better understanding of how anisotropic thermal conductivity affects the cooling of CMC parts. Each objective is described in detail in the chapters following the literature review. The chapters themselves are organized around research efforts instead of individual objectives. Each research effort answers a unique and different aspect of the objectives.

2. Literature Review

The research objectives occur at the intersection of three separate areas of research: gas turbine cooling, ceramic matrix composites, and anisotropic thermal conductivity. The purpose of this section is to provide a background into all three separate areas as well as their intersections.

2.1. Gas Turbine Cooling

The outcomes of this research can be applied to any application with film cooling: high-speed propulsion, gas turbine engines, and more. However, to ensure that the research is focused, the spotlight is on components in the hot section of gas turbine engines as the primary application and environment for this study.

Gas turbine engines employ cooling in many areas such as the combustor liner, turbine vanes and rotors, and end walls. In most places, both internal and external cooling occurs. Internal cooling refers to cooling from impingent or convection along a surface, like the inside walls or hole walls. External cooling refers to cooling from the film formed by the coolant ejected from the cooling holes mixing with the freestream along the top surface of the material.

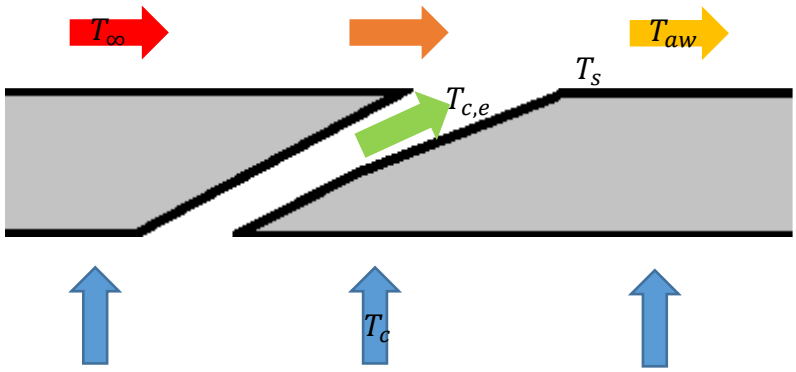

Figure 1. Simple cooling hole geometry showing internal and external cooling and various temperatures.

2.1.1. Overall Effectiveness

As shown in Figure 1, film cooling decreases the temperature of the fluid directly above the material. Areas covered by the coolant film are cooler than exposed areas. This process is described by Newton's Law of Cooling:

$$q'' = h(T_{aw} - T_s) \tag{2.1}$$

where q'' is the heat flux, h is the convective heat transfer coefficient, T_{aw} is the adiabatic wall temperature and T_s is the temperature of the surface. The adiabatic wall temperature is defined as the fluid temperature immediately above the surface for an adiabatic surface [6]. Conversely, overall effectiveness, ϕ, is the nondimensional surface temperature of film cooled, conducting part and characterizes the overall reduction of the surface temperature from all forms of cooling, including internal and film cooling. It is defined as

$$\phi = \frac{T_\infty - T_s}{T_\infty - T_c} \tag{2.2}$$

where T_s is the temperature of the outside surface, T_∞ is the freestream fluid temperature, and T_c is the temperature of the coolant at the inlet of the cooling passages. For the ϕ distribution measured on a wind tunnel model to match the engine component of interest, several requirements must be satisfied. Albert et al. [7] showed that ϕ is dependent on several factors through a simplified one-dimensional analysis, which follows. The analysis assumes one-dimensional, steady-state heat transfer through a plane wall, as shown in Figure 2, adapted from Ref. [8]. The temperature of the hot film is the adiabatic film temperature T_{aw}, the temperature of any point on the surface is unknown T, and the temperature on the inner surface is T_1. The two convection coefficients are h on the outside surface and h_i on the inner surface. The thickness of

the wall is L. Finally, the heat flux through the entire system is equal and independent of x because the system is at steady-state and there are no additional heat sources or sinks.

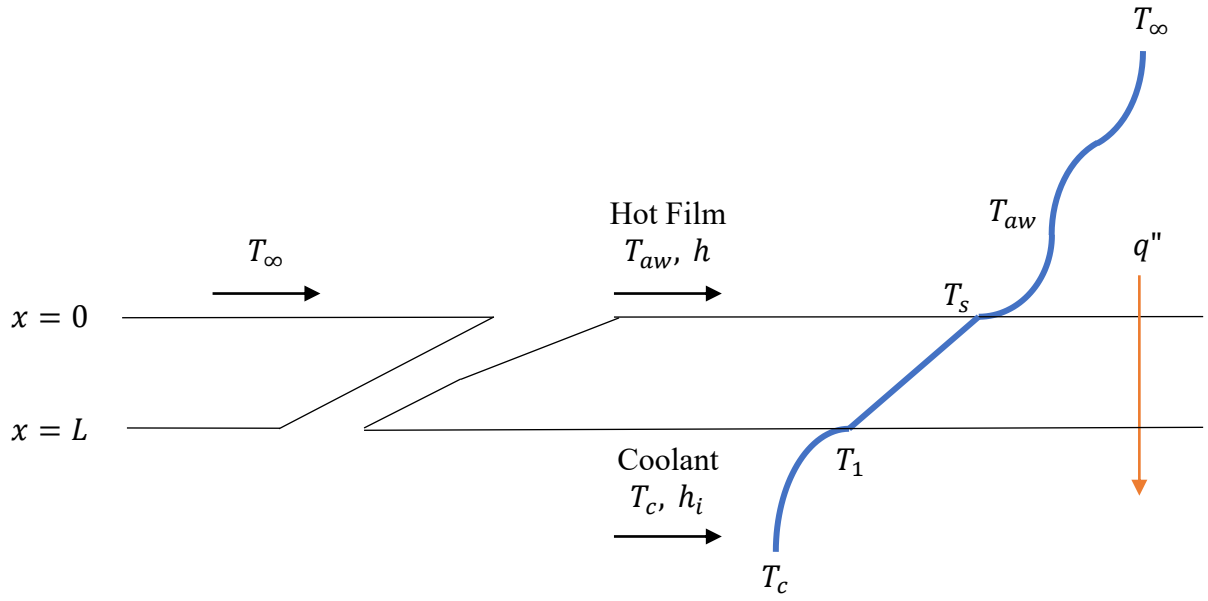

Figure 2: One-dimensional heat transfer through a wall, adapted from [8]

Starting with Fourier's Law, the conduction heat transfer through the wall is $q_w^{''}$

$$q_w^{''} = -k\frac{dT}{dx} = \frac{k}{L}(T_s - T_1) \tag{2.3}$$

where k is the thermal conductivity of the wall. For the two walls with convection, Newton's Law of Cooling is

$$q_f^{''} = h(T_{aw} - T_s) \tag{2.4}$$

$$q_i^{''} = h_i(T_1 - T_c) \tag{2.5}$$

where $q_f^{''}$ is the fluid heat transfer and $q_i^{''}$ is the internal heat transfer. Note that the temperature of the film is the temperature of the adiabatic wall, due to mixing between the freestream and the film. Next, the scaling parameter ϕ depends on are derived in terms of the temperatures shown in Eq. 2.3-2.5. To start, the heat flux due to convection on the film surface is set equal to the conduction heat flux. This derives the Biot number, Bi

$$q_f^{"} = q_w^{"} \tag{2.6}$$

$$h(T_{aw} - T_s) = \frac{k}{L}(T_s - T_1) \tag{2.7}$$

$$\frac{(T_s - T_1)}{(T_{aw} - T_s)} = \frac{hL}{k} \equiv Bi \tag{2.8}$$

The Biot number is the ratio of conductive to convective thermal resistance. Next, the heat fluxes on the inner and film surfaces are equated to define the ratio of heat transfer coefficients, h/h_i

$$q_f^{"} = q_i^{"} \tag{2.9}$$

$$\frac{h}{h_i} = \frac{(T_1 - T_c)}{(T_{aw} - T_s)} \tag{2.10}$$

The definitions of coolant warming, χ, and adiabatic effectiveness, η, are also needed

$$\chi = \frac{T_\infty - T_{c,e}}{T_\infty - T_c} \tag{2.11}$$

$$\eta = \frac{T_\infty - T_{aw}}{T_\infty - T_{c,e}} \tag{2.12}$$

where $T_{c,e}$ is the temperature of the coolant as it exits the film cooling holes. This temperature drops out if the two parameters are multiplied.

$$\chi\eta = \frac{T_\infty - T_{aw}}{T_\infty - T_c} \tag{2.13}$$

Next, these terms are used to write overall effectiveness, ϕ, in terms of $\frac{h}{hi}, Bi, \chi$, and η.

$$\phi - \chi\eta = \frac{T_{aw} - T}{T_\infty - T_c} \tag{2.14}$$

$$1 - \chi\eta = \frac{T_{aw} - T_c}{T_\infty - T_c} \tag{2.15}$$

$$1 + Bi + \frac{h}{h_i} = \frac{T_{aw} - T_c}{T_{aw} - T} \tag{2.16}$$

Finally, these terms are combined and reduced to find ϕ for one-dimensional, steady-state, film cooling.

$$\phi = \frac{\chi\eta\left(Bi + \frac{h}{h_i}\right) + 1}{\frac{h}{h_i} + Bi + 1} \tag{2.17}$$

While Eq. (2.17) generally cannot be directly applied to real turbines given the equation's limitation to one-dimensional heat transfer, the equation does correctly identify the relevant nondimensional parameters that must be matched in a more general three-dimensionally relevant geometry. According to Eq. (2.17), four parameters must be matched between two conditions to have identical ϕ in the two conditions: adiabatic effectiveness, η, the coolant warming factor, χ, the Biot number, Bi, and the ratio of the external to internal heat transfer coefficients, $\frac{h}{h_i}$. None of these can be set directly by the experimentalist since they are all functions of the flow behavior thus careful experimental design is required. It is exceedingly difficult to match all four parameters at laboratory conditions. Next, each of these four parameters is examined in greater detail.

2.1.1.1. Adiabatic Effectiveness

As previously discussed, adiabatic effectiveness is one way to quantify how effective the film is at cooling the surface. η is a nondimensional parameter, so it can be scaled from laboratory to engine conditions, assuming that other flow physics are also scaled. The adiabatic film effectiveness only considers the effect the film has on cooling the outside surface and is therefore commonly used to compare different cooling hole configurations and the film cooling literature is replete with contour plots of η for various turbine geometries and flow conditions.

The study of the intricacies of matching η dates several decades with most focus on the selection of the proper coolant flow rate because the density of the coolant is substantially greater than that of the hot freestream gas in an engine environment. The problem has primarily surrounded the matter of selection of the proper coolant flowrate and the necessary properties of the coolant. Numerous studies have examined matching η by scaling the nondimensional coolant flow rate. There are a variety of ways to select coolants, coolant temperatures, and quantify the coolant flow rate for one geometry. The density ratio (*DR)* [9] is the ratio of the coolant density, ρ_c, to the freestream density, ρ_∞. Other parameters use the velocity to scale the flow such as the velocity ratio (*VR*) [10], the blowing ratio (*M*) [6], and the momentum ratio (*I*) [11], where V_c is the coolant velocity and V_∞ is the freestream velocity. All four ratios have been investigated for utility in scaling experiments between engine and laboratory conditions.

$$DR = \frac{\rho_c}{\rho_\infty} \tag{2.18}$$

$$VR = \frac{V_c}{V_\infty} \tag{2.19}$$

$$M = DR \times VR = \frac{V_c \rho_c}{V_\infty \rho_\infty} \tag{2.20}$$

$$I = M \times VR = \frac{V_c^2 \rho_c}{V_\infty^2 \rho_\infty} \tag{2.21}$$

For example, Sinha et al. [12] examined the effects of coolant density on η downstream of a cylindrical cooling hole. They used cold air as the coolant at various temperatures so that the density could be varied. They examined the abilities of velocity ratio (VR), mass flux ratio (M), and momentum flux ratio (I) to scale the effects of the density variation, but no single parameter was entirely effective. Similar studies have also been conducted using foreign gases. For instance, Haas et al. [13] used Freon mixed with the air coolant to elevate the density of the

coolant relative to the freestream gas. With none of those scaling parameters ($VR, M,$ or I) effectively accounting for the density differences, a reasonable conclusion that some have drawn from such work is that one must match the density ratio in experimental work.

However, none of those parameters has any particular significance in the energy equation, although they are of importance in the momentum equation. Density appears only once in the energy equation and it is multiplied by the specific heat, c_p (and velocity). Rutledge and Polanka [14] noted that including the ratio of specific heats accounts for the coolant energy transport capacity. Using a laid-back fan-shaped cooling hole (the 7-7-7 geometry by Schroeder and Thole [15]) with zero compound angle, Fischer et al. (Refs. [16] and [17]) showed that the energy equation dictates that the advective capacity ratio (ACR) must be matched.

$$ACR = \frac{c_{p,c}}{c_{p,\infty}} \times M = \frac{c_{p,c} V_c \rho_c}{c_{p,\infty} V_\infty \rho_\infty} \tag{2.22}$$

Fischer et al. [16] demonstrated the utility of ACR by showing that it scales adiabatic effectiveness for a range of densities and specific heats, including helium, shown in Figure 3. They also found that ACR's utility is limited to cases where the coolant jet is attached to the surface. Figure 4 shows the limit Fischer et al. found for ACR to scale η. This plot shows that for flow rates with momentum flux values higher than 0.6 for most gases, the effectiveness drops off due to the coolant flow lifting off the surface. This crucial research found that ACR scales η for $I \leq 0.6$. For ACR to scale η, it is also important for the cooling holes to have no compound angle, otherwise, the trajectory of the coolant is governed by the momentum flux ratio.

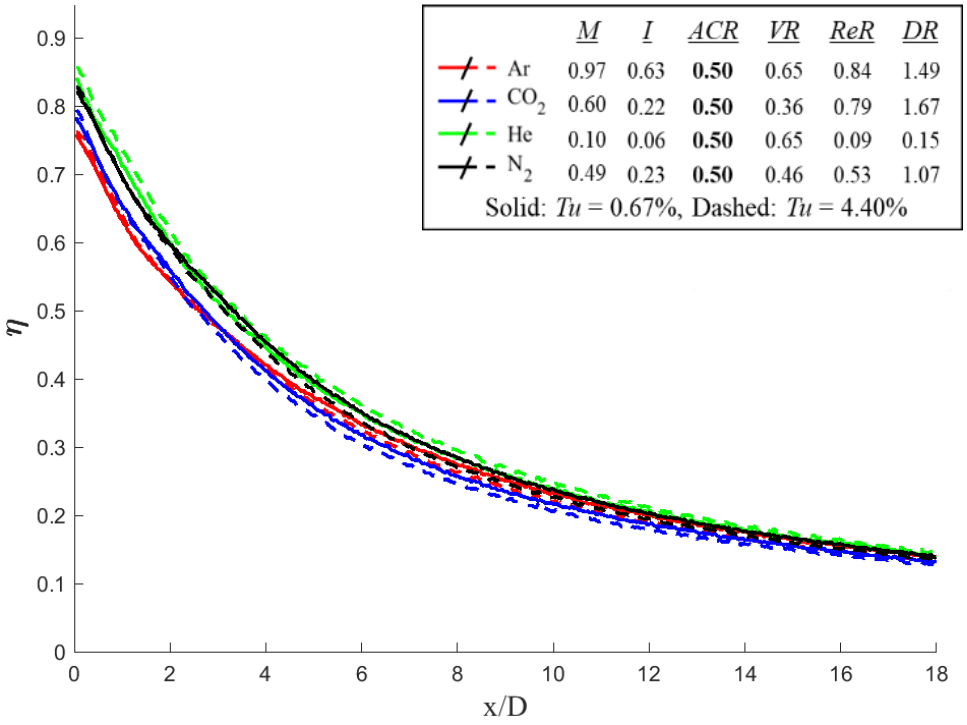

Figure 3. Adiabatic effectiveness distributions at y/D=0 at ACR=0.5 [17]

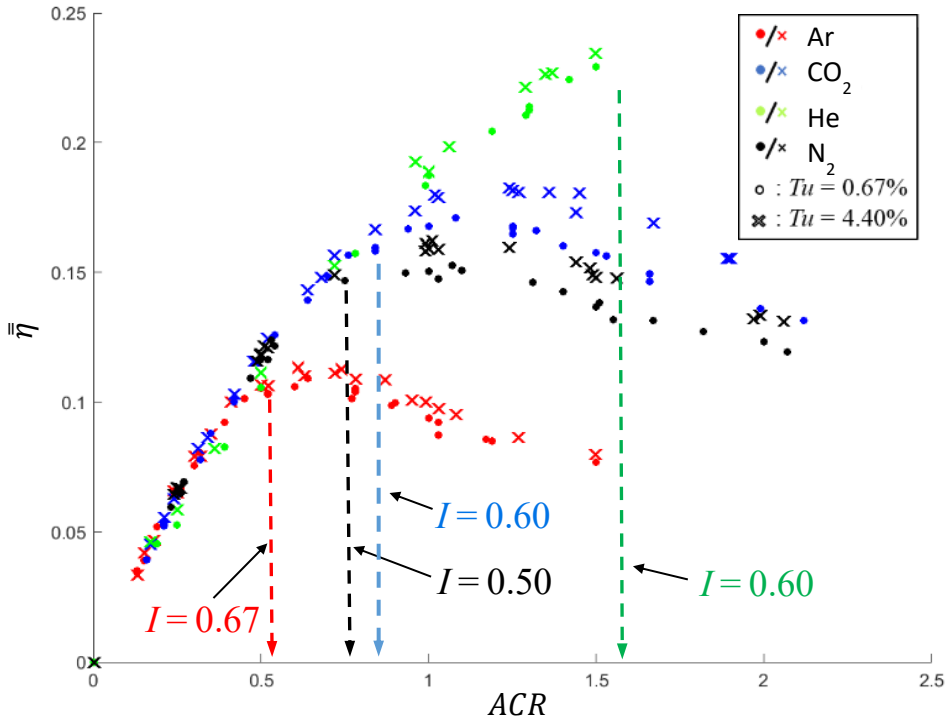

Figure 4: Adiabatic effectiveness distributions for a range of ACR, from [16]

Another parameter frequently used in the literature to measure the benefit of film cooling is the net heat flux reduction, defined in Refs. 6 and 18 as

$$NHFR = 1 - \frac{q_f^{"}}{q_0^{"}} = 1 - \frac{h}{h_0}\left(\frac{T_{aw} - T_s}{T_\infty - T_s}\right) = 1 - \frac{h}{h_0}\left(1 - \frac{\eta}{\phi}\right) \quad (2.23)$$

NHFR describes the reduction in heat load that could be achieved by adding film cooling while keeping the wall temperature constant. NHFR is problematic because film cooling does reduce the wall temperature. One part of the NHFR equation is the ratio of heat transfer coefficients, $\frac{h}{h_0}$. Physically, this is the ratio between the local heat transfer with and without the film cooling feature. Initiation of a new thermal boundary layer means this ratio is usually greater than unity [19] because film cooling increases the heat transfer coefficient on the surface. The increased ratio is partially offset by a reduction in T_{aw}. However, the effect of the ratio on overall effectiveness (where there is no adiabatic wall) is unknown. Another problem with NHFR is that there is no distinction between the internal coolant temperature, T_c, in the traditional definition for ϕ and the exit coolant temperature, $T_{c,e}$, in the definition for η. Overall, Ref. [16] showed η can be scaled using ACR at low I on a flat plate. However, Ref. [7] showed scaling η alone is insufficient to scale ϕ.

2.1.1.2. Biot Number

The second parameter important in scaling ϕ is the Biot number. The Biot number must be matched to scale overall effectiveness tests conducted at low temperature to results at engine conditions. Biot number matching is accomplished through the selection of a material with an appropriate thermal conductivity. Stewart and Dyson [20] show that matching Bi requires the ratio of the thermal conductivity of the model to that of the engine component must match the ratio of the thermal conductivity of the freestream gas at experimental conditions to that at

engine conditions. Nusselt number is generally matched in experiments since Reynolds number is typically matched and Prandtl number is generally a weak function of temperature for gases.

Matched Nusselt number implies:

$$\frac{h_{lab}}{h_{eng}} = \frac{L_{eng}}{L_{lab}} \frac{k_{\infty,lab}}{k_{\infty,eng}} \tag{2.24}$$

where h is the heat transfer coefficient, L is the length scale, k_∞ is the freestream fluid thermal conductivity, the subscript lab refers to conditions in a laboratory, and the subscript eng refers to conditions in an operating gas turbine engine. Similarly, matching the Biot number implies:

$$\frac{k_{w,lab}}{k_{w,eng}} = \frac{h_{lab}}{h_{eng}} \frac{L_{lab}}{L_{eng}} \tag{2.25}$$

Substituting Eq. (2.24) into Eq. (2.25) shows that the length scale of the laboratory model cancels and is thus irrelevant to matching the Biot number. The final requirement to match the Biot number is simply:

$$\frac{k_{\infty,lab}}{k_{\infty,eng}} = \frac{k_{s,lab}}{k_{s,eng}} \tag{2.26}$$

That is, for the Biot number to be matched between laboratory and engine conditions the ratio of the air's thermal conductivity to that of the solid must be matched. Polanka et al. [21] were the first to express this simple, yet important requirement. With the thermal conductivity of air increasing substantially with temperature, Eq. (2.26) demonstrates that the thermal conductivity of an experimental model must be substantially lower than that of the actual engine hardware. Stewart and Dyson demonstrated [20] the coincidental fact that the thermal conductivities of air and Inconel 718 happen to behave similarly with temperature. Inconel 718 is not only a practical high-temperature metal alloy itself but also similar in properties to other high-temperature turbine components. It so happens that such real metallic components may be

tested at low-temperature lab conditions without tremendous mismatch of the Biot number. Stewart and Dyson showed the expected Biot number error is less than 10% at any temperature experiment with an average $\phi = 0.6$.

Since the thermal conductivity of air can differ by approximately a factor of three between engine conditions and common experimental conditions, the thermal conductivity of the experimental model must have a substantially lower thermal conductivity than the actual engine component. Many matched-Biot experiments such as those of Terrell et al. [22] and Chavez et al. [23] showed the importance of matching the Biot number in scaling ϕ. In an anisotropic material, k_{wall} is a tensor of rank two, therefore the Biot number for an anisotropic material is also a tensor of rank two. There has been no research on how to scale the Biot number when it is a tensor.

2.1.1.3. Ratio of Heat Transfer Coefficients

The third parameter is the ratio of the heat transfer coefficients on the internal and external walls. While a good deal of prior work has focused on what must be done to match η and Bi, relatively little attention has been paid to the subtleties that arise to match h/h_i. The external and internal heat transfer coefficients can each be nondimensionalized using the Nusselt number, which includes a length scale and the thermal conductivity of the fluid. The Nusselt number is the dimensionless wall heat transfer coefficient. It is a function of the Reynolds number and Prandtl number [24]. For fully developed, laminar flow, the Nusselt number is a constant.

$$Nu = \frac{hL}{k_f} \tag{2.27}$$

This definition can be rearranged to find the convection coefficient

$$h = Nu\frac{k_f}{L} \tag{2.28}$$

Eq. (2.28) shows coolants with a higher k yield a higher internal convection coefficient if all other factors are equal. Coolants with higher thermal conductivity cause Pr_c to decrease, thereby increasing the heat transfer on the inside surfaces. This causes a lower h/h_i and therefore, according to Eq. (2.17), would also cause a higher ϕ value (because $0 \leq \chi\eta \leq 1$) if every other parameter is constant.

Albert and Bogard [7] found variations in *Nu* can alter the *h* ratio between the engine and experimental conditions, leading to additional errors in ϕ. Jones [25] characterized the effect that foreign gas used to simulate a coolant flow can have on the heat transfer coefficient along the coolant plume. Polanka et al. [21] performed experiments to measure ϕ and characterized how the external heat transfer coefficient was altered in the experimental situation while ensuring that the Biot number was approximately matched. However, no work has shown how to characterize how the selection of the coolant flowrate scaling parameter (e.g., M, I, ACR) can influence the ratio, h/h_i, and what might be done to prevent a mismatched value for it.

2.1.1.4. Coolant Warming

The final remaining parameter that must be matched to scale ϕ is χ. If all four of these parameters are matched, the model material, size, and temperatures are arbitrary. The coolant warming factor, χ, represents how much the coolant warms as it travels through a film cooling hole due to convecting heat away from the hole walls. Two studies (Refs. 26 and 27) have measured χ in low-temperature experiments with conducting models, but they did not try to determine any requirement to match χ to engine condition. Recently, Wiese et al. [28] showed a preliminary theory for the conditions necessary to scale χ. Additionally, they experimentally

demonstrated the theory for various coolant flow rate parameters. Though they made significant progress in identifying scaling parameters, their work also shows that matching χ is complex and multifaceted. Overall, there has been very limited research into matching χ for ϕ experiments.

2.1.2. Cooling Hole Geometry

According to Eq. (2.17), the four parameters discussed in the previous sections must be matched to scale ϕ. Another important experimental consideration is the cooling hole geometry. The model both Fischer et al. [16] and McNamara et al. [29] studied used a 7-7-7 shaped hole. This is a baseline cooling hole developed by Schroeder and Thole [15]. Because most shaped film hole designs are proprietary, they developed this shape to be an academic standard. As shown in Figure 5, the entrance to the 7-7-7 hole is a cylindrical hole, inclined at 30°. The diffused outlet has a 7° fan to both sides and a 7° layback diffused outlet. The diffuser shape is crucial because it helps the coolant flow stay attached to the downstream surface thereby further protecting the surface from the hot freestream. Without a diffuser, the coolant will more easily separate, and the resulting detached film is less effective in protecting the component.

	Range Common in Literature	7-7-7 Shaped Hole
Injection Angle, α	30 to 55°	30°
L_m/D	1 to 4	2.5
L_{lat}/D, L_{fwd}/D	1.6 to 9.5	3.5
L/D	2.8 to 11.5	6
Laidback Angle, β_{fwd}	2 to 25°	7°
Lateral Angle, β_{lat}	2 to 18°	7°
P/D	2.8 to 8	6
Coverage Ratio, t/P	0.3 to 0.8	0.35
Area Ratio, AR	2.5 to 4.7	2.5
Sharpness of Inlet and Breakout Edges	Usually Sharp	Sharp
Rounding of Four Edges Inside Diffuser, R/D	0 to 0.5	0.5

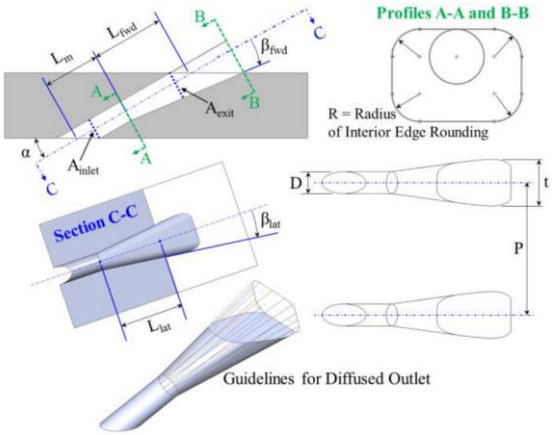

Figure 5. Geometric parameters for the baseline shaped hole [15]

Many studies have used this hole shape to represent a standard film cooling hole. Fischer [17] conducted baseline adiabatic effectiveness experiments using several different gases and a

7-7-7 shaped hole. His baseline η results with air coolant are shown in Figure 6. Note that at all three ACRs, the coolant flows preferentially to one side of the diffuser outlet. This phenomenon has been confirmed by experiments conducted by Schroeder and Thole [15] and Large Eddy Simulations (LES) using CFD by Simiriotis [30]. Both results show the coolant flow attaching to only one side of the coolant hole diffuser, one unique characteristic of this hole shape.

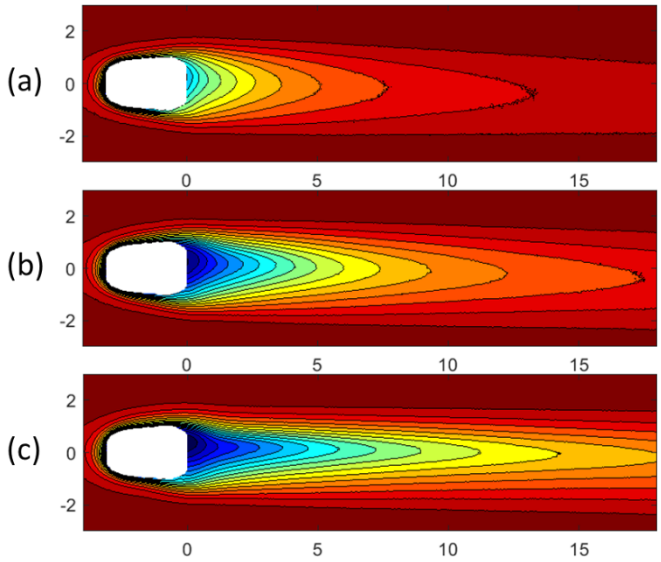

Figure 6. Contours of adiabatic effectiveness at (a) ACR=0.25, (b) ACR=0.5, and (c) ACR=1.0 [17]

Bryant and Rutledge [27] used CFD to study overall cooling effectiveness on a 7-7-7 hole array. A novel technique was used to separate the relative influence of plenum cooling, hole cooling, and film cooling on ϕ. The technique was demonstrated on a flat plate with five 7-7-7 staggered, shaped cooling holes arranged in an array. They found plenum cooling had the smallest effect on ϕ. Film cooling was the most effective form of cooling but had a decreasing effect as the coolant jets started to liftoff. Adiabatic effectiveness simulations confirmed jet liftoff contributed to decreasing cooling effectiveness at advective capacity ratios higher than ACR=1.0. The film was only effective downstream of the exit of each cooling hole. Additionally, the film built up with each hole exit causing increased cooling with increasing

downstream distance. Close to the hole exits, the material is thinnest and is, therefore, cooled most effectively by hole bore cooling which is dependent upon conduction. Hole cooling was most effective just upstream the hole exit and increased monotonically with increasing advective capacity ratio. This technique can be used to identify the most significant contributions to overall effectiveness to help designers focus on the cooling methods that are likely to provide the greatest incremental benefit when they are improved. These findings also show why it is so important to match the h/h_i ratio and χ. Areas where hole bore and plenum cooling are more effective than film cooling would be more sensitive to incorrect h_i matching. Additionally, l ow velocity plenums will yield low values of h_i.

Another hole shape commonly used in previous research is a cylindrical hole. Wiese et al. [28] and Bryant et al. [55] used this hole shape on a cylindrical leading edge. Unlike the 7-7-7 hole shape on a flat plate, this model has compound hole angles. The film cooling holes were oriented spanwise with $\gamma = 20°$ injection angle and $\beta = 21.5°$ angular spacing, as shown in Figure 7. Due to the lack of a diffuser, coolant ejected from this hole more easily detaches from the surface compared to the shaped hole previously discussed.

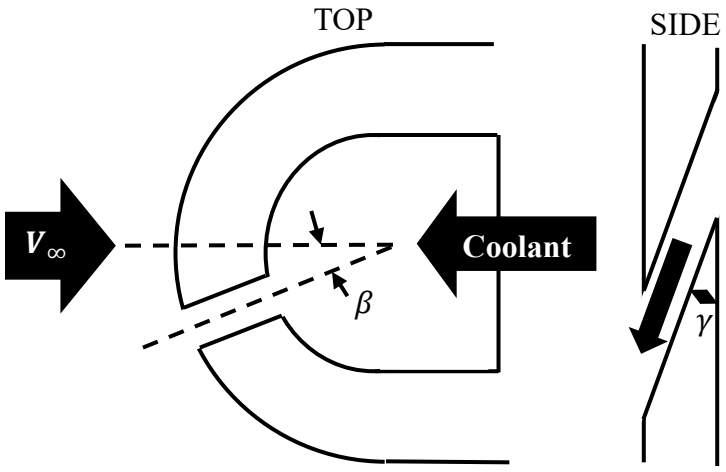

Figure 7: Cylindrical hole orientation on a cylindrical leading edge with compound injection. Adapted from Ref. [28]

Wiese et al. [28] examined whether various coolant flowrate parameters could scale ϕ on a leading edge of a film cooled turbine blade. They found c_p had a large influence on the ϕ distribution in the region of interest. ACR indicated the capacity of the coolant to absorb heat, especially important for any geometry with internal cooling. One cautionary finding was the injection angle of the cooling holes in the showerhead caused the momentum flux to dominate the external film. Overall, no coolant parameter could characterize ϕ due to the varied flow characteristics in the leading edge showerhead.

2.2. Ceramic Matrix Composites

Ceramic matrix composites (CMCs) are an important enabling technology for future gas turbine engines. One composite material frequently used in components in the hot section of gas turbine engines is a ceramic matrix composite with silicon carbide (SiC) matrix phase and fiber phase (SiC/SiC CMCs) [31]. The matrix and fiber components typically have different thermal conductivity, which therefore causes the composite to have anisotropic thermal conductivity. There is a wide variety of CMCs, however, it is assumed that any CMCs referred to in this section are SiC/SiCs. This section focuses on ceramic matrix composites as a representative CMC material. Though CMCs are the focus of this section, this research aims to be broad enough to apply to any material, including materials with isotropic or anisotropic thermal conductivity.

Compared to metallic super alloys, CMCs have several advantages when used in gas turbine engines. First, they have a much higher maximum use temperature. According to DiCarlo [32], metallic components' strength degrades significantly above 1100° C, whereas CMCs have demonstrated utility up to 1500° C [5]. They also have high fracture toughness and damage tolerance. Finally, CMCs have a third of the density of most super alloys and therefore are much

lighter [5]. The way CMCs are made dictates how these properties can be leveraged against the risks of using them. The specific risks and risk mitigation practices are discussed at the end of this section.

DiCarlo and van Roode [31] provide a thorough overview of CMCs for gas turbine engine hot-path components. There are a variety of CMC systems, the primary type used for hot-section components is SiC/SiC. They are made with silicon carbide fibers and are reinforced by a silicon-based matrix. A diagram of the fabrication process is shown in Figure 8, from another overview by DiCarlo [36]. To fabricate SiC/SiC CMCs a high-strength, low-diameter SiC fiber is made into a multi-fiber tow (like a thread). The tows are formed into a textile-like architectural preform as dictated by the component's shape and property requirements. Preforms can have fiber volume fractions up to 40% [32]. Next, a thin crack-deflecting interfacial coating is applied on the tow surfaces using Chemical Vapor Infiltration (CVI). These coatings are usually made from silicon-doped Boron Nitride (BN). Afterward, a silicon-based matrix is formed (infiltrated) by some process designed not to damage the fibers or coating. Every infiltration leaves pores (between 2-15% volume), called porosity. These voids usually hinder the material's performance in terms of thermal stability, conductivity, environmental durability, and creep-rupture resistance. Finally, some sort of environmental and/or thermal barrier coating is applied [31].

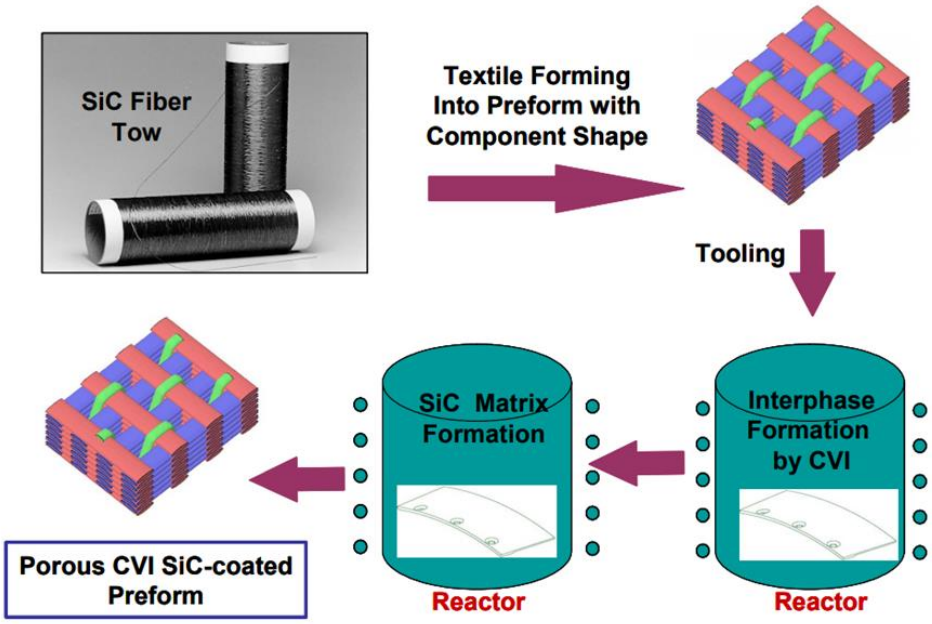

Figure 8: Diagram of CMC fabrication process for NASA CMC systems [36]

The goal of CMC designers is to create a material that avoids fractures under the maximum time, temperature, and stress conditions each part may be subjected to during use. CMC rupture characteristics are determined by loading on axis with the primary fiber direction so that the matrix carries little or no load due to a higher creep rate [32]. Put another way, the fibers should carry nearly all the load. Therefore, the fibers should be more creep resistant, or the matrix should have a higher creep rate than the fiber to reduce matrix cracking and environmental degradation to fibers. Parts must be thermally stable at expected temperatures and through temperature fluctuations, as any kind of cracking or delamination in the matrix can expose the fibers to environmental degradation. One way to address this challenge is to use 3D structures instead of 2D textile preforms. 3D architectures improve the mechanical and thermal shock resistance by increasing the thru-thickness thermal conductivity. They also offer an enhanced ability to do directional tailoring of in-plane and out-of-plane properties by using high-strength fibers with high thermal conductivity [33].

CMCs face several technical challenges. First, larger fiber tow sizes and preforms are stronger but more difficult to make into small parts. It is difficult to shape high-performing fiber tows to accommodate a sharp radius of curvature (like an airfoil leading edge and trailing edge) without fiber fracture [34]. Next, the matrix infiltration processes limit part thicknesses. Per Ref. [36], it is difficult to fully infiltrate thick parts without leaving large pores, or voids, in the center of parts. The voids can lead to delamination of the part. Third, environmental attack through matrix cracks, as seen in Figure 9, can lead to degradation from water vapor and free silica in the matrix interacting causing interlaminar cracking and recession [31]. Finally, CMCs can be prohibitively costly. Part assembly is not yet fully automated, so "man in the loop" yields to greater part to part variation. Automation is being pursued to reduce cost and part variability. Despite these challenges, the previously mentioned unique aspects of CMCs make them advantageous for many parts.

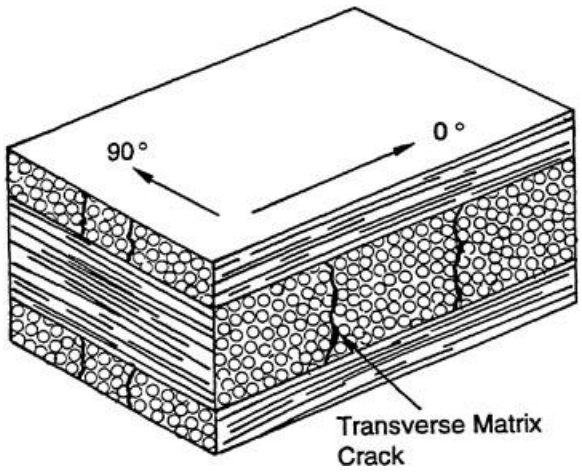

Figure 9: Transverse matrix cracks in a cross-plied composite [35]

Thermal conductivity is a particularly interesting aspect of CMCs. A high *k* is desired to reduce thermal shock during transients [36], however, the boron nitride interfacial coating has low thermal conductivity, thereby reducing the through-plane *k*. Delamination cracks induce additional thermal resistance within the material that can also significantly reduce the through-

thickness thermal conductivity. These two contrasting factors mean that CMCs have anisotropic thermal conductivity. The thermal conductivity differs between the through-thickness (k_y) and in-plane, (k_x and k_z) directions. The in-plane direction is aligned with the tows and layers of material in the CMC, as shown in a representative composite from Ref. [37] in Figure 10. The magnitude of the difference varies widely, depending on the material, matrix, and processing method, as shown in Table 1.

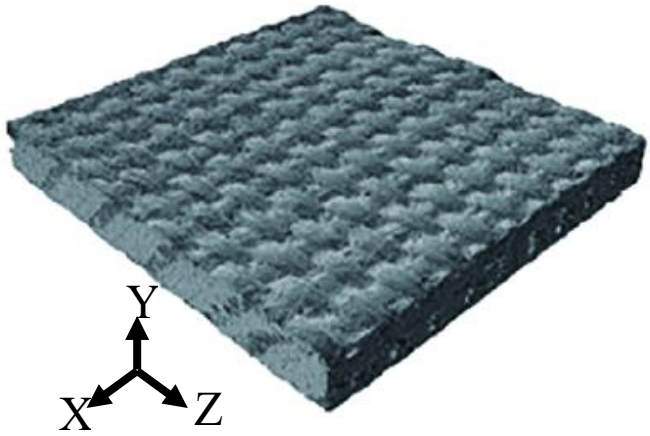

Figure 10: Coordinate system directions are shown on a SiC/SiC CMC. Adapted from [37]

Table 1: Comparison of in-plane (k_x) to through-thickness (k_y) thermal conductivity for several composites

Material	k_x/k_y
Carbon/epoxy [38]	10.4
Graphite epoxy weave fabric composite [39]	11.5
Hexcel F593 carbon epoxy prepreg laminate [40]	4.2
Graphite/epoxy matrix lamina [41]	9.8
SiC/SiC 2D fabric CVI-MI [31]	2.8
SiC/SiC 2D fabric Full PIP [31]	10.0

2.3. Anisotropic Thermal Conductivity

The final part of the literature review covers anisotropic thermal conductivity. This is both a unique part of the literature, as well as an intersectional area between gas turbine cooling and

CMCs. The first part of this section discusses literature about *k* as a tensor and the second part covers previous work on the intersection of these areas.

To provide a basis for further discussion, a basic overview of anisotropic thermal conductivity from Özışık [42] is summarized in the following section. Heat flux in isotropic solids obeys Fourier's law, Eq. (2.29), where thermal conductivity is independent of direction and the heat flux is normal to the surface.

$$\boldsymbol{q} = -k\nabla T \tag{2.29}$$

In anisotropic solids, the component of heat flux depends on the linear combination of the temperature gradients in each direction. The thermal conductivity of a 3D solid can be expressed as a coefficient of a second-order tensor $\bar{\bar{k}}$.

$$\bar{\bar{k}} = \begin{bmatrix} k_{11} & k_{12} & k_{13} \\ k_{21} & k_{22} & k_{23} \\ k_{31} & k_{32} & k_{33} \end{bmatrix} \tag{2.30}$$

For the rest of the document, it is assumed all anisotropic thermal conductivity tensors in 3D space are second order. Therefore, the general expressions for the three components of heat flux are

$$\begin{aligned} -q_1 &= k_{11}\frac{\partial T}{\partial x_1} + k_{12}\frac{\partial T}{\partial x_2} + k_{13}\frac{\partial T}{\partial x_3} \\ -q_2 &= k_{21}\frac{\partial T}{\partial x_1} + k_{22}\frac{\partial T}{\partial x_2} + k_{23}\frac{\partial T}{\partial x_3} \\ -q_3 &= k_{31}\frac{\partial T}{\partial x_1} + k_{32}\frac{\partial T}{\partial x_2} + k_{33}\frac{\partial T}{\partial x_3} \end{aligned} \tag{2.31}$$

Written in index notation, the heat flux is

$$q_i = -k_{ij}\frac{\partial T}{\partial x_j} \tag{2.32}$$

where the summation is implied by repeated indices. Therefore, for an anisotropic solid, the heat flux is not necessarily in the same direction as the thermal gradient.

There are three limitations to what each coefficient can be. Onsagar [43-44] shows that when the fluxes (q) and forces ($\partial T/\partial x$) are related to each other linearly, as in Equation (2.31), the coefficients obey the reciprocity relation. Casimir [45] further applied this logic to heat conduction in anisotropic solids. Therefore, the thermal conductivity coefficients obey reciprocity, that is:

$$k_{ij} = k_{ji} \tag{2.33}$$

Further, according to irreversible thermodynamics, the diagonal components are positive,

$$k_{ii} > 0 \tag{2.34}$$

where the summation is not implied by the repeated index. And the magnitude of the off-diagonal components k_{ij} where $i \neq j$, is limited by

$$k_{ii}k_{jj} - k_{ij}^2 > 0 \tag{2.35}$$

where the summation is again not implied by repeated indices. These three equations are the natural limits for thermal conductivity coefficients.

Formalev [46] authored a general review of heat transfer on bodies with 2D anisotropic *k*. In reviewing the governing equations, he comes to several important conclusions. First, at the boundaries on an anisotropic media, the normal component of heat flux is continuous, however, the tangential component may be discontinuous. Next, he solved the governing equations to determine the temperature distribution within a given anisotropic body. Using this method, he found that given a high degree of anisotropy, with the highest value of thermal conductivity along the principal axis, it is possible to considerably reduce the downstream heat flux. Finally,

he found a theoretical basis for ‘heat islands’. Under a very high degree of anisotropy ($k_{11} = 200 \times k_{22}$), the temperature field can separate, and boundary isotherms appear.

Subsequent researchers show how these theories compare to tests with physical materials. To scale CMC experiments from laboratory to engine scales, it is important to understand how the thermal conductivity of CMCs varies with temperature. Appleby et al. [47] examined the temperature dependence of electric resistance for various MI-CVI SiC/SiC composites. The testing used laser-based heating, which induced a longitudinal thermal gradient. Therefore, the authors analytically modeled the temperature-dependent transverse thermal conductivity. They found the fiber *k* decreases linearly with temperature from 31 W/m-K at 300 K to 15 W/m-K at 1500 K. Recall Stewart and Dyson [20] found Inconel experiments scale well because the thermal conductivity of both air and Inconel 718 increase ~2.5X over the specified temperature range. Because CMC's thermal conductivity decreases with temperature, results obtained by testing CMCs at laboratory scale experiments do not automatically scale to engine conditions. More research is needed to determine which parameters are important to match to scale laboratory CMC experiments.

There has been very little research on the effects of anisotropic conduction on ϕ. Tu et al. [48] performed a numerical study looking at the effect anisotropic thermal conductivity has on the heat distribution on a composite turbine vane with cooling holes. The authors found that by changing the anisotropic thermal conductivity, the location and magnitude of the max temperature varied. In one case, they found a nearly 100 K change in one spot by increasing the anisotropic thermal conductivity in one direction to be 20 times as much as the other directions. They concluded that it is important to take anisotropic thermal conductivity into account when conducting thermal analysis on a composite hot component [48].

The same group [49] looked at the effect of anisotropic thermal conductivity on a film cooled flat plate. In the study, they used CFD to vary the thermal conductivity in one direction and the angle of the tows to determine the effect on cooling effectiveness. Using this method, they were able to keep the magnitude of the *k* tensor constant with each change in hole angle. Most significantly, they found that by increasing the component of heat transfer by a factor of four in the direction of the holes, cooling just upstream of the hole outlet (hole cooling) was increased by $\bar{\phi} = .07$. The area around the hole showed the same level of change in ϕ from changing the angle of the principle thermal conductivity component. Further downstream, orienting the tows perpendicular to the flow increased $\bar{\phi}$ by 0.03. Changing the component in the span-wise direction did not have a significant effect.

Tu et al. [50] did a complementary experimental study. In the study, they examined the effect of anisotropic thermal conductivity on a flat plate with a row of cylindrical film cooling holes (identical to the previous study). The plate was tested in a heated tunnel, and overall effectiveness was measured using IR thermography. The plates were generated by cutting a block of carbon-fiber-reinforced resin matrix composite. Each plate had the tows at an angle in either the spanwise or through-thickness direction. The angles tested ranged from 0 to 90° in both directions. They also varied the blowing ratio on each plate. The study found that increasing the thermal conductivity by a factor of four in the through-thickness dimension leads to a 0.06 increase in $\bar{\phi}$ in the area around the coolant holes. They also found that increasing the conductivity in the spanwise direction leads to better cooling uniformity.

These three research efforts examine the same type of composite: a carbon fiber tow, resin matrix material with tows running in only one direction. This material has a different type of anisotropy and therefore, different behavior than a SiC/SiC CMC used in high-temperature gas

turbine parts. While these papers are used for trend comparison, a study focused on SiC/SiC CMCs may show different results.

In the future, the current manufacturing and material constraints for CMCs may be different. Xu et al. [51] calculated the effective thermal conductivity of a computer-generated composite with random material arrangements. Their motivation was to someday be able to manage heat load via constitutional design. In other words, design a material to have the ideal thermal conductivity for its intended use. However, there is no analytical solution to solve the effective thermal conductivity for components with anisotropic thermal conductivity. Therefore, the authors generated and validated a FEM model to determine the effective thermal conductivity. The results were affected by the size of the model and the mesh refinement. Research showing how CMCs conduct heat in different orientations inform forward-looking research efforts such as this.

2.4. Limitations of Previous Research

The previous research shows a need for more understanding of how anisotropic thermal conductivity affects overall cooling effectiveness. There have been numerous studies on film cooling, scaling overall effectiveness, CMC material properties, and even a few on cooling composites. However, further research is needed on the effect of CMC anisotropy on film cooling. Moreover, there is no published research on how to improve overall film cooling effectiveness in an anisotropic material or how to scale such results. Specifically, there is a lack of research on how to scale the Biot number for an anisotropic material, how to scale the ratio of heat transfer coefficients with any material, and how to combine that knowledge to design well-scaled film cooling experiments for an anisotropic engine component.

This page is intentionally left blank

3. Effects of Anisotropic Thermal Conductivity on a Film Cooled Flat Plate

This chapter addresses the first two objectives in the context of a film cooled flat plate. The first objective is to understand how ϕ changes when a material with anisotropic *k* is used, compared to a traditional metallic material. The second objective is to leverage this knowledge to increase ϕ. Overall effectiveness for a component in a gas turbine engine hot gas path is determined not only by the design of coolant flow but also by the conduction through the materiel itself. CMCs have anisotropic thermal conductivity, giving rise to heat flow that differs somewhat relative to what we have come to expect from experience with traditional metallic components. Conjugate heat transfer CFD simulations were performed to isolate the effect anisotropic thermal conductivity has on a cooling architecture consisting of both internal and external cooling. As CMCs begin to make their way into gas turbine engines, care must be taken to ensure that anisotropy is characterized properly and considered in the thermal analysis.

3.1. Model Description

CFD was used in this study to go beyond physical limitations by mathematically manipulating the thermal conductivity tensor. Physically, this would be very difficult because it would involve building many different CMC layups with tows in strange directions, with various thermal conductivities. The cost would be prohibitively expensive (a quote for three different SiC/SiC CMC layups was over $100,000). Therefore, to gain an understanding of the effect of various anisotropic *k* tensors, only CFD is utilized in this section.

3.1.1. Geometry

The geometry used in these simulations was a flat plate with shaped film cooling holes. The model was previously used in Bryant et al. [27]. The film cooling holes are the 7-7-7 shaped holes first characterized by Schroeder and Thole [15]. They are at a 30° angle to the freestream

with a 7° layback and 7° fan to each side. The holes are in a staggered array with a spanwise pitch of 6.32-hole diameters and a row spacing of 5.91-hole diameters, where the metering diameter of the hole is 0.643 cm. A diagram of the model is shown in Figure 11 and a schematic of the hole geometry is shown in Figure 12. Dimensions are shown in green. The top wall extends 50 hole diameters upstream of the first film cooling hole exit to ensure the flow is fully developed. The solid material is not shown in Figure 11 to highlight the hole shapes, but the material was completely meshed and solved to ensure the model is fully conjugate.

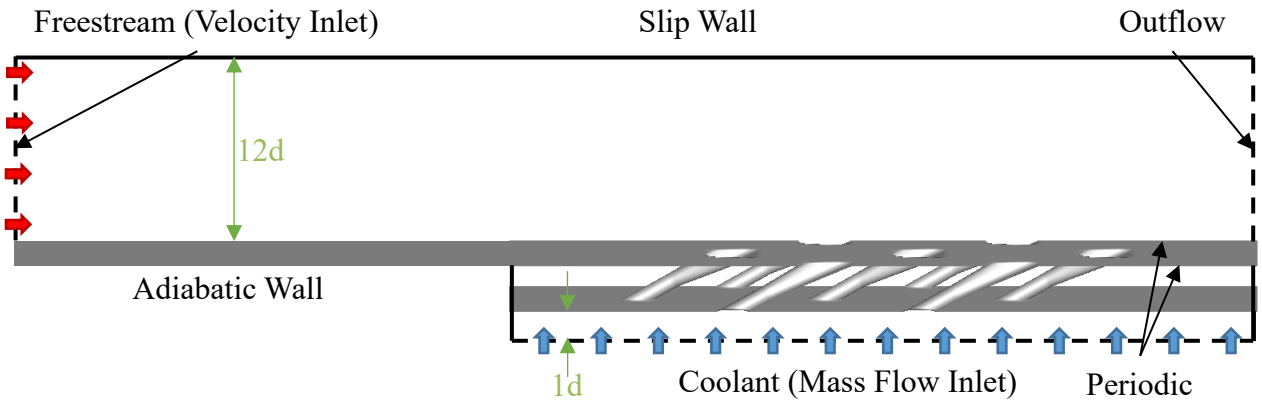

Figure 11: Flat plate model and boundary conditions

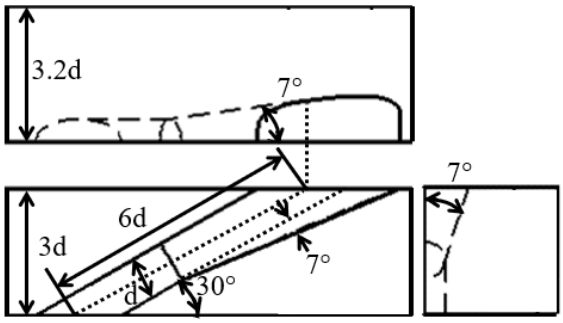

Figure 12: Schematic of the 7-7-7 hole based on the metering diameter (d=0.643 cm)

The mesh, shown in Figure 13, has 2.2 million structured cells with $z^+ \leq 1$ along the outside surface and in the coolant holes. Because the entire mesh is structured, it has a lower cell count

than many unstructured meshes. One drawback to this is that some cells in the far-field had high aspect ratios. A smoothing algorithm was used to reduce the maximum aspect ratio. Grid convergence was tested by creating higher resolution grids using Fluent's built-in grid adaptation ability. The adaption algorithm was solution-dependent, based on the velocity and temperature gradients. The areas refined were primarily around the film cooling hole exits and inlets in both the fluid and solid zones. The medium grid had 2.7 million cells and the fine grid had 3.2 million cells. Both grids yielded nearly identical to the original coarse grid, so the coarse grid was sufficient and used for all simulations.

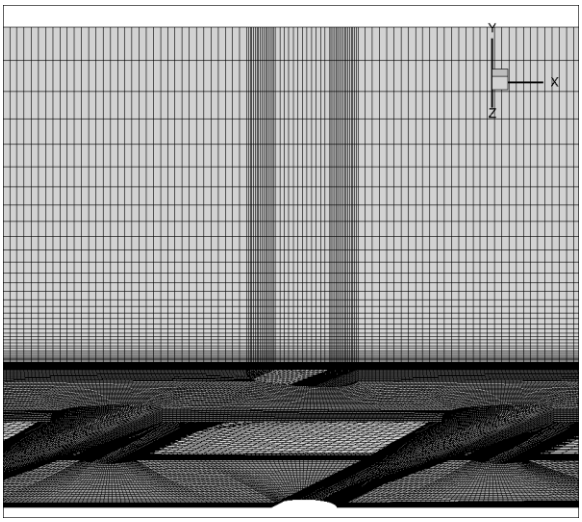

Figure 13: Mesh detail

3.1.2. Validation

The flow was solved using ANSYS Fluent's Reynolds-Averaged Navier-Stokes (RANS) realizable k-ε solver with enhanced wall treatment. The model has full conjugate heat transfer with both conduction and convection, where both the fluid and solid zones are solved simultaneously. Appendix A: Computational Fluid Dynamics Procedure has additional details about the Fluent settings used. The freestream air was set to 11.36 m/s at 300 K at the velocity inlet, to match the Reynolds number based on hole diameter in the experimental work of

McNamara et al. [29] $Re_d = 5{,}000$. Convergence was monitored by examining the surface temperature on the top wall. Once the temperature at several points on the surface, both in and out of the film cooling flow, was invariant for 100 iterations, convergence was achieved. After convergence was reached, the flow field was saved and used to initialize each run. Because only the *k* tensor was changed with each case, the flow field was nearly unchanged, and each case was able to converge in less than one hour.

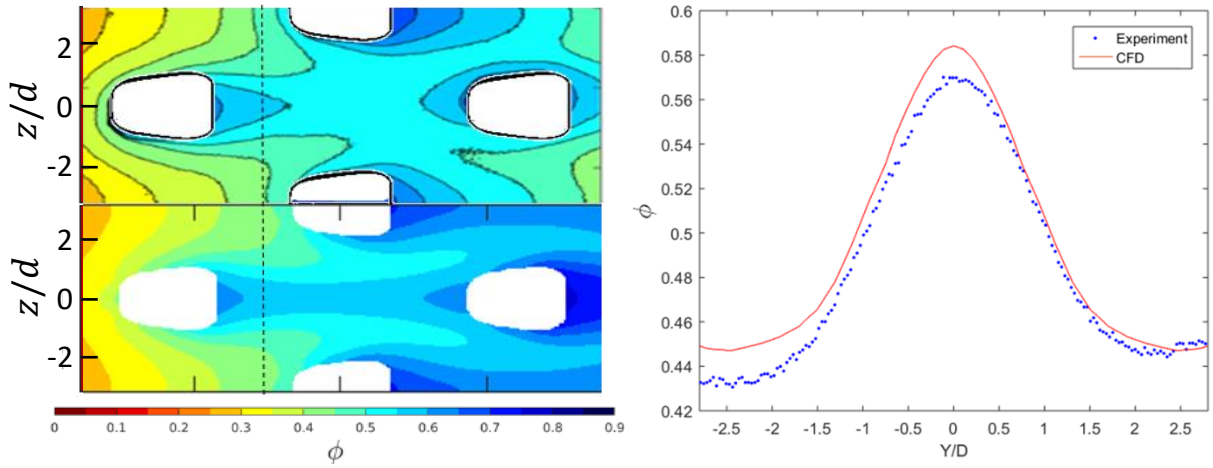

Figure 14: Left: comparison of experiment [29] (top) to computational results (bottom) at ACR=0.5. Right: spanwise ϕ plot at 1d upstream of the second row of cooling holes (see dashed line)

The mesh was validated by comparing it to experimental results. McNamara et al. [29] measured overall effectiveness on an array of 7-7-7 shaped holes in Corian. The experimental array only had three rows of holes due to limited coolant airflow; however, the computational model has five rows of coolant holes. To compare to the experiment, the isotropic conductivity in the mesh was set to a constant 1.007 W/m-K (the conductivity of Corian) and run to convergence. A comparison of the overall effectiveness at ACR=0.5 is shown in Figure 14. The figure on the right shows the spanwise ϕ at $x/d = 16.8$ for both data sets. There is agreement within $\phi \leq 0.02$ around the first and second rows of holes. Because the third row of holes is the final row in the experiment, the overall effectiveness is lower than the computational model.

Overall, the excellent agreement between the experiment and computational results indicates the mesh and computational solver used are sufficient. LES simulations would likely yield more accurate results, however, there is already good agreement between RANS and experiment. Further, LES simulations are very computationally expensive: each simulation will take about 10x as long as the RANS simulation. Because this study does not examine any variations in airflow, the RANS realizable *k-ε* solver was determined to be sufficient and was used for all the cases discussed herein.

3.1.3. Coordinate System

The thermal conductivity of the model was set using Fluent's materiel property settings. Because the goal of this research is to examine anisotropy, like that found in CMCs, the thermal conductivity was modeled as if layers of materiel were stacked together. Within the layers, the in-plane thermal conductivity is uniform in both directions. The through-thickness conductivity, or the component of thermal conductivity normal to the conductive layers, is much lower. To discuss the thermal conductivities in higher fidelity, coordinate systems must be described.

For the flat plate model, the global coordinate system is (*X, Y, Z*). Let a local coordinate system ($\zeta,\ \eta,\ \nu$) be oriented with the weave lay-up. When the coordinate systems are aligned, $X = \zeta, Y = \eta, Z = \nu$.

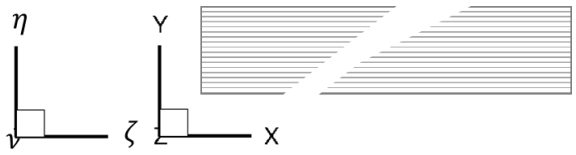

Figure 15: Global and local coordinate axis with a side view of representative layers in the model

The through-thickness and in-plane thermal conductivities are constant, therefore the thermal conductivity tensor in the local coordinate system remains constant. The through-thickness

thermal conductivity was chosen to match the experiment using Corian, k_η = 1 W/m-K and the in-plane k was chosen to be four times k_η, as in Ref. [40], $k_\zeta = k_\nu$ = 4 W/m-k. The thermal conductivity tensor in the local coordinate system remains constant, no matter what orientation the layers are in relative to the global coordinate system.

$$k_{\zeta\eta\nu} = \begin{bmatrix} 4 & 0 & 0 \\ 0 & 1 & 0 \\ 0 & 0 & 4 \end{bmatrix} \text{ W/m-K} \tag{3.1}$$

To set with thermal conductivity tensor in Fluent, $k_{\zeta\eta\nu}$ had to be rotated back to the global coordinate system. Tensor rotation is accomplished using the standard technique [52] where the tensor in the original unrotated or "unprimed" coordinate system can be specified in a rotated "primed" coordinate system:

$$k_{i'j'} = c_{mi'} c_{n'j} k_{mn} \tag{3.2}$$

In Eq. (3.2), $c_{ij'}$ is the direction cosine matrix. The thermal conductivity tensor in global coordinates, k_{XYZ} was then employed in Fluent's anisotropic material setting.

3.2. Results

Table 2 lists the first five cases tested. The *ACR* is 1.0 for every case tested. In each case, the thermal conductivity tensor is rotated about at least one axis. In cases with multiple rotations, the layers are rotated with respect to the global coordinate system, not the newly rotated local axes. In addition, the rotations are order specific: Z, X, then Y.

Table 2: Cases tested with each rotation angle listed in degrees

Case	Rotation in Degrees		
	Z	***X***	***Y***
1	0	0	0
2	30	0	0
3	90	0	0
4	0	90	0
5	0	90	28

3.2.1. Case 1: Baseline

The first plate modeled is the standard 0/90° lay-up commonly seen in flat plates. In this orientation, the layers are parallel to the outside surface, along the *X*, *Z* plane. The thermal conductivity tensor is therefore simple $k_{XYZ} = k_{\zeta\eta\nu}$ in Eq. (3.1). This case is the baseline for comparison with the remaining cases. The resulting contours of overall effectiveness are shown in Figure 16.

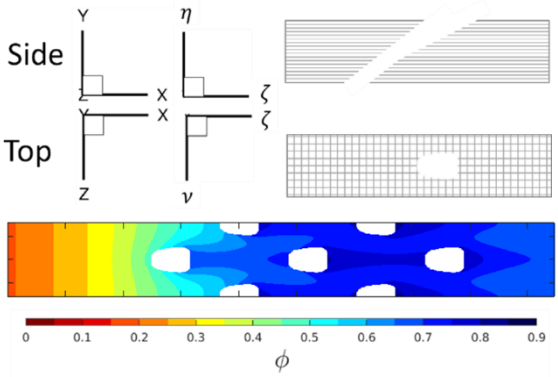

Figure 16: Case 1, 0/90 lay-up model orientation and overall effectiveness

It is impossible to directly compare overall effectiveness for otherwise equivalent isotropic and anisotropic cases because the change in thermal conductivity eradicates any semblance of equivalency. The anisotropic cases have a different thermal conductivity in at least one direction from any isotropic case. Increasing the conductivity in one direction, while reducing it in another, does not even out the 'bulk' thermal conductivity. This is because heat flux occurs due

to a directional temperature gradient, therefore the directionality of the thermal conductivity tensor cannot be 'averaged out'.

To better understand where heat transfer is occurring in each case, area-specific cooling was isolated using the technique shown in Ref. [27]. This is a computational technique using non-physical boundary conditions to remove heat transfer on individual surfaces or from film cooling itself. The result is the overall effectiveness without that specific form of cooling. In this case, three types of cooling are removed: plenum cooling, hole cooling, and film cooling. To remove plenum cooling, the internal surface of the flat plate facing the plenum is computationally set to adiabatic. To remove hole cooling, only the interior surfaces of the film cooling holes are made adiabatic. Finally, removing film cooling involves placing pressure outlets at the exits of the film cooling holes thereby removing the coolant so that it cannot flow over the external surface of the model, but the internal coolant flow remains unimpeded. Through this technique, one may determine the relative importance of each form of cooling to the overall effectiveness. The ϕ contours for each form of cooling removed and the baseline is shown in Figure 17.

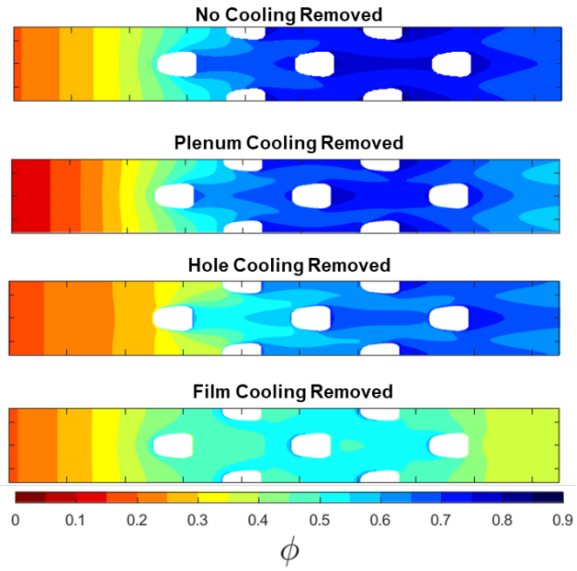

Figure 17: ϕ contours of cooling removed for Case 1

The top contour is identical to the baseline shown in Figure 16. The next contour shows the effect on ϕ from removing plenum cooling. Compared to the top figure, removing plenum cooling shows decreased effectiveness on the leading edge and trailing edge. The general shape of the contours is not affected since the contour shapes are driven by the hole cooling and film cooling. The third contour shows effectiveness with hole cooling removed. The main difference between this contour and the baseline is much lower effectiveness directly upstream of the first hole where the thin material with cool coolant flowing through the hole right under the surface would normally provide a substantial cooling effect. The final contour shows film cooling removed. This contour shows far lower effectiveness downstream of each cooling hole.

To better evaluate each case, delta phi ($\Delta\phi$) plots were also generated. The delta phi method first applied in Ref. [53], quantifies the nondimensional change in surface temperature due to some modification in the cooling scheme.

$$\Delta\phi = \phi_{modified} - \phi_{baseline} \tag{3.3}$$

or $$\Delta\phi = \frac{T_{s,baseline} - T_{s,modified}}{T_\infty - T_c} \tag{3.4}$$

By using $\Delta\phi$, one may discern the magnitude and location of changes in overall effectiveness due to changes in the cooling scheme. Of present interest is the effect of removing the various contributions to cooling and later, the technique is used to examine the effects of rotating the thermal conductivity tensor.

The $\Delta\phi$ contours for the baseline thermal conductivity tensor are shown in Figure 18. Each contour is the difference between each form of cooling removed and no cooling removed. The more negative $\Delta\phi$ is, the more important that form of cooling is in that location. The top contour shows plenum cooling is most effective on the leading and trailing edges. The middle contour

shows hole cooling is most effective in front of each film cooling exit, with decreasing effectiveness with downstream distance. The last contour shows film cooling is very effective downstream of each film cooling hole, with increasing effectiveness with downstream distance.

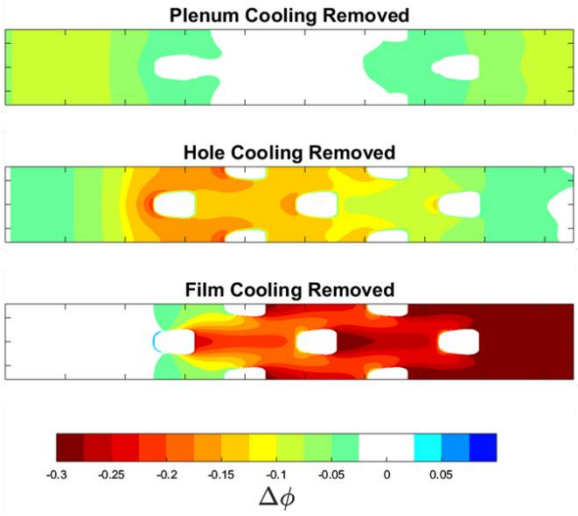

Figure 18: $\Delta\phi$ ($\phi_{cooling\ removed} - \phi$) contours for Case 1

3.2.2. Case 2: 30° around the *Z*-axis

In Case 2, the thermal conductivity tensor was rotated, as if the layers were rotated 30° around the *Z*-axis such that the layers are aligned with the metering section of the coolant holes. Figure 19 shows how the layers would be aligned within the film cooled plate. The thermal conductivity tensor does not change in the local coordinate system because it is aligned with the layers; however, in the global coordinate system, it now has non-zero off-diagonal components. According to Özışık in Ref. 42, such tensors are also common in monoclinic crystal systems, for which two sides of the crystal are at right angles and the third is inclined, much as has been done here by inclining the CMC planes. The thermal conductivity in the global coordinate system is given by:

$$k_{XYZ} = \begin{bmatrix} 3.25 & 1.299 & 0 \\ 1.299 & 1.75 & 0 \\ 0 & 0 & 4 \end{bmatrix} \text{W/m-K} \quad (3.5)$$

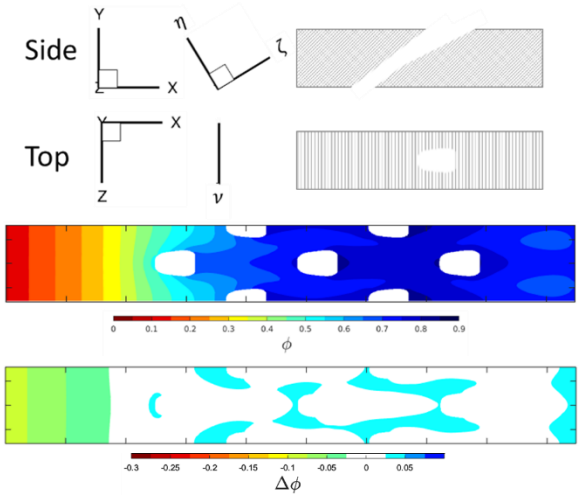

Figure 19: Case 2, 30° rotation around the Z-axis, model orientation, ϕ, and $\Delta\phi$ ($\phi_{rotated} - \phi_{baseline}$)

Figure 19 also shows the resulting ϕ contours for Case 2 as well as a $\Delta\phi$ plot comparing ϕ with Case 1. The alignment of the CMC layers with the hole somewhat impedes hole cooling in the region upstream of the cooling holes, thus the effectiveness is lower in the upstream region indicated by the negative $\Delta\phi$ upstream of the first hole. As the $\Delta\phi$ contours shown in Figure 21 demonstrate, removing the plenum cooling indeed generally causes a greater decrease in ϕ compared to Case 1 (see Figure 18). However, removing hole cooling resulted in a smaller decrease in ϕ indicating that hole cooling is a smaller contributor to the overall cooling when the CMC planes are aligned with the film cooling holes. Nevertheless, CMC planes do intersect both the holes and the surface laterally to the cooling holes, providing a small region of more substantial $\Delta\phi$ just adjacent to the cooling holes. Referring to the $\Delta\phi$ contour in Figure 19, the 30° rotation results in improved cooling in between cooling hole exits within the array. This improvement in ϕ is attributable to the fact that the CMC planes provide an improved

conductive path to the cool plenum, as shown in Figure 20 by the changes in the temperature around the holes due to the change in conductivity.

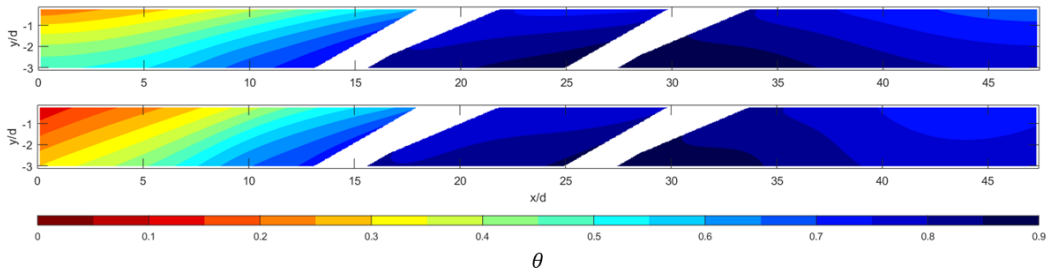

Figure 20: Side view of nondimensional temperature contours for the (top) standard 0/90 layup and (bottom) 30° rotation about the *Z*-axis

The improved conduction is also evidenced by the more negative $\Delta\phi$ with plenum cooling removed for the 30° rotation compared to Case 1. Since the 30° rotation allows for improved internal cooling relative to the baseline case, one would expect the coolant exiting the film cooling holes to be slightly warmer with the 30° rotation. Indeed, a comparison of the $\Delta\phi$ contours shows that $\Delta\phi$ with film cooling removed is less negative for the 30° rotation than it is for Case 1. To be clear, this means that a loss of film cooling with the 30° rotation is not as deleterious as it would be in the baseline case, i.e., the film cooling is a less important contributor to the overall effectiveness due to the improved internal cooling and resulting in warmer film coolant ejection.

3.2.3. Case 3: 90° around the *Z*-axis

Case 3 completes the rotation around the *Z*-axis to the full 90°. The layers are now stacked vertically so the layers are aligned span-wise when viewed from the top. In the global coordinate system, the layers are oriented in the *Y, Z* plane so the thermal conductivity in the *Y* direction is now four times that in the *X* and *Z* directions. The layup orientation, ϕ, and $\Delta\phi$ contours are shown in Figure 22.

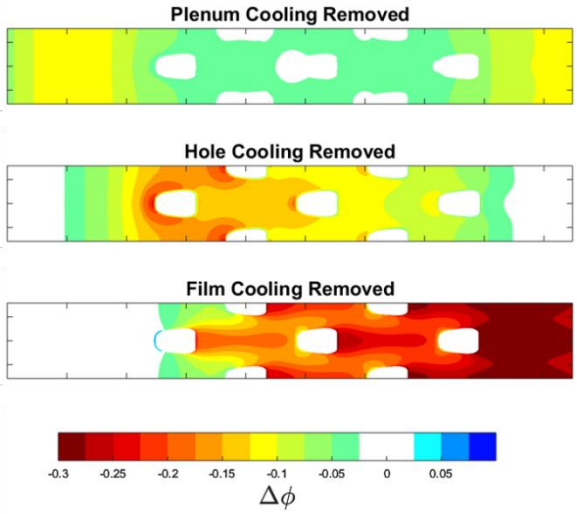

Figure 21: Case 2, 30° rotation around the Z-axis, $\Delta\phi$ ($\phi_{cooling\ removed} - \phi$) contours

$$k_{XYZ} = \begin{bmatrix} 1 & 0 & 0 \\ 0 & 4 & 0 \\ 0 & 0 & 4 \end{bmatrix} \text{W/m-K} \tag{3.6}$$

Case 3 is quite remarkable when compared to Case 1 because it is entirely cooler than the baseline case. As shown in Figure 22, the upstream leading edge is nearly identical, until the area in front of the first cooling hole. This area is now much cooler because the layers allow for increased hole cooling by creating improved conduction paths straight down from the hot surface to the cooler air traveling through the film cooling holes. This is repeated down the length of the plate, through the array of film cooling holes. The resulting average $\bar{\phi} = 0.626$, compared to the baseline average $\bar{\phi} = 0.581$. In essence, the overall effectiveness has increased nearly 0.05 on average, without any changes to the flow rate, type of holes, etc. The only change is the way the layers of conductive material are stacked.

The $\Delta\phi$ contours for the 90° Z-axis rotation are shown in Figure 23. Plenum cooling is much more effective in this case, particularly between holes and upstream of the first hole. Hole cooling is also much more effective in this case, compared to Case 1. Upstream of the first and second rows of holes $\Delta\phi$ is 0.1 lower (more negative) and in fact, the average $\Delta\phi$ is 0.05 more

negative than the baseline average with hole cooling removed. Hole cooling averages out to be nearly as effective as film cooling. Compared to the baseline, film cooling is slightly less effective, again due to the higher film coolant temperature resulting from the more substantial conductive cooling.

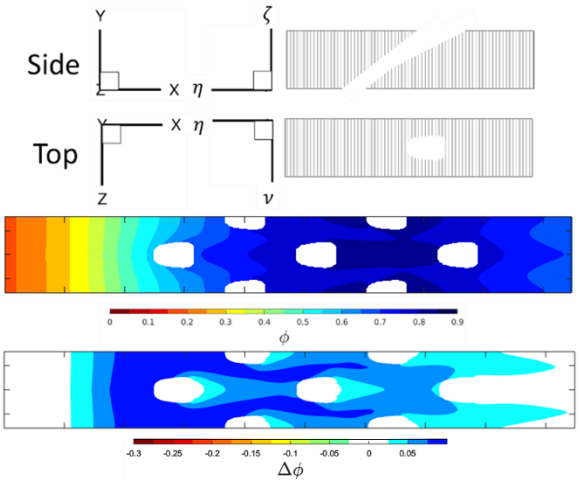

Figure 22: Case 3, 90° rotation around the Z-axis, model orientation, ϕ, and $\Delta\phi$ ($\phi_{rotated} - \phi_{baseline}$)

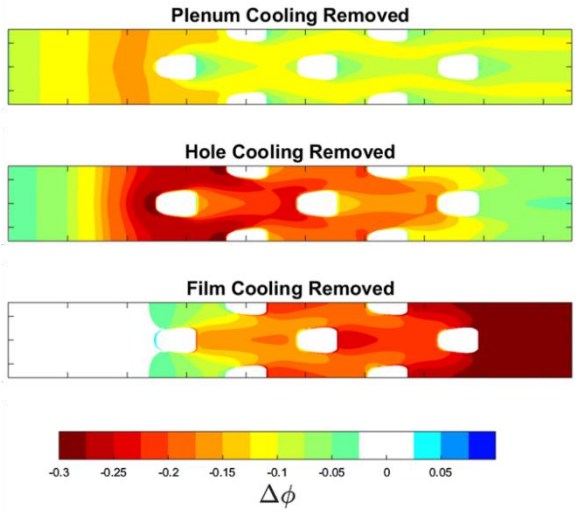

Figure 23: Case 3, 90° rotation around the Z-axis, $\Delta\phi$ ($\phi_{cooling\ removed} - \phi$) contours

3.2.4. Case 4: 90° around the *X*-axis

In Case 4, the layers were rotated 90° around the *X*-axis instead of the *Z*-axis. Therefore, the layers were now aligned horizontally, stretching down the length of the plate when viewed from

the top. In the global coordinate system, the layers are aligned with the *YX* plane. The *k* tensor has zero off-diagonal coefficients again because it was rotated the full 90°, shown in Eq. (3.7) and Figure 24. Case 4 is also cooler than Case 1 but differs in most other ways.

$$k_{XYZ} = \begin{bmatrix} 4 & 0 & 0 \\ 0 & 4 & 0 \\ 0 & 0 & 1 \end{bmatrix} \text{W/m-K} \tag{3.7}$$

First, there is elevated ϕ upstream and downstream of each coolant hole, extending much farther downstream than in Case 3. Because the layers are aligned with the stream-wise direction (and the direction of the holes in the material), heat flows directly to the plenum and coolant holes within the material. The result is increased effectiveness on the leading edge, trailing edge, and between holes in the array.

Figure 25 shows the $\Delta\phi$ contours for Case 4. Plenum cooling is significantly increased on the leading edge. There is also more cooling from the plenum between holes in the array, though less than Case 3 with 90° rotation about the *Z*-axis. Hole cooling is also much more significant in this case than the baseline. However, unlike Case 3, the increased effect of hole cooling is localized directly upstream of the hole exits. Because the layers are oriented such that the greatest conductivity is in the *X*-*Y* plane most conductive in the stream-wise direction, it follows that the increased effectiveness does not spread laterally in the Y direction as it did in all previous cases with tows oriented in the span-wise direction. The film cooling effectiveness is slightly decreased again.

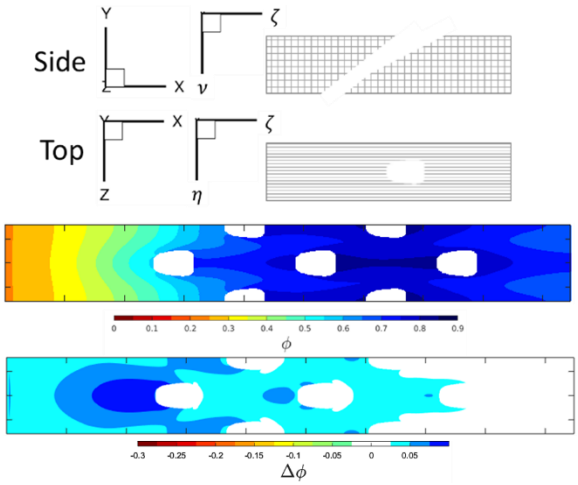

Figure 24: Case 4, 90° rotation around X-axis, model orientation, ϕ, and $\Delta\phi$ ($\phi_{rotated} - \phi_{baseline}$)

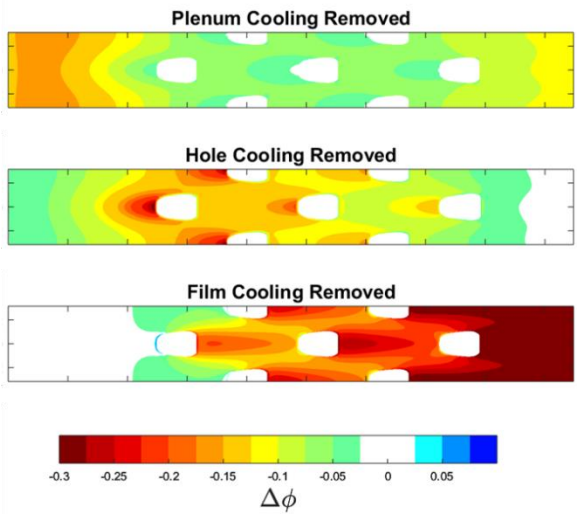

Figure 25: Case 4, 90° rotation around X-axis, $\Delta\phi$ ($\phi_{cooling\ removed} - \phi$) contours

3.2.5. Case 5: 90° around the *X*-axis and 28° around the *Y*-axis

The final example, Case 5, consists of two rotations. The first rotation, in this case, was 90° about the *X*-axis (same as Case 4), but then the layers were rotated 28° around the *Y*-axis so the layers aligned with the angle of the offset film hole array. The resulting *k* tensor, Eq. (3.8) has a different structure than the previous rotations. k_{XZ} and k_{ZX} are the only non-zero off-diagonal coefficients. The resulting ϕ distribution is shown in Figure 26.

$$k_{XYZ} = \begin{bmatrix} 3.3183 & 0 & -1.2571 \\ 0 & 4 & 0 \\ -1.2571 & 0 & 1.6817 \end{bmatrix} \text{W/m-K} \quad (3.8)$$

Overall, Case 5 is cooler than Case 1 and similar to Case 4. The far upstream leading edge has similar contour levels to Case 4 with the 90° rotation about the *X*-axis. This makes sense because this case has the same 90° rotation around the *X*-axis. Unlike Case 4, the additional rotation about the *Y*-axis means this case has more lateral conduction across the plate, so the increase in effectiveness is not limited to the span-wise direction from the holes. The most notable feature of Case 5 is the ϕ distribution is no longer symmetric. The airflow, and therefore temperature gradient, is still nearly identical to the previous cases, but the *k* tensor has shifted the heat flow to the side.

The $\Delta\phi$ contours for this case are shown in Figure 27. The magnitudes of these contours are similar and show the same trends as Figure 25; however, the asymmetry is obvious in Figure 27. Perhaps most notably, is the effect that hole cooling has in that it not only provides a great deal of cooling upstream of the holes, but the upstream hole cooling effect also has a significant component in the +z direction. Asymmetry is also pronounced in the upstream region for the plenum cooling removed $\Delta\phi$ contour. These contours reveal that in regions without a clear diagonal conductive path to cooling holes, the cooling is more dependent upon plenum cooling. Since the *k* tensor is the cause of the asymmetry, it makes sense that types of cooling most affected by conduction would most contribute to the asymmetry. The film cooling removed contour also shows some asymmetry from heat conducting within the surface, but the asymmetry due to removing film cooling is less pronounced than for the hole cooling and plenum cooling.

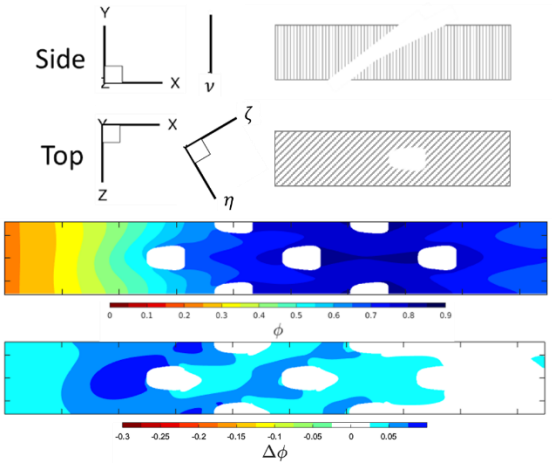

Figure 26: Case 5, 90° rotation around *X*-axis and 28° rotation around the *Y*-axis, orientation, ϕ, and $\Delta\phi$ ($\phi_{rotated} - \phi_{baseline}$)

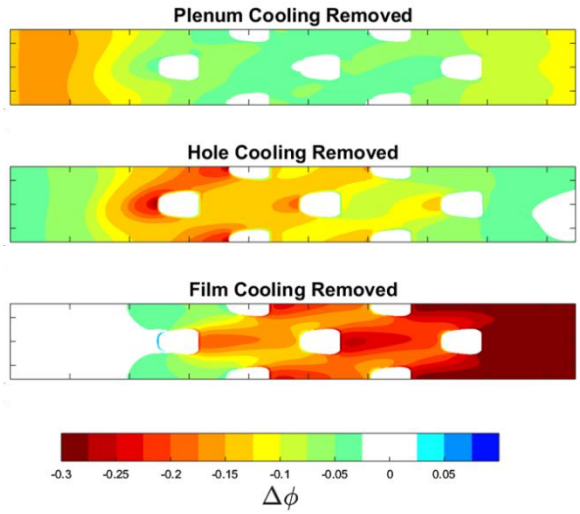

Figure 27: Case 5, 90° rotation around *X*-axis and 28° rotation around the *Y*-axis, $\Delta\phi$ ($\phi_{cooling\ removed} - \phi$) contours

3.2.6. Case Summaries

The area-averaged $\Delta\phi$ value for each form of cooling, in each case, is depicted in Figure 28. In each case, plenum cooling was more effective than in Case 1. As the rotation around the *Z*-axis increased from 0° to 90°, plenum cooling increased. Average hole cooling effectiveness slightly decreased when the angle of the layers matched the angle of the holes, thereby impeding the conduction path from the holes and top surface. However, when the CMC planes were

rotated to 90° about the Z-axis, hole cooling effectiveness increased by up to $\Delta\phi = 0.2$, nearly as high as the film cooling effectiveness. The two cases with rotation about the *X*-axis, Cases 4 and 5, have nearly identical $\Delta\phi$ values for each form of cooling because rotating the *k* tensor around the *Y*-axis did not change the conduction paths except to make them at an angle. In all cases, the film cooling effectiveness decreased due to increased heat transfer on the plenum and hole walls.

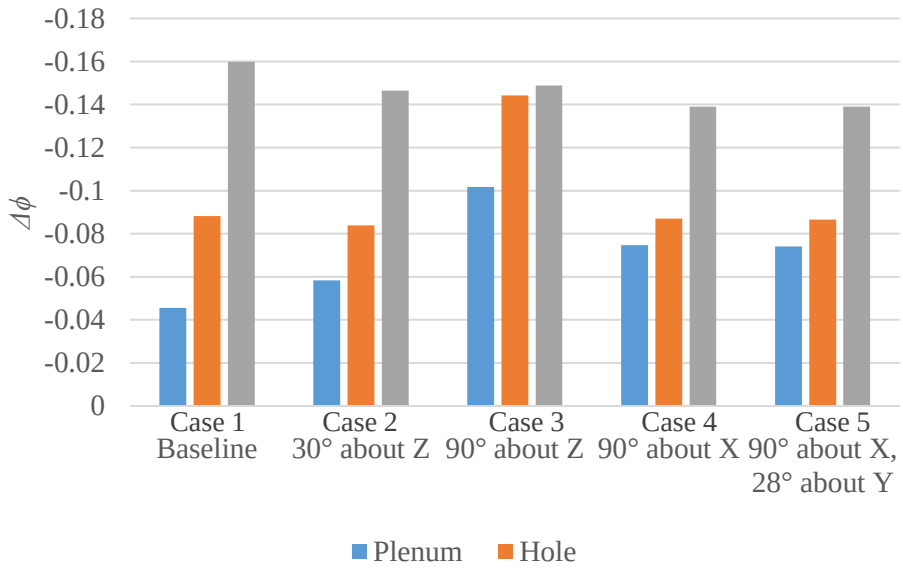

Figure 28: Average $\Delta\phi$ $\left(\phi_{cooling\ removed} - \phi\right)$ for each case

Contours of heat flux are shown in Figure 29 for all five cases. The contours are colored with the magnitude of the 3D heat flux and overlayed with 2D vectors of the heat flux. The hole walls, plenum wall, and top wall are all removed from the contours because they have high heat transfer due to convection. The magnitude of heat transfer on the walls dwarfs the heat transfer due to conduction inside the material, so it is blanked out in Figure 29. The second and third contours have increased heat flux connecting the plenum and top walls, showing more conduction due to the material rotation. Additionally, the conduction paths are at the same angle as the layers in the material. Finally, and most interestingly, unlike isotropic materials, the heat flux arrows are not perpendicular to the lines of heat flux magnitude. Fourier's Law in Eq. (2.3)

shows that an anisotropic k results in a tensor q" with multiple components too. This means the heat flux cannot be thought about the same way as an isotropic material and additional modeling will be useful to show heat flux, as shown in Figure 29.

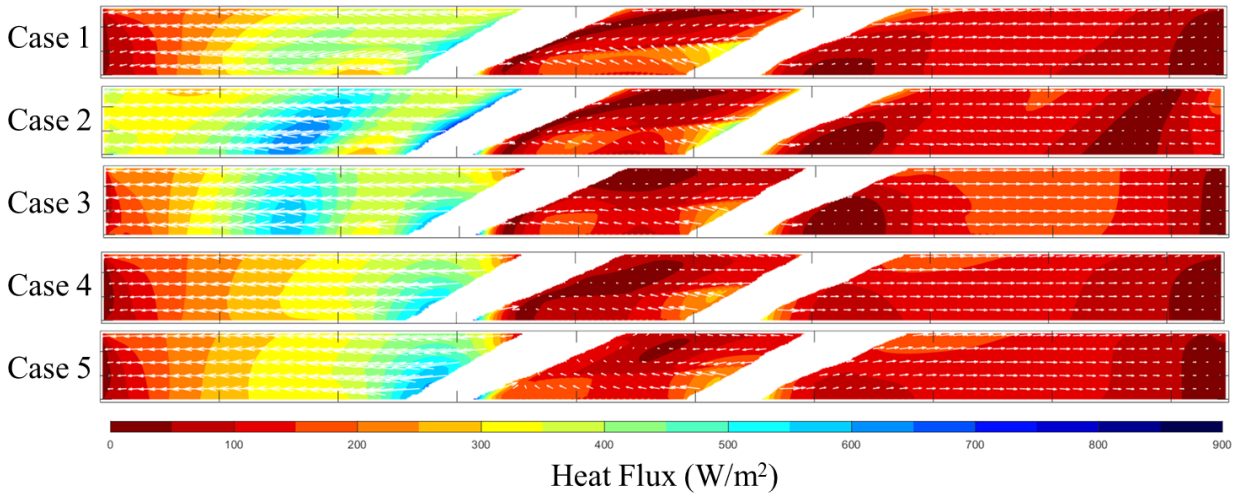

Figure 29: Side view of the flat plate with contours and vectors of heat flux

Though it is not possible to directly equate ϕ contours between iso- and anisotropic materials, it is reasonable to compare the maximum and minimum values that comprise the anisotropic tensor. Figure 30 shows three contours, the top is isotropic $k = 1$ W/m-K, the middle is Case 1 the baseline lay-up, and the bottom is the difference between the two. The difference between the two is less than 0.05 on the entire surface. Figure 31 shows a similar trend between isotropic $k = 4$ W/m-K and Case 3, the 90° rotation about the Z-axis. There is a slightly larger difference on the upstream edge, however across the majority of the surface, the difference is less than $\phi = 0.025$. Compare this to the difference between Case 1 and Case 3, shown in Figure 22. The $\Delta\phi = 0.1$ around the first three rows of film cooling holes, much higher than the differences between either of the anisotropic and isotropic differences. The effect of rotating the layers 90° is similar to increasing the isotropic thermal conductivity by four-fold, particularly in the regions around the film cooling holes. One reason for the improvement between Case 1 and

Case 3 is the increase in thermal conductivity in the thru-thickness direction. While that is certainly one factor, another factor to consider is changing the axis with reduced conduction, or where the 1 is in the *k* tensor. The isotropic case in Figure 31 shows just increasing the thermal conductivity is not as effective in the middle of the array as the rotated anisotropic tensor. The layers, in that case, span the width of the plate, so $k_{XX} = 1$ acts as insulator, thereby keeping the entire plate cooler.

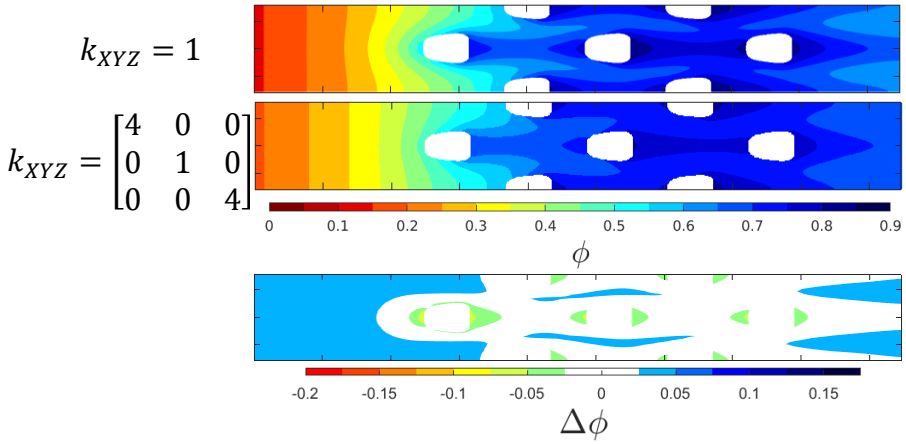

Figure 30: Overall effectiveness contours with isotropic $k = 1$ W/m-K, anisotropic Case 1, and $\Delta\phi$ $(\phi_{anisotropic} - \phi_{isotropic})$

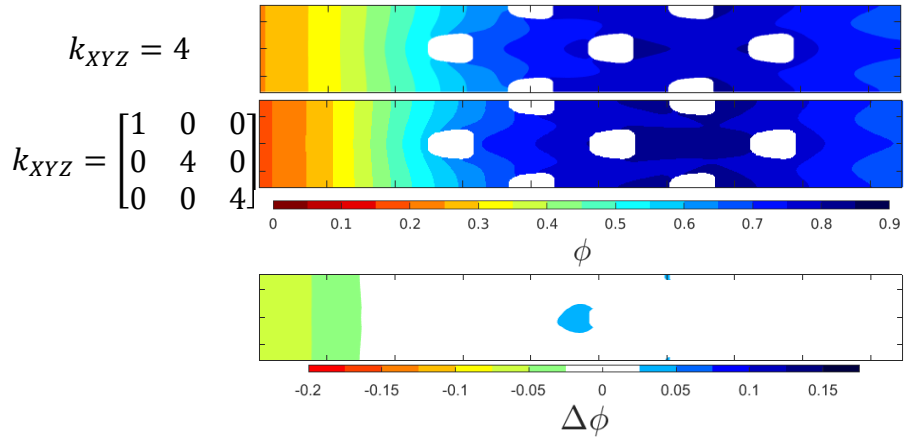

Figure 31: Overall effectiveness contours with isotropic $k = 4$ W/m-K, anisotropic Case 3, and $\Delta\phi$ $(\phi_{anisotropic} - \phi_{isotropic})$

3.3. Optimization

The next section addresses Objective 2, methods to improve ϕ by changing only the k tensor. The previous objective informs this objective because it is necessary to understand the effect of anisotropic k tensor to leverage it. In a CMC, the goal of this objective would be to understand how to orient the layers to optimize the overall cooling effectiveness. For example, this information could be used with 3D printed ceramics [54], to inform how to best orient chopped fibers in specific areas for maximum ϕ. The aim of this objective is not to be the final design because there are many other factors an engineer should consider, such as tensile strength, creep rates, rupture characteristics, etc. This objective aims to show only how to improve ϕ by changing k. CFD is used again because to do this physically would be prohibitively expensive due to the numerous models which would have to be constructed with various orientations. However, with CFD, numerous models can simply be mathematically constructed and tested quickly.

3.3.1. One Axis Rotation

The model used is the same computational model and solved flow field from the previous section. First, a rotation sweep of each axis was conducted. The solved airflow was used to initialize each case, then the tensor was rotated in increments of 10° around the *X* and *Z* axes, separately. The computational regimen required 35 unique CFD simulations, so it was imperative to consider computational efficiency. Since the velocity field was only minimally impacted by changing the solid's thermal conductivity tensor, a frozen velocity solution was used to solve the energy equation for each case. The converged energy solution and the frozen velocity field were then used to initialize the fully coupled simulation which was then run to convergence. The resulting ϕ distributions were area-averaged and plotted in Figure 32. The rotations around the

Z-axis are shown in orange and the *X*-axis is shown in blue. The figures to the left show some of the resulting overall effectiveness contours. The top and bottom (orange lines) contours are the best and worst average overall effectiveness when rotated about the *Z*-axis. The middle contour (blue line) is the for 30° rotation about the *X* axis.

The maximum effectiveness for rotations about the *X*-axis occurred at ±90°. At these equivalent angles, the layers were aligned as in Figure 24. For rotations around the *Z*-axis, the maximum effectiveness occurred at -70°. At this angle, the layers would be nearly perpendicular to the upstream side of the film holes. This angle allows the heat from the surface to flow at a sharp angle to the film holes, so more effective conduction occurs from the surface to the film holes, compared to other angles. Thus, hole cooling becomes even more effective. Plenum cooling is also improved by the high rotation angle about the *Z*-axis. The question left by this study was, what would happen if the two most effective angles were combined? Would these rotations, combined, produce the most effective cooling lay-up for this film cooling geometry?

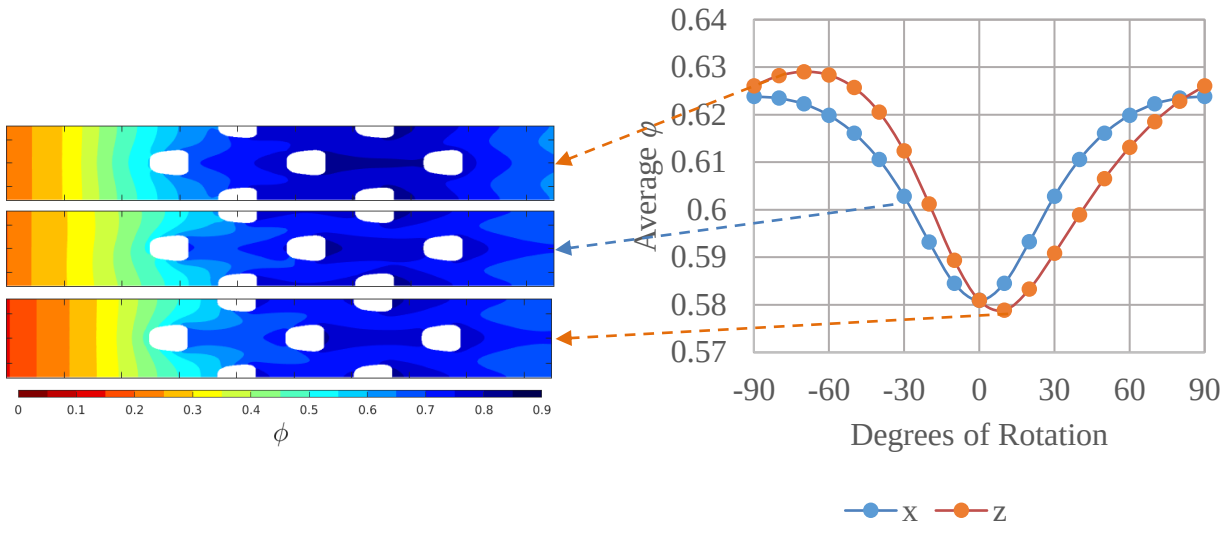

Figure 32: Average overall effectiveness with one axis of rotation

3.3.2. Two-Axis Rotations

While Figure 32 shows the optimum *X* and *Z* rotation angles for independent rotations, it does not address compound rotations about both axes simultaneously. A sweep of 2-axis rotations was also accomplished in 10° increments. This regimen required 307 total simulations (eliminating duplicate equivalent angles). Note that rotation about the third axis is unnecessary as it would only create redundant layup angles. The resulting ϕ distributions were again area-averaged and plotted in Figure 33 and Figure 34. A significant finding is that the standard 0/90 layup (no rotation) has nearly the worst overall effectiveness. Nearly any rotation improves the baseline effectiveness. The highest effectiveness occurs with any large negative rotation around the Z-axis, regardless of rotation around the X-axis. Recall that the case in Figure 22 also had very high effectiveness and was rotated 90° around the Z-axis.

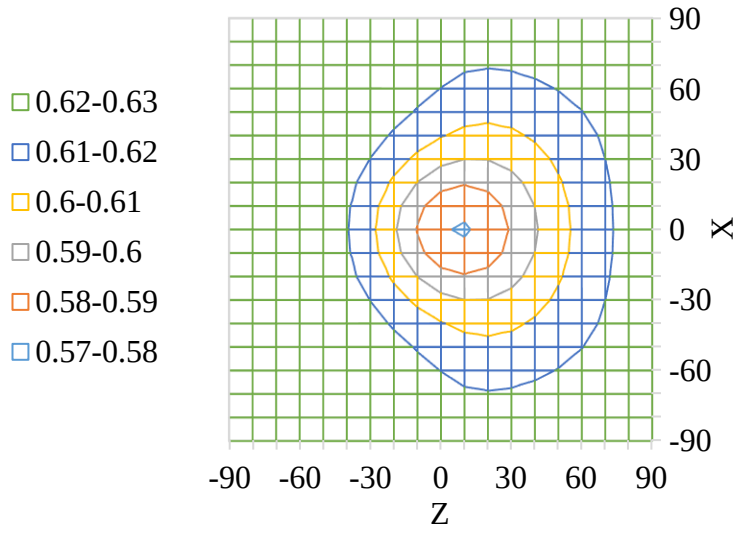

Figure 33: Contours of average overall effectiveness with two axes of rotation

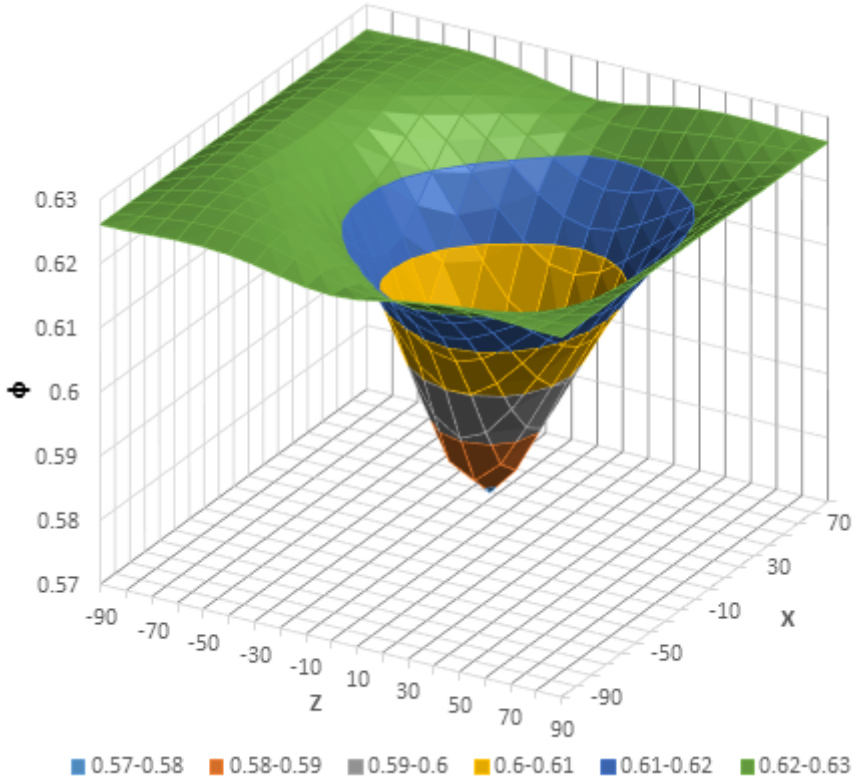

Figure 34: 3D map of average overall effectiveness with two axes of rotation

The lowest and highest average ϕ values in this data set show several interesting points. The lowest area-averaged ϕ occurs at 10° around Z and 0° around X. The highest area-averaged ϕ is at -70° around Z and 0° around X. The $\Delta\phi$ plot for the best case is shown in Figure 35.

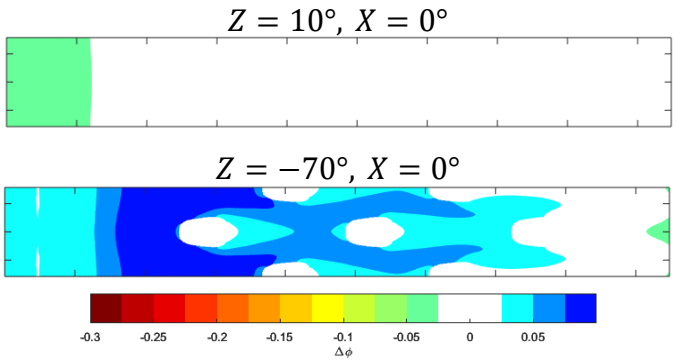

Figure 35: $\Delta\phi$ ($\phi_{rotated} - \phi_{baseline}$) contours for the worst case (top) and best case (bottom)

The worst case is only slightly worse than baseline. The ϕ contour shows some small changes, such as the angles in the leading edge due to *X*-axis rotation. But according to the $\Delta\phi$ plot, all the changes except the decrease in effectiveness on the leading edge are small, less than 0.05. The only change that shows up on the $\Delta\phi$ plot is the decrease in effectiveness at the spanwise edges of the leading edge.

The best case shows several improvements. The $\Delta\phi$ contour shows that most of the improvements are on the leading edge, especially in the hole cooling region upstream of the first and second rows of cooling holes. There is also a region of slightly worse cooling effectiveness downstream of the last coolant hole exit. Figure 32 also showed a -70° rotation about the *Z*-axis is the best lay-up. Because the layers are perpendicular to the holes, the cooling hole array can conduct nearly all the heat from the upper surface to the film cooling holes, thereby increasing hole cooling and increasing the overall cooling effectiveness. The average ϕ for the best case is 0.048 higher than the baseline 0/90 orientation case.

3.4. Summary

This chapter examined the effect of anisotropic thermal conductivity on a film cooled flat plate. The results show that simple one-axis rotations can have a profound effect on overall effectiveness. Compound two-axis rotations were then used to find the optimal orientation for optimizing overall effectiveness. From a practical perspective, to increase cooling performance in layered CMCs, designs should incorporate as many tows in the through-thickness direction as possible. By accomplishing these things, this chapter addressed the first two objectives. First, it compared different layups of a notional composite material to show the effect anisotropic k has on ϕ. This fulfilled the first objective of understanding the effect of anisotropic thermal

conductivity. Objective 2 was satisfied next when various ways to optimize *k* were investigated. Overall, this chapter achieved the first two objectives on a film cooled flat plate.

This page is intentionally left blank

4. Effect of Anisotropic Thermal Conductivity on a Leading Edge

A film cooled leading edge is a much different component than a flat plate. It is sufficiently different from the geometry explored in the previous chapter that it warrants a separate study. A leading edge is a difficult geometry to build using CMCs because of the small radius of the curvature. The typical layup using a textile-like preform has the primary tows along the chord and wrapping around the curvature of the edge. This technique means that the materials on the downstream surfaces would have a 0/90 flat plate geometry. As shown previously, rotating the Cartesian coordinate system is an easy way to visualize changing the orientation of layers for a flat plate geometry. The layers in the leading edge, however, are best represented using a cylindrical coordinate system. The goal of this section is to investigate whether changing the anisotropic directionality of the thermal conductivity to improve ϕ can be applied to a different geometry and layer coordinate system. This chapter also addresses the first two Objectives, but on a more practical, albeit difficult to model, geometry.

4.1. Model Description

Compared to a flat plate, the leading edge is more a complex film cooling environment to predict due to the curvature and the compound angle injection angles. There are several possibilities for the fabrication of CMC leading edge geometries. For instance, the CMC may be laid up over a mandrel such that the layers are aligned with the curvature of the surface. On the other hand, the CMC material could be laid up into a flat plate out of which the final shape is machined. Further research is needed to better understand the role of anisotropic thermal conduction on overall effectiveness for a leading edge with full coverage showerhead cooling. Using the more complex leading edge geometry allows a better quantification of the expected anisotropic thermal conductivity effects on turbine-relevant hardware.

4.1.1. Geometry

The geometry used in these simulations is a leading edge with a showerhead of film cooling holes with compound angle injection. A leading edge is a difficult geometry to build using CMCs because of the small radius of the curvature. The typical layup using a textile-like preform has the primary tows along the chord and wrapping around the curvature of the leading edge. The computational model used in the present work is a half-cylinder leading edge, replicating the geometry used experimentally in Bryant et al. [55] and based upon the geometry used by Ekkad et al. [56]. A picture of the leading edge and the associated CFD model are shown in Figure 36. Cutaway views of the model are shown in Figure 37. As indicated in these figures, the computational model was cut in half on the centerline and a symmetry boundary condition was applied on the centerline. A periodic boundary condition was modeled for the top and bottom planes of the model. The red arrows show the direction of the hot freestream, and the blue arrows show the direction of the coolant through the film cooling holes in the top and side view. In the front view, the blue arrows show the direction of the coolant as it exits the coolant holes and forms a film. They are curved because the coolant flows down through the coolant holes, then is pushed against the surface by the freestream flow.

Figure 38 shows the mesh boundary conditions. The red arrow shows the direction of the hot freestream flow and the blue arrows show the direction of the coolant flow. The solid regions are colored grey and the fluid regions are white. The model has four rows of film cooling holes in an offset array at $21.5°$ increments around the leading edge. The holes are at a $20°$ angle to the surface. The diameter of the leading cylinder is 8.89 cm and the diameter of the cooling holes is 0.48 cm, matching the dimensions of the large-scale experimental model from Ref. [55].

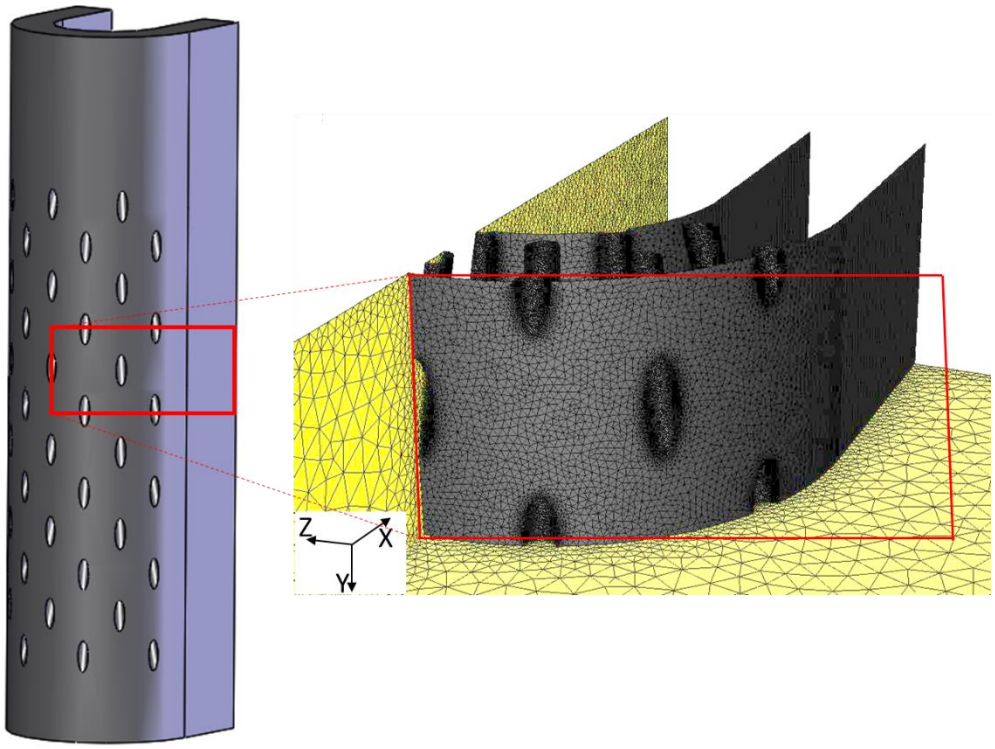

Figure 36: Close up of CFD model of the scaled-up leading edge

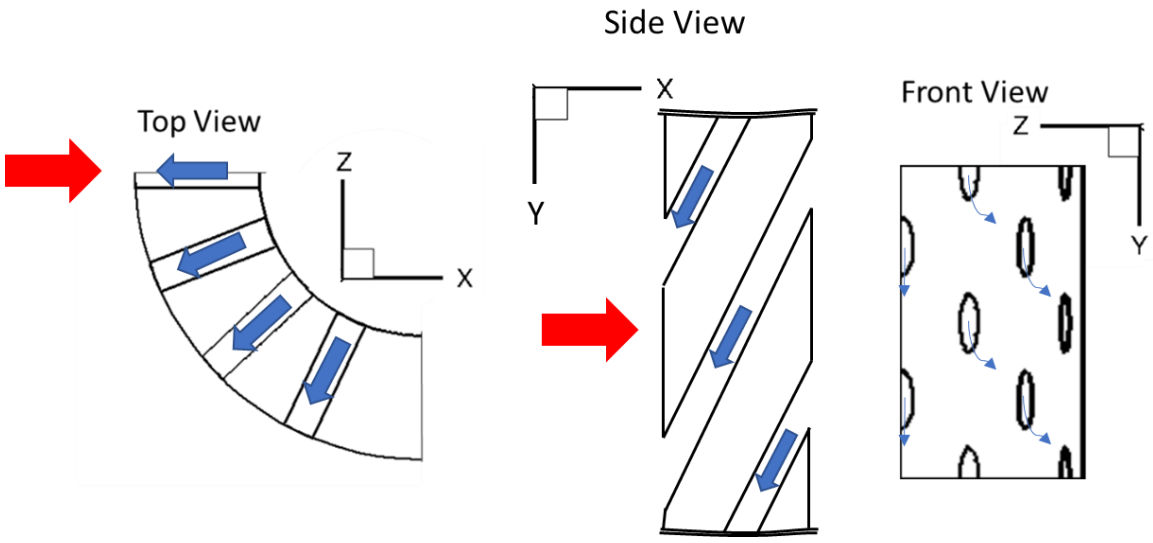

Figure 37: Leading edge model and cutaway views (d=0.49 cm)

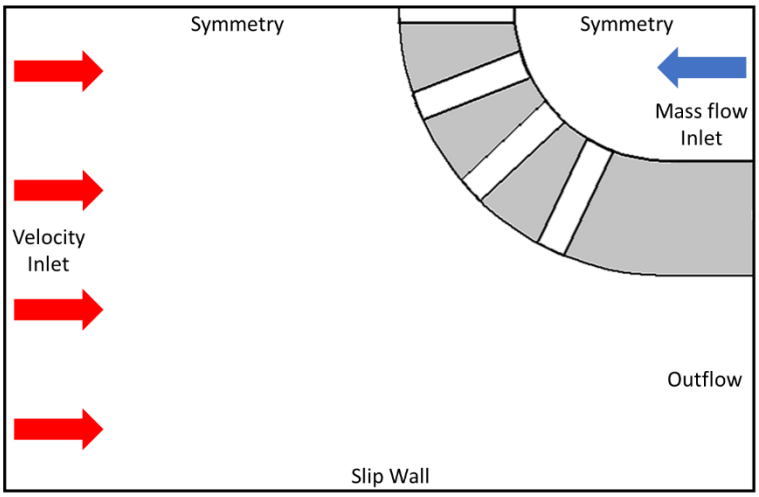

Figure 38: CFD boundary conditions

The mesh is an unstructured grid with 3 million cells. Appendix A: Computational Fluid Dynamics Procedure has additional details about the Fluent settings used. The freestream velocity is set to 12 m/s at 320 K for a Re_D = 60,000. The coolant flow is set to ACR=1.0 at 300 K for all cases except for comparison to experimental data from Ref. [55] for which the maximum ACR available was 0.9. The flow was solved in Fluent using the realizable k-ε model. The flow was incompressible at low velocities. Wall functions were utilized to model the viscous sublayer. Convergence was monitored by measuring the calculation residuals and the temperature at a few points on the surface. Once all monitors were stable and changing by less than 10^{-6} between iterations, convergence was reached. After this, the flow field was saved and used to initialize each run. Because only the k tensor within the solid was changed with each case, the flow field was relatively unaffected, so each simulation was able to converge in two hours.

4.1.2. Validation

The mesh was validated by comparing to experimental data from Ref. 55 at ACR=0.9, shown in Figure 39. In this case, the solid material thermal conductivity was set to an isotropic value of k = 1 W/m-K to match that of the Dupont Corian® physical model. The ϕ contours were generated

by unwrapping the front view of the leading-edge and nondimensionalizing the temperature distribution. In both contour plots, the freestream air flows from left to right. The coolant is traveling from the top to the bottom of the page. The experimental model shows uneven coolant flow between each row of holes, whereas the CFD simulation shows even coolant flow. Due to the uneven flow, the experiment shows an average of 0.1 higher ϕ downstream of the last cooling holes. Overall, the agreement between the experiment and computational results indicates the mesh and computational solver used are sufficient for the present purposes. Large eddy simulations (LES) would likely yield more accurate results; however, the flow field is not a variable of interest in the present study and there is no need to undergo the computational expense of LES.

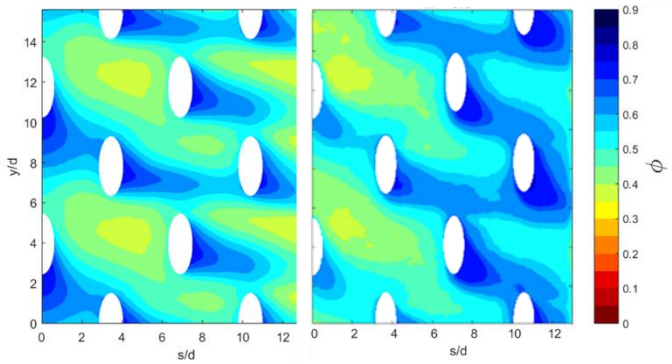

Figure 39: Comparison of CFD (left) and experiment (right) ϕ contours at ACR=0.9, from Ref. [55]

4.1.3. Coordinate Systems

The thermal conductivity of the model was set using Fluent's material property settings. Because the goal of this research is to examine anisotropy, like that found in CMCs, the thermal conductivity was modeled as if layers of material were stacked together. Within the layers, the in-plane thermal conductivity is uniform in both directions. However, the through-thickness conductivity, or the component of thermal conductivity normal to the conductive layers, is lower

by a factor of four, like the previous chapter. To discuss the thermal conductivities in higher fidelity, coordinate systems must be described.

Two global coordinate systems are defined for the leading edge model. The first is the global Cartesian coordinate system (X, Y, Z). The second is a global cylindrical coordinate system (θ, r, y), as shown in Figure 40. Typically, a cylindrical coordinate system is in a different order. This order was chosen specifically so that the baseline lay-up has an identical thermal conductivity tensor to the previous, flat plate geometry.

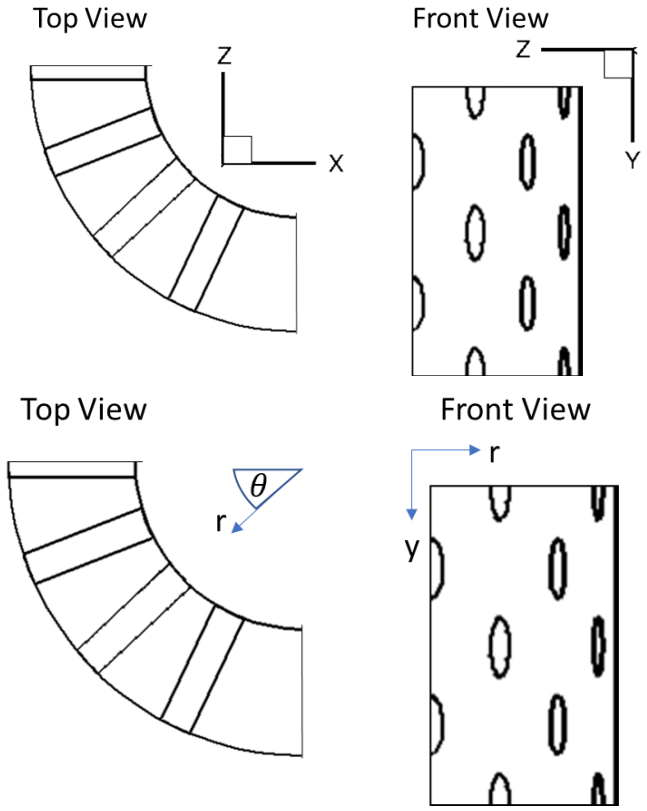

Figure 40: Coordinate systems for the model (top) Cartesian and (bottom) cylindrical

4.1. Results

The thermal conductivities were entered into Fluent using either the anisotropic material setting or the cyl-orthotropic material setting. In case of the latter, the origin and axis of rotation

were defined as the center of the plenum. The through-thickness thermal conductivity was chosen to match the experiment using Corian, k_{Thru} = 1 W/m-K and the in-plane k was chosen to be four times k_{Thru}, as suggested by Ref. [40], k_{In} = 4 W/m-k. Table 3 lists the thermal conductivities along each axis for the five cases tested. For the tangential and radial cases, the conductivity of the entire model is set using two coordinate systems. The front curved zone is set using the cyl-orthotropic coordinate system, but the flat part downstream section shown in Figure 38 is set using the orthotropic coordinate system.

Table 3: Thermal conductivity for each case

Case	***k* (W/m-K)**		
	θ	***r***	***y***
Tangential	4	1	4
Radial	1	4	4
	X	***Y***	***Z***
XZ	4	1	4
XY	4	4	1
YZ	1	4	4

4.1.1. Tangential Case

The baseline case is the first, tangential case identified in Table 3. That is, the thermal conductivity tensor is set as if the layers were aligned with the tangential direction, spanning the length of the axial direction. This orientation is the baseline case because that is the current state-of-art approach for layered CMC airfoils. If it were possible to unroll the cylindrical leading edge into a flat plate, the layers would be aligned in a standard 0/90 weave. The *k* tensor for this case is

$$k_{\theta ry} = \begin{bmatrix} 4 & 0 & 0 \\ 0 & 1 & 0 \\ 0 & 0 & 4 \end{bmatrix} \text{W/m-K} \qquad (4.1)$$

Figure 41 shows the model and ϕ contour, where the red curve shows how the layers would be aligned in this case. The horizontal axis of the contour (*s/d*) is the nondimensional distance around the leading edge from the centerline.

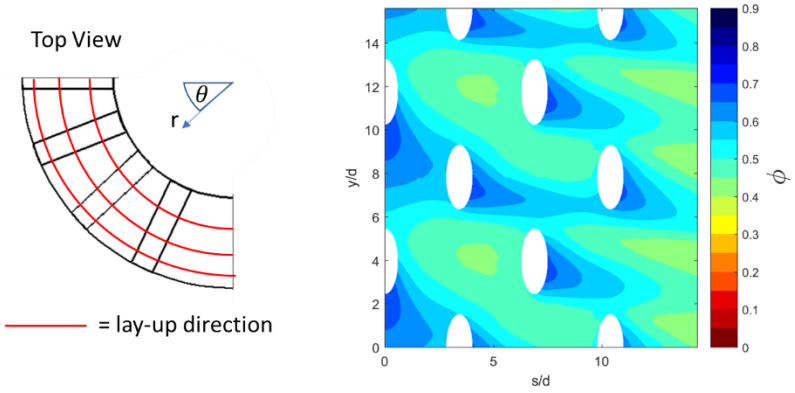

Figure 41: Tangential lay-up, orientation, and overall effectiveness

To better understand the relative influences of film cooling, internal plenum cooling, and bore hole cooling, these effects were isolated using the technique of Ref. [27]. With this technique, non-physical boundary conditions are applied to make certain internal surfaces adiabatic or remove the effect of film cooling without otherwise altering the internal flow of coolant. For instance, to remove plenum cooling, the internal surface exposed to the plenum is set to be adiabatic. To remove hole cooling, the interior surfaces of the film cooling holes are set to be adiabatic. Finally, removing film cooling is accomplished by applying pressure outlets at the exits of each of the film cooling holes such that coolant is removed from the computational domain and it does not flow over the external surface of the model, but the internal coolant flow is unaltered. Analysis of the results allows one to discern the relative importance of each form of cooling. Figure 42 shows the ϕ contours for each form of cooling removed from the baseline shown previously in Figure 41.

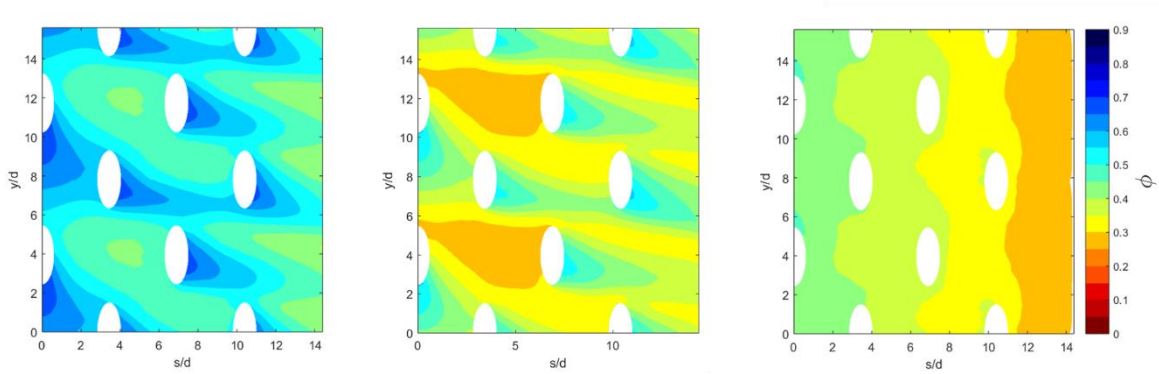

Figure 42: ϕ contours of (left) plenum cooling removed, (center) hole cooling removed, and (right) film cooling removed for the tangential lay-up

To further examine each case, $\Delta\phi$ plots were also generated. Contours of $\Delta\phi$ describe the magnitude and location of changes in overall effectiveness due to a change in the cooling scheme. Presently, the interest is in the effect of eliminating the various modes of cooling, and later the technique is used to examine the effects of rotating the thermal conductivity tensor. The $\Delta\phi$ contours for the baseline thermal conductivity tensor are shown in Figure 43. Each contour is the difference between the case with a form of cooling removed and the corresponding case without any cooling modes cooling removed. The more negative $\Delta\phi$ is, the more important that form of cooling is in that location since its elimination resulted in a decrease in ϕ. Note that the plenum cooling $\Delta\phi$ plot has a different scale than the other two plots. Examination of Figure 42 and Figure 43 shows several important aspects of this geometry. First, plenum cooling has almost no effect on the leading edge. The only area that shows a slightly negative $\Delta\phi$ is the fore part of the flat afterbody, downstream of the hole arrays. In Ref. [27], a flat plate with shaped film cooling holes, plenum cooling was only effective outside of the hole array. All the holes in the showerhead of the leading edge block the conduction path and prevent plenum cooling from having a significant effect. Hole and film cooling, therefore, are the primary methods of cooling the leading edge. Hole cooling is shown to be most effective above each hole breakout and upstream of each hole exit.

Film cooling is most effective in the areas downstream of the coolant hole exits and increases in efficacy with each row of holes due to building up the coolant layers.

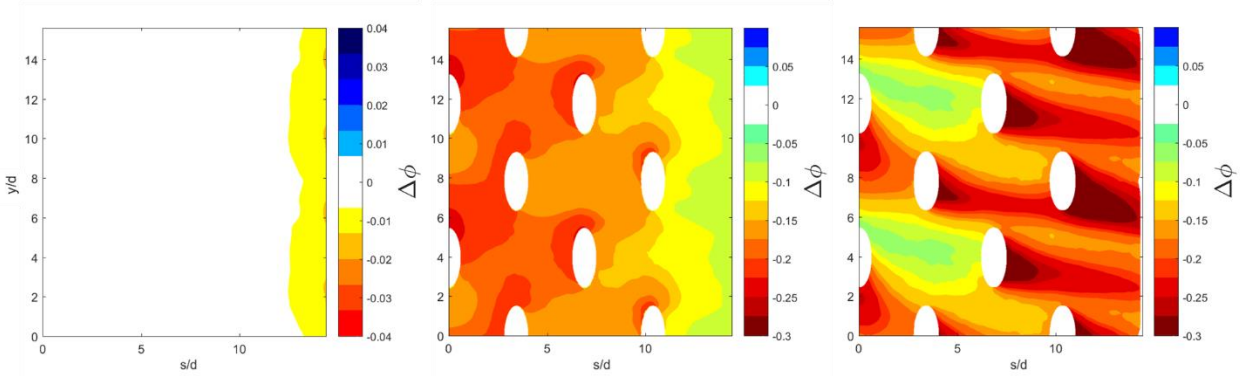

Figure 43: $\Delta\phi$ ($\phi_{cooling\ removed} - \phi$) contours for (left) plenum cooling removed, (center) hole cooling removed, and (right) film cooling removed for the baseline case

4.1.2. Radial Case

The next case orients the layers with the same 0/90 weave to be aligned radially instead of tangentially. The resulting *k* tensor in the cylindrical coordinate system is

$$k_{\theta ry} = \begin{bmatrix} 1 & 0 & 0 \\ 0 & 4 & 0 \\ 0 & 0 & 4 \end{bmatrix} \text{W/m-K} \qquad (4.2)$$

and the resulting ϕ distribution is shown in Figure 44. Also shown is the $\Delta\phi$ plot which demonstrates the difference between the radial and baseline lay-up ($\phi_{radial} - \phi_{baseline}$). Compared to the baseline, ϕ is increased by approximately 0.1 between holes in the first few rows. There is little improvement in the coolant plumes and a slight decrease in effectiveness where the curved leading edge transitions to the flat afterbody.

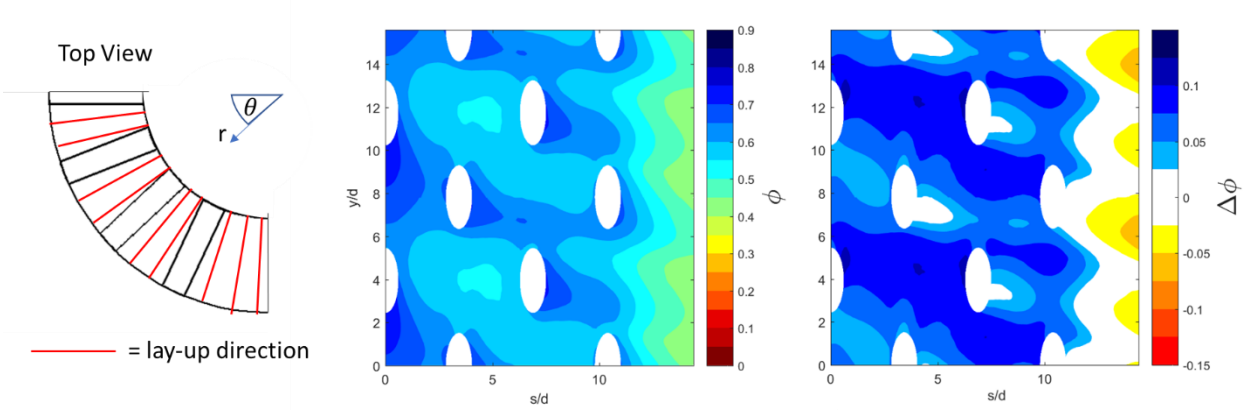

Figure 44: Radial lay-up orientation, ϕ, and $\Delta\phi$ ($\phi_{radial} - \phi_{baseline}$)

Figure 45 shows the ϕ plots and Figure 46 shows the $\Delta\phi$ plots describing the effect of removing the three cooling modes for this case. Once again, plenum cooling has a negligible contribution compared to hole cooling and film cooling. However, compared to Figure 43, hole cooling in the present situation has greater importance and film cooling is less important. The area directly above the cooling holes is thin-walled due to the cooling hole beneath the surface about to break through. Because the layers are oriented perpendicularly to the surface, they facilitate increased heat transfer to the coolant and plenum walls (thereby increasing hole and plenum cooling effectiveness) and warming the coolant within (thereby decreasing the benefit of film cooling). This is particularly clear in the stagnation region because that is the area with the most energy transfer.

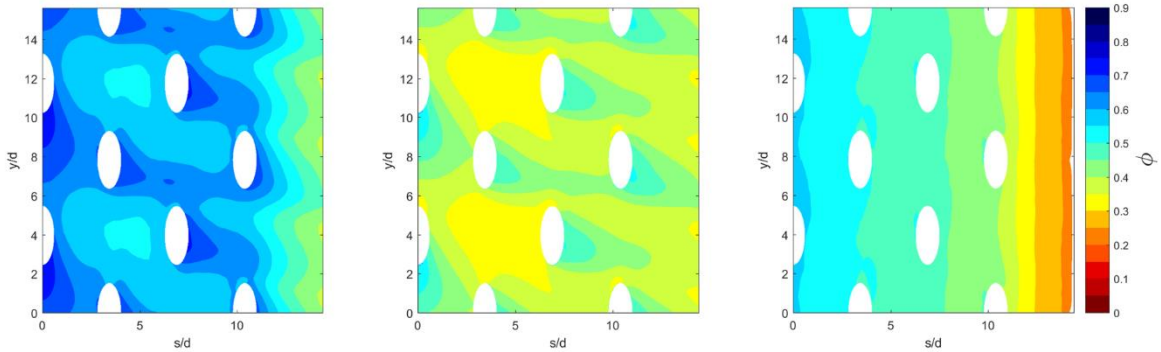

Figure 45: ϕ contours of (left) plenum cooling removed, (center) hole cooling removed, and (right) film cooling removed for the radial lay-up

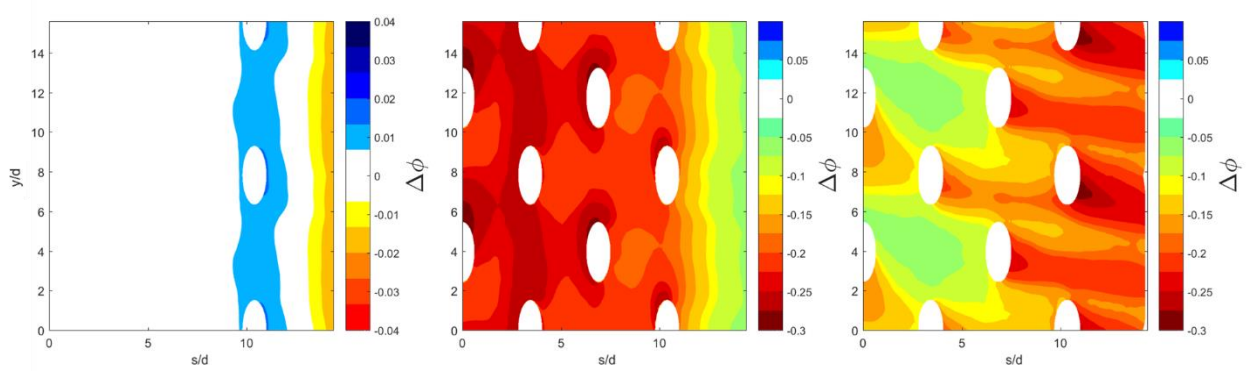

Figure 46: $\Delta\phi$ ($\phi_{cooling\ removed} - \phi$) contours for (left) plenum cooling removed, (center) hole cooling removed, and (right) film cooling removed for the radial lay-up

4.1.3. XZ Case

The next three cases orient the layers in the Cartesian coordinate system (*X*, *Y*, *Z*) system. For all three cases in this coordinate system, one plane has increased thermal conductivity. The layers are oriented parallel to that plane. The first case has layers aligned with the *XZ* plane. The *k* tensor is

$$k_{XYZ} = \begin{bmatrix} 4 & 0 & 0 \\ 0 & 1 & 0 \\ 0 & 0 & 4 \end{bmatrix} \text{W/m-K} \qquad (4.3)$$

and the model orientation, ϕ, and $\Delta\phi$ contours are shown in Figure 47. The ϕ contours are shown in Figure 48 and the $\Delta\phi$ contours for each type of cooling removed are shown in Figure 49. Like the radial orientation, this case is also much more effective than the baseline, tangential case. The shape of the contours is like the baseline, but generally between $\Delta\phi$ = 0.05 – 0.10 higher. Because the layers are perpendicular to the surface, they create a conduction path directly from the plenum to the outside surface. Heat travels perpendicular to the surface, directly to the cool plenum and film holes via the layers, increasing cooling on the outside surface. Unlike the radial case (where the layers were also perpendicular, but vertically aligned), the cooling effect is spread more by conduction in the horizontal direction, along the *XZ* plane.

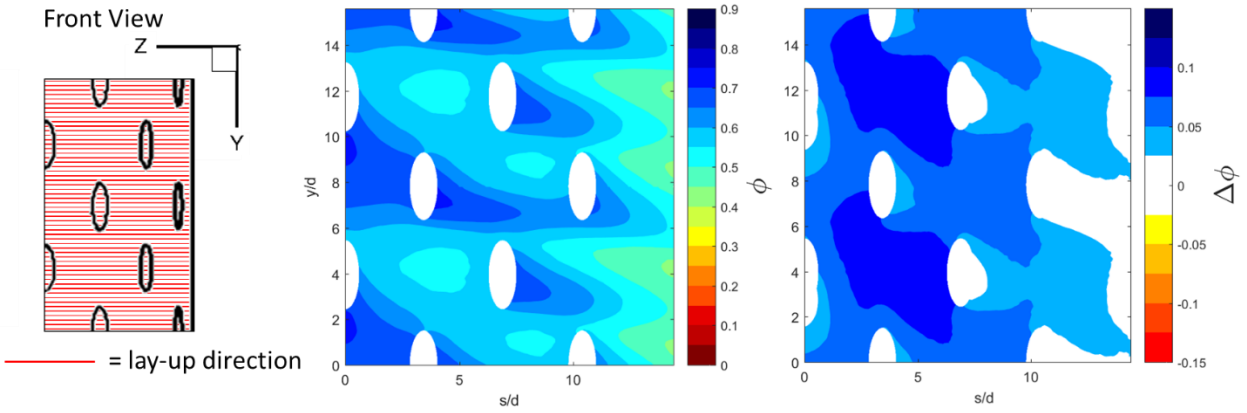

Figure 47: XZ plane lay-up orientation, ϕ, and $\Delta\phi$ ($\phi_{rotated} - \phi_{baseline}$)

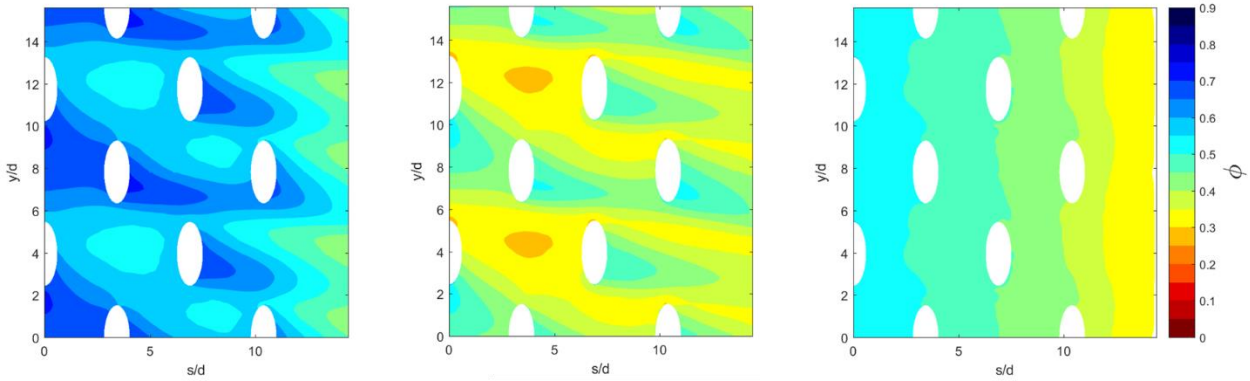

Figure 48: ϕ contours of (left) plenum cooling removed, (center) hole cooling removed, and (right) film cooling removed for the XZ plane lay-up

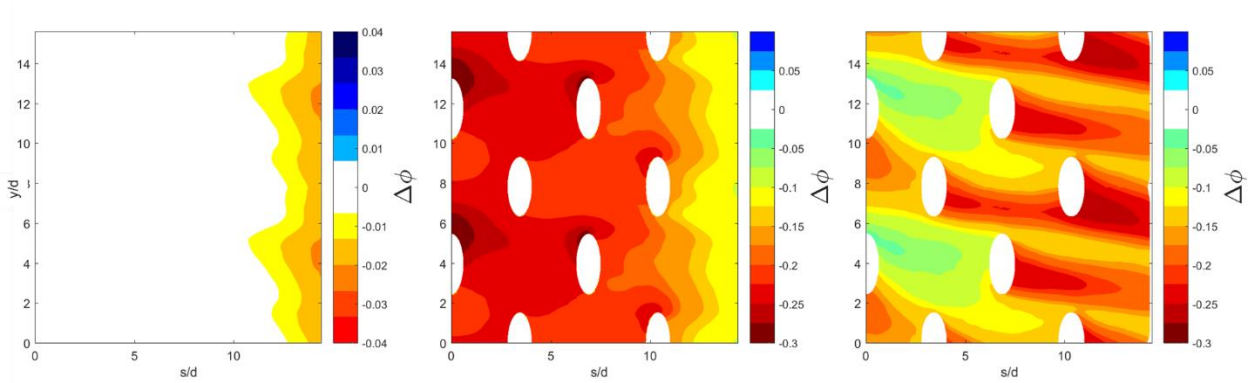

Figure 49: $\Delta\phi$ ($\phi_{cooling\ removed} - \phi$) contours for (left) plenum cooling removed, (center) hole cooling removed, and (right) film cooling removed for the XZ plane lay-up

4.1.4. XY Case

The next case has the layers aligned with the XY plane, parallel to both the hot freestream and coolant in the plenum. The *k* tensor is

$$k_{XYZ} = \begin{bmatrix} 4 & 0 & 0 \\ 0 & 4 & 0 \\ 0 & 0 & 1 \end{bmatrix} \text{W/m-K} \tag{4.4}$$

and the model orientation, ϕ, and $\Delta\phi$ contours are shown in Figure 50. The ϕ contours are shown in Figure 51 and the $\Delta\phi$ contours for each type of cooling removed are shown in Figure 52. Compared to the baseline case, this case has increased ϕ in the first two rows of film cooling holes, but at the expense of decreased ϕ in the last row and downstream. Along the centerline, the layers are generally aligned radially and conduct almost directly through the leading edge from a region with very high film effectiveness. Compared to the case with radial layers, Figure 44, the present case has higher effectiveness. Further downstream, the layers are aligned nearly tangentially, therefore, these layers act as almost an insulator to keep the highly effective first row of holes cool, without allowing the downstream layers to conduct their heat to the first row. The downside of this is that it impedes the flow of heat in the last row of cooling holes to travel across the layers to the cooler first row of holes, therefore that region is hotter. With a diminished benefit of conduction there, film cooling becomes far more important as evident in the $\Delta\phi$ distribution for the film cooling removed case.

4.1.5. YZ Case

The last case has layers aligned perpendicular to the freestream, along the *YZ* plane. The *k* tensor is

$$k_{XYZ} = \begin{bmatrix} 1 & 0 & 0 \\ 0 & 4 & 0 \\ 0 & 0 & 4 \end{bmatrix} \text{W/m-K} \tag{4.5}$$

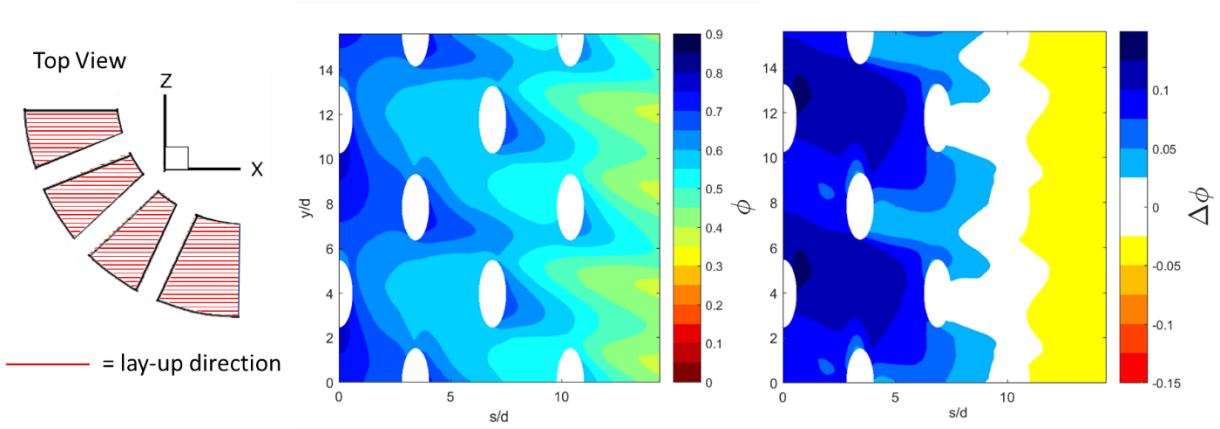

Figure 50: XY plane lay-up orientation, ϕ, and $\Delta\phi$ ($\phi_{rotated} - \phi_{baseline}$)

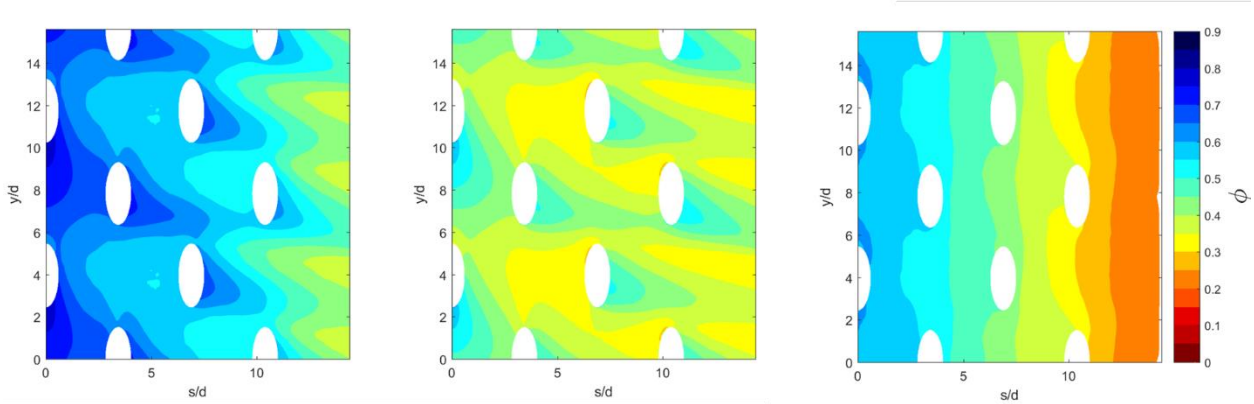

Figure 51: ϕ contours of (left) plenum cooling removed, (center) hole cooling removed, and (right) film cooling removed for the XY plane lay-up

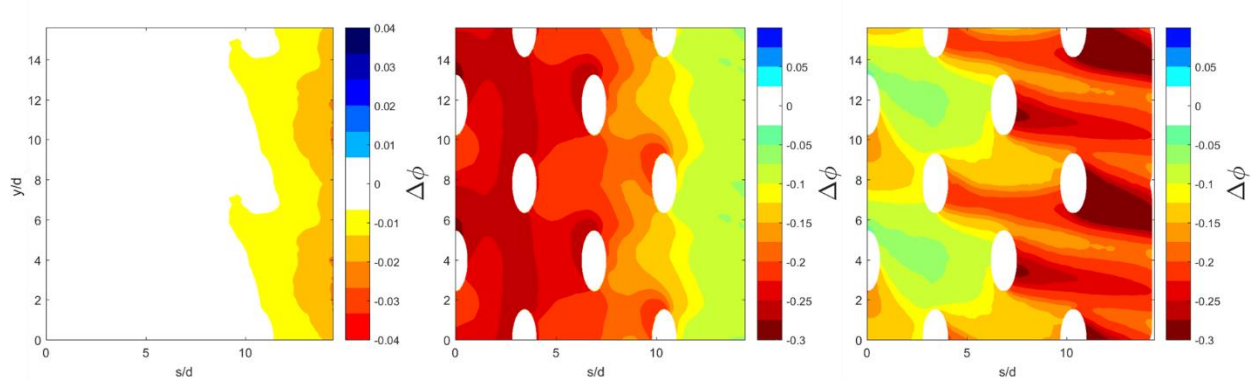

Figure 52: $\Delta\phi$ ($\phi_{cooling\ removed} - \phi$) contours for (left) plenum cooling removed, (center) hole cooling removed, and (right) film cooling removed for the XY plane lay-up

and the model orientation, ϕ, and $\Delta\phi$ contours are shown in Figure 53. The ϕ contours are shown in Figure 54 and the $\Delta\phi$ contours for each type of cooling removed are shown in Figure 55. In a

sense, this case is nearly the opposite of the previous case, because the first two rows of cooling holes have lower effectiveness, but the last two rows have higher ϕ. The reason for this is that the layers towards the back intersect the plenum. The layers in front never intersect the plenum, so they can only conduct heat to the other film cooling holes, much like the baseline case. The effectiveness for the first two rows of holes looks like the baseline case (Figure 41), whereas the last two rows behave more like the radial case (Figure 44).

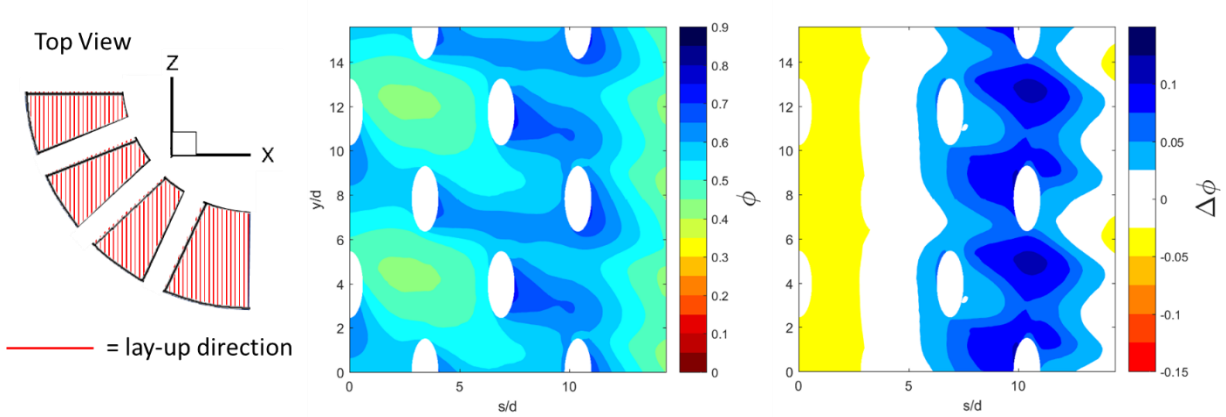

Figure 53: YZ plane lay-up orientation, ϕ, and $\Delta\phi$ ($\phi_{rotated} - \phi_{baseline}$)

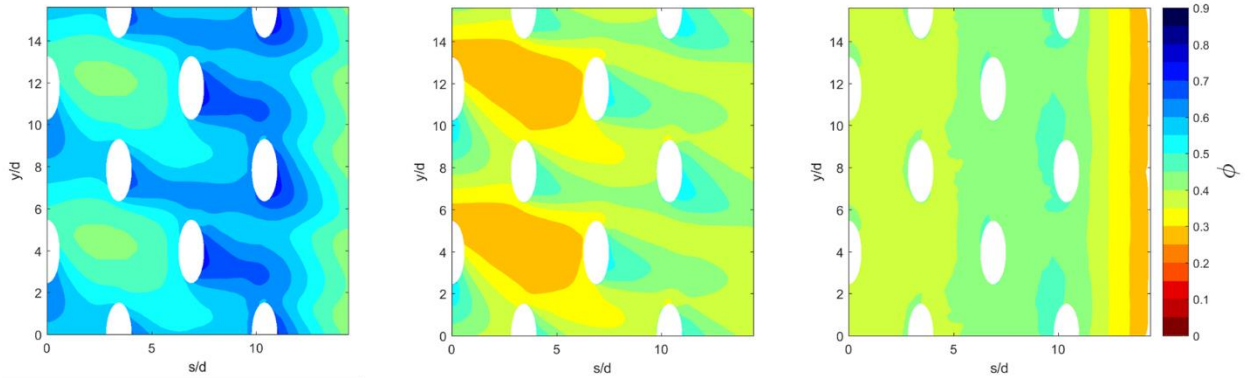

Figure 54: ϕ contours of (left) plenum cooling removed, (center) hole cooling removed, and (right) film cooling removed for the YZ plane lay-up

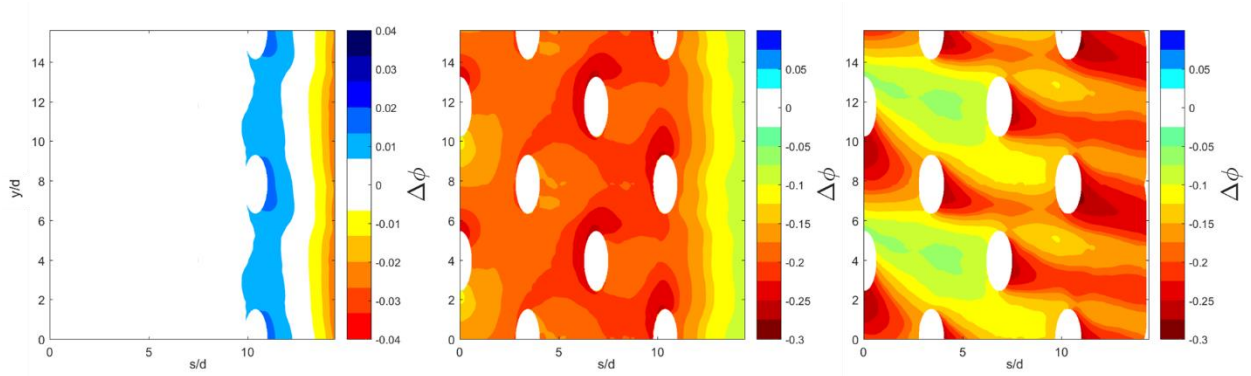

Figure 55: $\Delta\phi$ ($\phi_{cooling\ removed} - \phi$) contours for (left) plenum cooling removed, (center) hole cooling removed, and (right) film cooling removed for the YZ plane lay-up

4.1.6. Case Summaries

To review, the layers on a semi-cylindrical leading edge have been varied and the resulting ϕ distributions have been analyzed. It is apparent that orienting the tows in the thru-thickness direction results in increases in ϕ because conduction is increased to the plenum. Orienting the layers so that they also intersected several holes also increased the conduction of heat between holes, further cooling the external surface. Figure 56 shows the area-averaged $\Delta\phi$ for each type of cooling removed in each case. In all five cases, plenum cooling is ineffective due to the showerhead blocking conduction. In every case besides the baseline case, hole cooling is more effective than film cooling. Hole cooling particularly increased in the radial and XZ lay-ups, which also have an average $\Delta\phi = 0.05$ higher than the baseline case.

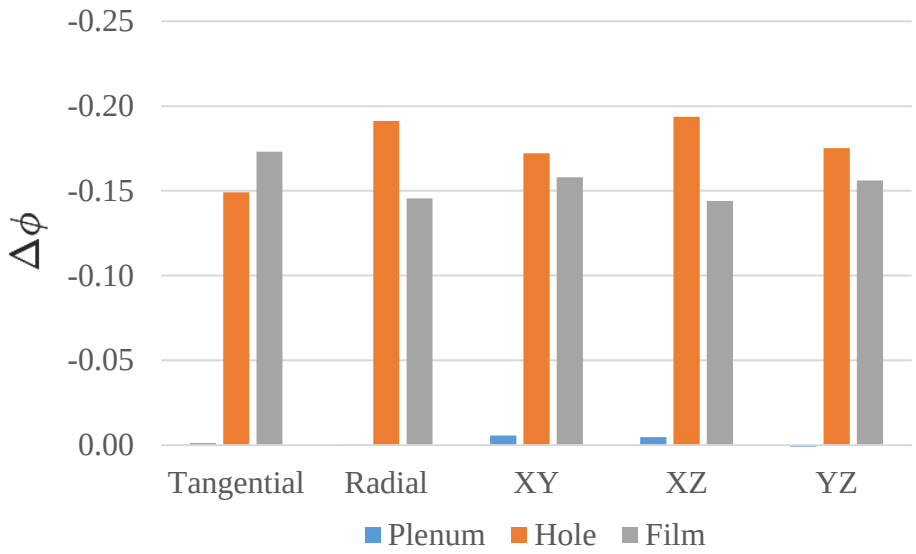

Figure 56: Area Average $\Delta\phi$ ($\phi_{cooling\ removed} - \phi$) for each type of cooling removed and each case

Although it is not possible to directly equate ϕ contours between iso- and anisotropic materials, one may compare the maximum and minimum values that comprise the anisotropic tensor. Figure 57 shows four contours--the left is isotropic $k = 1$ W/m-K, the next is the baseline tangential lay-up previously discussed, the center-right is the radial case, and the last contour is isotropic $k = 4$ W/m-K. Comparing the two plots on the left to the two plots on the right, it is evident that the effect of changing just the position of the one in the k tensor is nearly equal to the effect of multiplying the thermal conductivity of the material by four. This is because radial tows in the radial lay-up provide a conduction path between the outer surface and the inner surface and the cooling holes. Additionally, $k_{\theta\theta} = 1$ acts as insulator, thereby keeping the entire plate cooler, but in the tangential case $k_{rr} = 1$ insulates the outside surface, preventing heat from dissipating by flowing to the coolant holes.

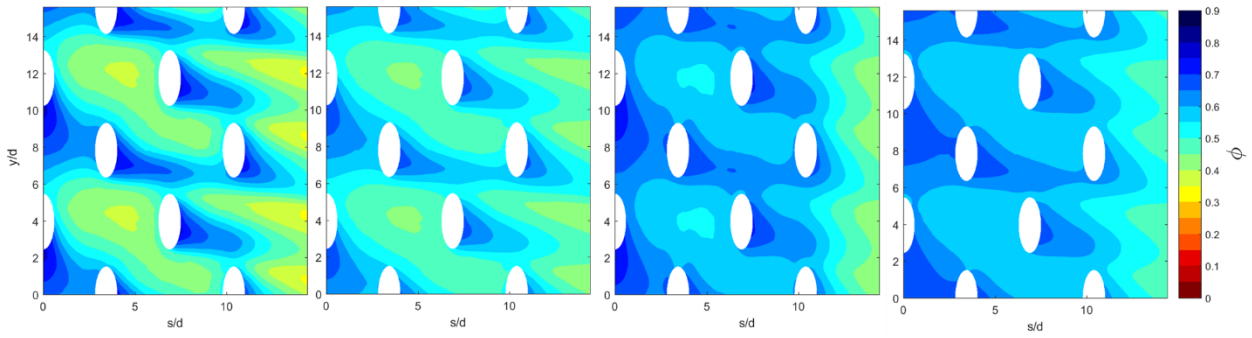

$k_{r\theta y} = \begin{bmatrix} 1 & 0 & 0 \\ 0 & 1 & 0 \\ 0 & 0 & 1 \end{bmatrix}$ $k_{\theta ry} = \begin{bmatrix} 4 & 0 & 0 \\ 0 & 1 & 0 \\ 0 & 0 & 4 \end{bmatrix}$ $k_{\theta ry} = \begin{bmatrix} 1 & 0 & 0 \\ 0 & 4 & 0 \\ 0 & 0 & 4 \end{bmatrix}$ $k_{r\theta y} = \begin{bmatrix} 4 & 0 & 0 \\ 0 & 4 & 0 \\ 0 & 0 & 4 \end{bmatrix}$ W/m-K

Figure 57: Effect of changing the k tensor (from left to right): k=1 W/m-K, tangential lay-up, radial lay-up, k=4 W/m-K

4.2. Summary

Overall, this chapter confirmed the findings of the previous chapter, on a more complex geometry. Lay-ups with tows that intersected coolant holes resulted in the highest overall effectiveness. Additionally, a high degree of curvature resulted in a large disparity in overall effectiveness if the lay-ups were not also curved. This technique of identifying the best lay-ups for various locations could be used to tailor the CMC lay-up of any film-cooled part in a gas turbine engine. This chapter also addressed the first two research objectives. The first objective was to investigate the effect of anisotropic k on ϕ. This was accomplished by comparing the effects of different notional composite lay-ups in two different coordinate systems. The second objective was to find ways to increase ϕ by leveraging the anisotropic k. Unlike the previous chapter that showed an optimized lay-up orientation, this objective was completed by comparing different lay-ups and coordinate systems. The anisotropic lay-ups were also compared to isotropic materials to show the effect of rotating the lay-ups.

This page is intentionally left blank

5. Scaling Biot Number Effects

Thus far, every simulation has been conducted at a lower temperature than the hot section of a gas turbine engine, where CMC parts are utilized. There are many advantages to testing at a lower temperature, such as ease of optical access for IR measurements and no risk of a test article or instrumentation melting. However, the primary disadvantage is that it is known that ϕ values at laboratory conditions do not necessarily correspond with ϕ values at engine conditions. The term scaling refers to relating and comparing results at one condition to another, in this case, between low and high temperatures.

There are several aspects of scaling which must be addressed. As discussed in Chapter 2, previous scaling research work was primarily focused on coolant flowrate for scaling η and matching the Biot number for scaling ϕ. Other factors such as the ratio of heat transfer coefficients and the thermal conductivity of both the coolant and solid material are key to finding ϕ, as shown in Eq. (2.17). Add anisotropic thermal conductivity to that complexity and scaling ϕ becomes even more intricate. The purpose of the next several chapters is to answer Objective 3 by exploring the complicated nature of scaling ϕ with the goal of better understanding how laboratory ϕ experiments scale to engine conditions.

The first step to understanding how to scale ϕ with CMCs is to understand how conduction from internal cooling is scaled. Because anisotropic materials conduct heat differently than isotropic materials, and the *k* tensors are temperature dependent, CFD analysis is required to isolate the effects of anisotropy. The results from this describe how to scale anisotropic ϕ results from laboratory to engine conditions. The same CFD model from Chapter 3, the flat plate, is used once more. The *k* tensor is modified to match real CMC's thermal conductivity at various laboratory conditions.

5.1 Analysis

Unlike typical Nickel-based superalloys, ceramic matrix composite materials have anisotropic thermal conductivity due to the directional tows within the material. Therefore, for an anisotropic solid, the heat flux is not necessarily aligned with the temperature gradient [42]. Notably, in the present context of scaling experiments through matching the Biot number, the thermal conductivity tensor, as shown in Eq. (2.30), gives rise to a Biot number tensor:

$$\overline{\overline{\boldsymbol{Bi}}} = \frac{hL}{\overline{\overline{\boldsymbol{k}}}} \tag{5.1}$$

Little research has been done on the effects of anisotropic conduction on overall cooling effectiveness. While most research on CMCs for film cooling applications has focused on material strength and durability (cf. Refs. 57 and 58), the impact of anisotropy on turbine cooling is an area of emerging interest. The computational work of Ref. 59 shows that the selection of lay-up direction in a CMC can have a strong influence on the resulting temperature distribution on a film cooled turbine component. A few studies have examined the effect of anisotropic thermal conductivity on film cooling effectiveness at laboratory conditions (Refs. 48 and 49); however, further research is needed to understand how these results scale to engine conditions. Identifying and quantifying the impact of mismatched Biot numbers leads to better predictions of the thermal state of composite components at engine-relevant conditions.

5.1.1. Inconel 718

The methodology used to determine Biot number error is like the method of Stewart and Dyson [20]. Consider the engine and laboratory conditions shown in Table 4. The density ratio at both conditions is approximately $DR = 2.0$. To match the ratio shown in Eq. (2.26), the ratio of the freestream air thermal conductivity to the solid material thermal conductivity must be matched. Figure 58 shows that both the thermal conductivity of air [60] and Inconel 718 [61]

increase with temperature. Note that air's *k* is shown on a separate axis on the right side of the graph.

Table 4: Notional engine and laboratory thermal conditions for $\bar{\phi} = 0.6$

	Freestream T (K)	Coolant T (K)	Material T (K)
Engine Condition	2000	1000	1400
Lab Condition	500	250	350

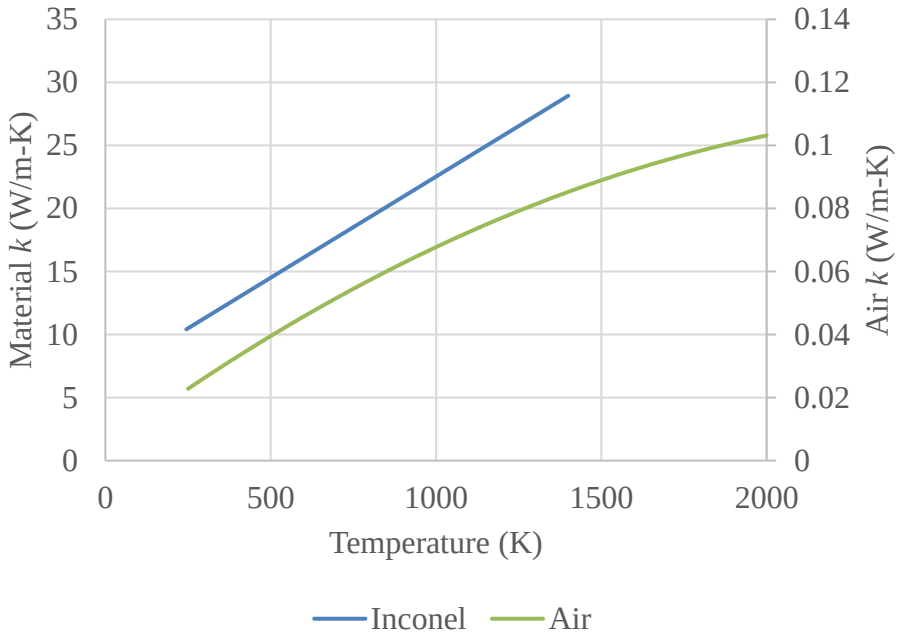

Figure 58: Thermal conductivity variation of air and Inconel 718 with temperature

With further knowledge of ϕ, the surface temperature can be determined and therefore the Biot number error. Naturally, a mismatch in Biot number would cause the ϕ value measured at lower temperatures to differ somewhat from the engine condition value. This is precisely a situation to avoid, but the relationship between the Biot number error and the error in ϕ is also a function of other parameters, such as η and $\frac{h}{h_i}$, as indicated in Eq. (2.17). Both of those parameters tend to have large spatial variation and dependence on geometry, so making

assumptions about those values would be fruitless. For the sake of predicting Biot number error, ϕ is assumed to be invariant with temperature. First, the Biot number error is determined if ϕ is invariant, which could then be used to predict the actual error in ϕ for a particular combination of η and $\frac{h}{h_i}$ in Eq. (2.17). $\bar{\phi} = 0.6$ is used as a typical value [62].

The Biot number error is quantified by

$$Bi\ error = \frac{Bi_{lab} - Bi_{eng}}{Bi_{eng}} \tag{5.2}$$

Note that the sign of Eq. (5.2) is the reverse of that used by Stewart and Dyson [20]. If the thermal conductivity of a material at laboratory condition is higher than desired, it would result in a Biot number that is too low for the experiment to properly match the engine conditions in a laboratory experiment. The freestream thermal conductivity decreases by a factor of approximately 2.9 from the engine to the lab condition in Table 4. Therefore, for the Biot number to be matched, it would be desired that the thermal conductivity of the material should also decrease by a factor of 2.9. However, Inconel's thermal conductivity decreases by a factor of only 2.4 from the engine condition to the lab condition and therefore leads to a Biot number in the lab that is 17% lower than the Biot number at engine condition. Figure 59 shows the Biot number error for a range of laboratory conditions. The analysis here differs from Ref. [20] likely due to the use of different material and fluid properties.

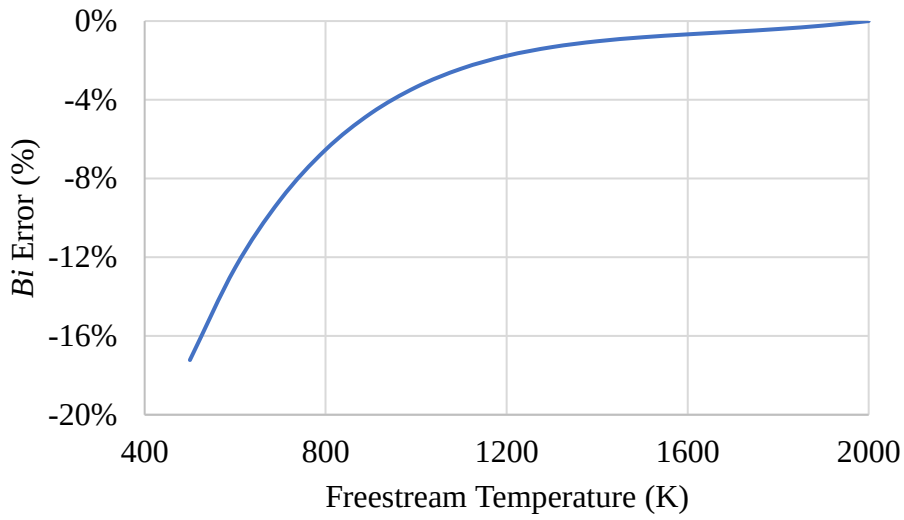

Figure 59: Error in Biot number using Inconel for a range of lab conditions for which $T_\infty/T_c = 2$ and $\bar{\phi} = 0.6$

One may use Eq. (2.17) to estimate the effect that a 17% reduction on Biot number would have on the measured value of ϕ. By assuming a worst case scenario of η = 0 and typical values of *Bi* = 0.5 (c.f. Refs. 21 and 7), χ = 0.9 (Ref. 63) and $\frac{h}{h_i}$ = 1.7 (Ref. 21), the error in ϕ caused by an undesired reduction of *Bi* by 17% is only a $\phi = 0.009$ increase. If η = 0.5, this error in ϕ drops to a 0.005 increase. Section 5.2 will address this aspect more thoroughly through CFD simulations that do not require these assumptions. Nevertheless, it is quite apparent that Inconel's fortuitous thermal conductivity variation allows for the turbine community to use it for low-temperature testing that gives ϕ values that are meaningful to the high temperature condition. The next three sections examine emerging composite materials for which *Bi* error has not yet been demonstrated, or perhaps even considered.

5.1.2. SiC/SiC CMC

Several relevant composite materials with anisotropic thermal conductivity were examined using the same method used previously with Inconel. The first CMC is a melt infiltrated silicon

carbide-silicon carbide ceramic matrix composite (SiC/SiC CMC). This class of material is typically used for high-temperature components with potential applications including turbine engine hot gas path components and thermal protection systems. Figure 60 shows the thermal conductivity of the material compared to air. Note that two conductivities are shown. The parallel thermal conductivity refers to the *k* component(s) aligned with the tows in the material. This may be one of two directions depending on the lay-up of the material, whether it consists of uni-directional long tows or a 2D textile-like weave. The transverse thermal conductivity refers to the *k* components perpendicular to the tows. Again, this may be one or two directions depending on the lay-up. This parallel component of *k* is higher because the tows have a higher *k* than the matrix. Of significance to the present interest in matching Biot number, the thermal conductivity variation is unlike air in that both *k* components *decrease* with temperature. Notice also that even the ratio of the two components of *k* changes with temperature. These two unfortunate features of *k* behavior might be expected to have deleterious effects on the experimentalist's ability to match Biot number and warrant further examination that is presented in Section 5.2.4.

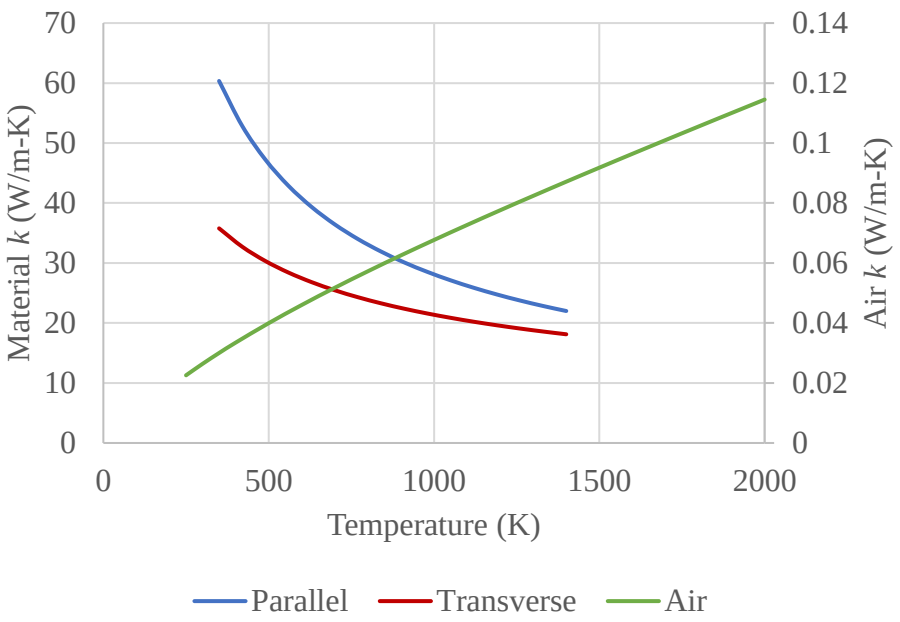

Figure 60: Thermal conductivity of SiC/SiC CMC compared to Air, $\bar{\phi} = 0.6$

The Biot number error for the SiC/SiC CMC is plotted in Figure 61. At low temperature, the error is high: -87% in the parallel direction and -82% in the transverse direction. The error increases nearly linearly to engine conditions. The error in *Bi* is slightly more negative for the parallel *k* because it increases even more rapidly with a drop in temperature than the transverse *k* as evident in Figure 60. The primary takeaway from this case is heat transfer testing this type of SiC/SiC CMC parts at low temperature yields overall effectiveness corrupted to some degree due to a high Biot number error.

As was done with Inconel. Eq. (2.17) is used to estimate the effect that a % reduction on Biot number would have on the measured value of ϕ. In the worst case scenario, of η = 0, the error in ϕ caused by an undesired reduction of *Bi* by 87% is 0.049 and by 82% is 0.046. If η = 0.5, this error in ϕ drops to 0.027 in the parallel direction and 0.025 in the transverse direction. That's nearly five times the estimated change with Inconel. It is also worth noting that the present analysis assumes a ϕ distribution that is invariant with temperature, but the reality is that if the

Biot number is too low at lab conditions, it results in a cooler surface than desired, which would exacerbate the Biot number error with the SiC/SiC CMC. Both thermal conductivities are quite sensitive to temperature and increase with decreasing temperature. This contrasts with Inconel which has $\frac{\partial k}{\partial T} > 0$, and therefore tends to have a somewhat self-correcting effect. For this reason, the experimentalist is cautioned in the interpretation of laboratory-obtained overall effectiveness data with SiC/SiC CMC components. Further analysis of the extent of the error in ϕ is examined via CFD in Section 5.2.4.

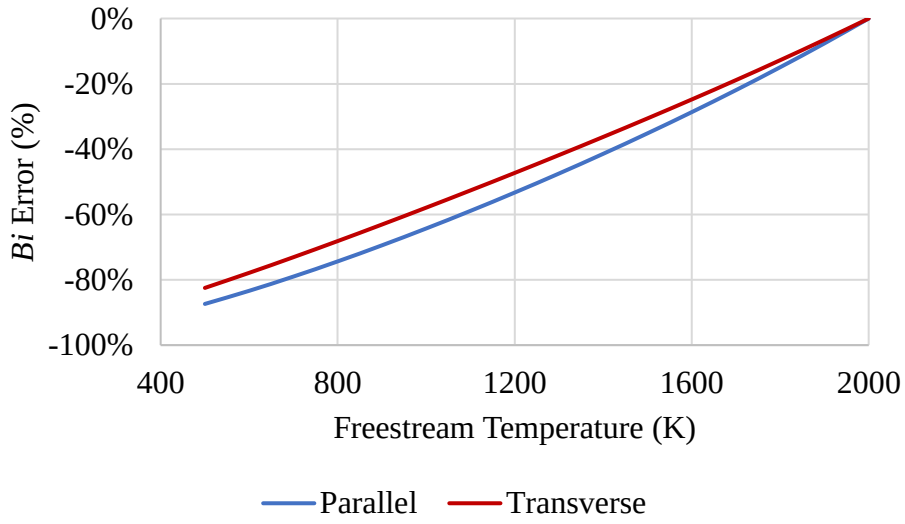

Figure 61: Error in Biot number with a SiC/SiC CMC for a range of lab conditions, $\bar{\phi} = 0.6$

5.1.3. C_f-UHTCMCs

The next class of materials examined are carbon fiber-based ultra-high temperature ceramic matrix composites (C_f-UHTCMCs), discussed in Ref. 64. These are carbon/carbon composite materials with advanced temperature capabilities, currently being developed for use in key components such as rocket nozzles and leading edges of high-speed vehicles. Figure 62 shows the thermal conductivity of this material compared to air. Unlike what was observed with

SiC/SiC CMCs, the thermal conductivities of C_f-UHTCMCs are not strong functions of temperature.

Figure 63 shows the resulting Biot number error for C_f-UHTCMCs. At lab condition, the error is -50% in the parallel direction and -59% in the transverse direction. Note that, unlike the SiC/SiC material, the transverse component of the *Bi* error is more negative than the parallel component for this material. The slope is similar to the SiC/SiC CMC and the error is also negative because the thermal conductivity at lower temperatures does not decrease proportionally with air, as is required by Eq. (2.26). The impact on ϕ is discussed in Section 5.2.5.

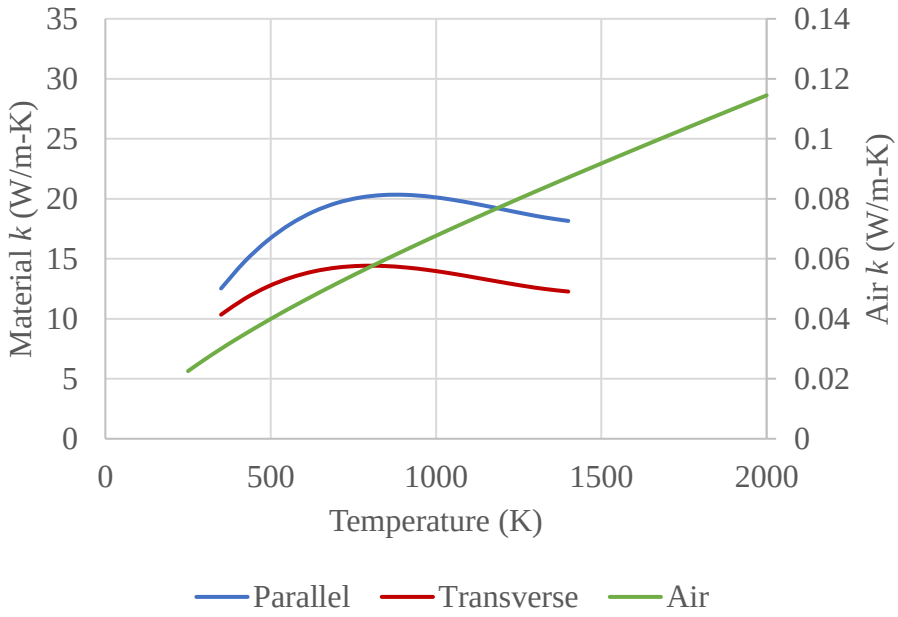

Figure 62: Thermal conductivity of C_f-UHTCMCs compared to Air

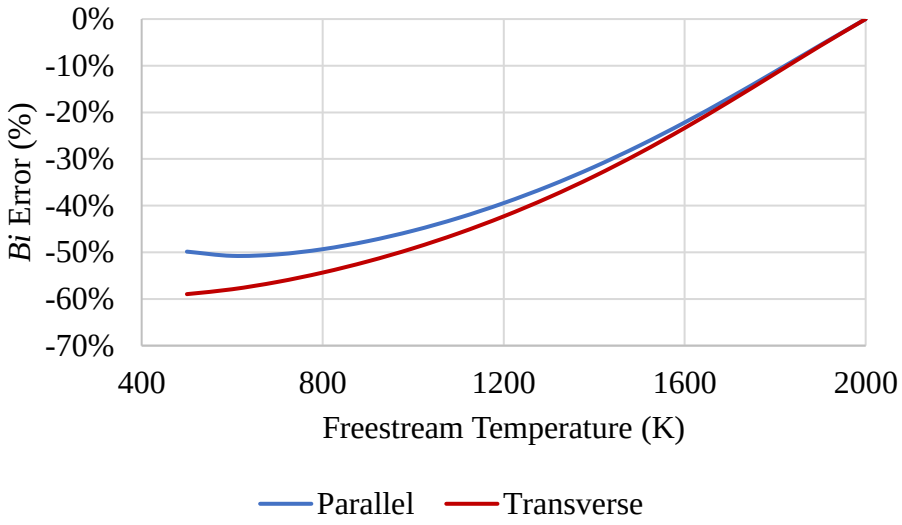

Figure 63: Error in Biot number with C_f-UHTCMCs for a range of lab conditions, $\bar{\phi} = 0.6$

5.1.4. PSCs

The final class of materials examined are polysialate composites (PSC) from Ref. 65. PSCs are neither ceramic nor polymer matrix composites, but are lightweight composites used in heat shield applications, and potentially high temperature structural applications. PSC's thermal conductivity increases with temperature, as shown in Figure 64. Both conductivities follow the same trend: at low temperature *k* is nearly constant, then gradually increases with temperature. Figure 65 shows the expected Biot number error for PSC. The error in the parallel component is -55% and -51% in the transverse component at the lab condition.

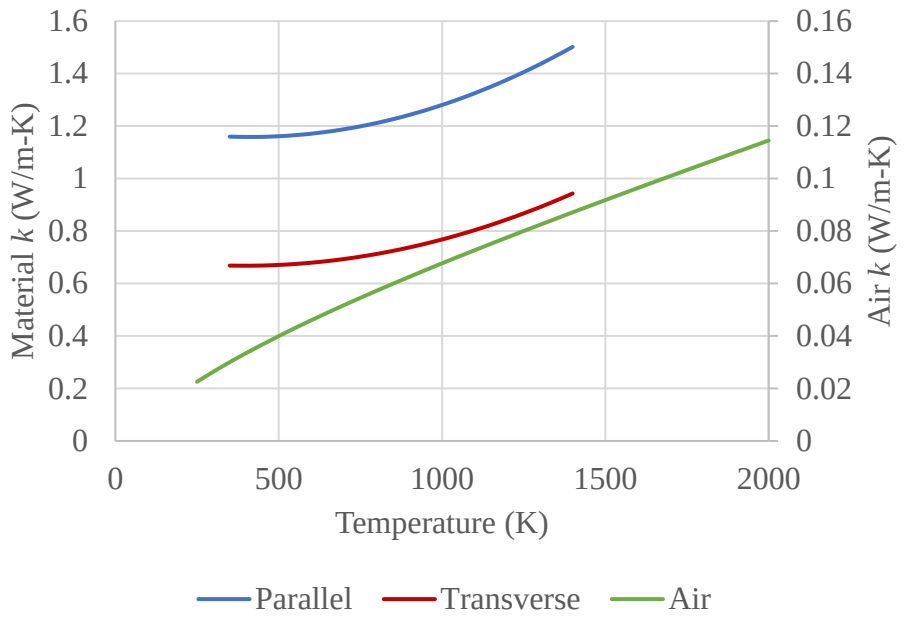

Figure 64: Thermal conductivity of PSC compared to Air

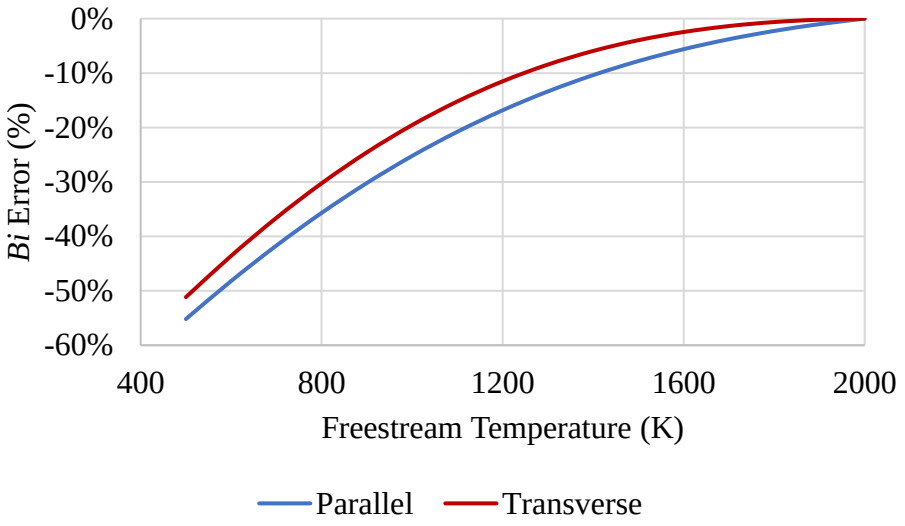

Figure 65: Error in Biot number with PSC for a range of lab conditions, $\bar{\phi} = 0.6$

Figure 66 is a comparison of all three composite materials previously discussed, compared to Inconel 718. All three composites show large negative errors (<-50%) at low temperatures, where laboratory tests typically take place. Experimentalists must examine the thermal conductivity of the composites tested at low temperatures because these data show a high

likelihood of a mismatched Biot number. How the error in Biot number corresponds to an error in the measured overall effectiveness has not yet been established and is the focus of the next section of this chapter.

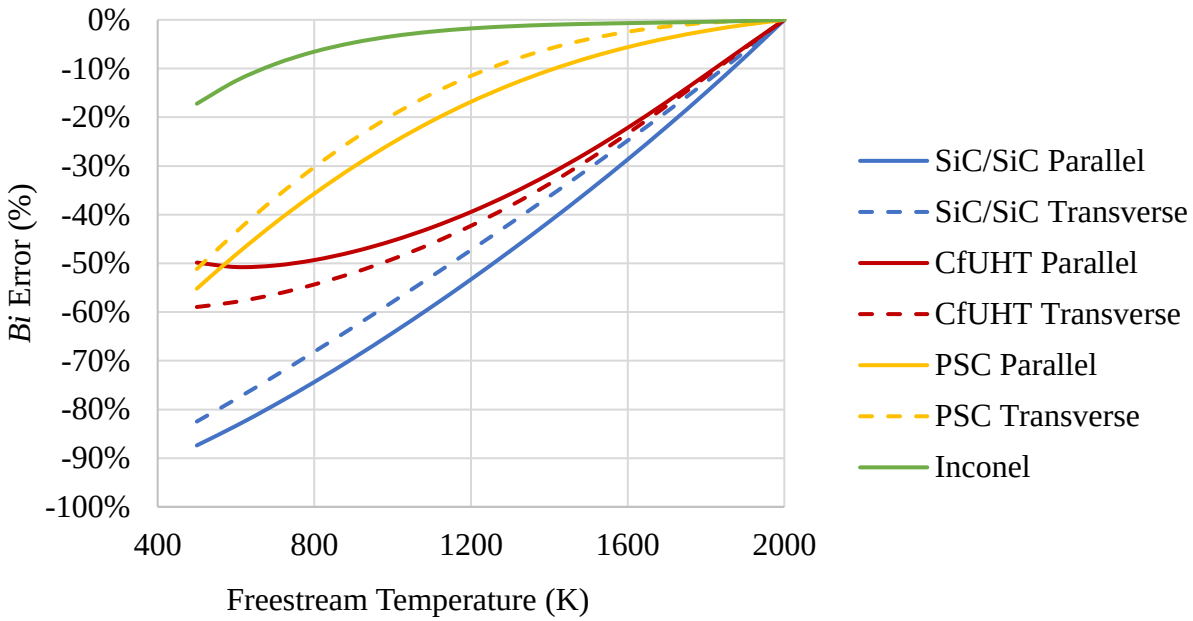

Figure 66: Comparison of Biot number error for all materials discussed, $\bar{\phi} = 0.6$

5.2. Film Cooled Flat Plate CFD

To show the effect of the Biot number mismatch, CFD simulations were performed using the film cooled flat plate discussed in detail in Chapter 3. Three different materials are compared: Inconel 718, the SiC/SiC CMC, and the C_f-UHTCMC. The PSC was not modeled because it has a similar *Bi* error as the C_f-UHTCMC at low temperatures. Each material was used in a fully conjugate heat transfer model at two different conditions, lab and engine, as described in Table 4.

The solid material and air thermal conductivities are all temperature-dependent (and thus spatially dependent) in the present work. Solid material properties were incorporated into Fluent using polynomial fits (shown in Figure 67). For anisotropic materials, the conductivities were input using the orthotropic material setting. A standard 0/90 2D weave orientation was assumed

with parallel conductivity along the streamwise length (x) and width (z) of the flat plate. The transverse conductivity was used for the through-thickness (y) conductivity.

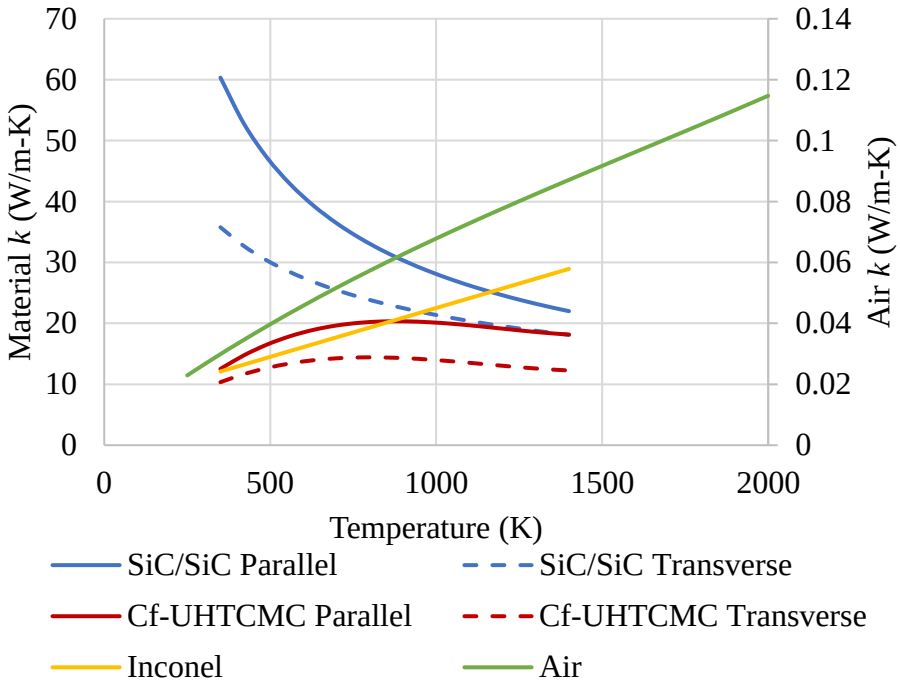

Figure 67: Temperature-dependent *k* for the flat plate model

Table 5 lists the air properties for the lab and engine conditions. In both cases, $T_\infty/T_c = 2$, but at engine conditions, $T_\infty = 2000$ K and at lab conditions, $T_\infty = 500$ K. The overall pressure ratio is 40 at engine condition. Air density was modeled using ideal gas assumptions. The freestream flow rate was adjusted to keep the freestream Reynolds number constant. The coolant flow rate was set to *ACR*=0.5 for both conditions.

Table 5: Flow Properties

	ρ_c kg/m^3	$c_{p,c}$ J/(kg K)	k_c W/(m K)	μ_c kg/(m s)	$Re_{d,c}$	Pr_c	ρ_∞ kg/m^3	$c_{p,\infty}$ J/(kg K)	k_∞ W/(m K)	μ_∞ kg/(m s)	$Re_{d,\infty}$	Pr_∞
Lab	1.41	1006	0.0226	1.60×10^{-5}	4325	0.71	0.71	1030	0.0399	2.71×10^{-5}	5000	0.70
Engine	13.9	1145	0.0680	4.35×10^{-5}	4282	0.73	7.01	1251	0.1146	6.82×10^{-5}	5000	0.74

5.2.1. Adiabatic Effectiveness

Among the parameters identified in Eq. (2.17), adiabatic effectiveness must be matched to match ϕ. For this reason, the two conditions are compared in terms of the adiabatic effectiveness, η. η distributions were determined by setting the thermal conductivity of the model to k = 0 W/m-K. Figure 68 shows the adiabatic effectiveness contours for both cases with the freestream flowing from left to right. Even though matching ACR captures some effect of both density ratio and specific heat ratio differences between the engine and experimental conditions, it does not account for viscosity and thermal conductivity differences in the gases which do have some effect on adiabatic effectiveness (c.f. Refs. 14 and 66).

The difference between the two conditions is shown in the $\Delta\eta$ contour at the bottom of Figure 68. The η distributions differ by, at most, 0.08 and only in a small region in the vicinity of the hole centerlines. Using the simple one-dimensional model of Eq. (2.17) with Bi = 0.5, χ = 0.9, and $\frac{h}{h_i}$ = 1.7 previously discussed, a 0.08 difference in η gives rise to a 0.05 difference in ϕ. However, the large gradient in η in the lateral direction in the contour plots would be expected to give rise to large multidimensional conduction within a conducting plate that would tend to compensate for the effect of a localized mismatch in η. Nevertheless, differences in ϕ due to fluid property differences between the engine and experimental conditions remain an area of interest and are addressed next and separate from those differences in ϕ attributable to Biot number differences.

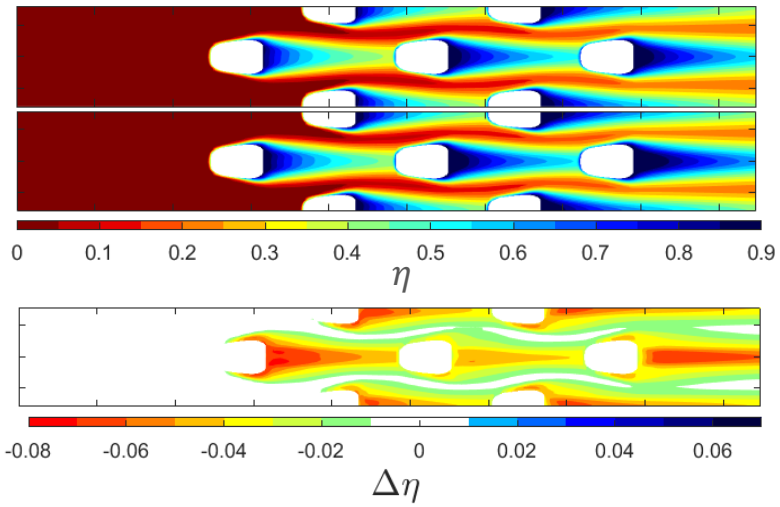

Figure 68: Contours for (top) η_{lab}, (middle) η_{engine}, and (bottom) $\Delta\eta$ $(\eta_{lab} - \eta_{engine})$

5.2.2. Isolating the Effect of Biot Number Mismatch

Despite the present focus on the Biot number, particularly that of complex anisotropic materials such as CMCs, the intricacies of the heat transfer coefficient's dependence on fluid properties means it is impossible to accept a priori that $\frac{h}{h_i}$ or χ are necessarily matched. Likewise, η is not always perfectly matched, even with matched *ACR* as previously shown. As such, differences in ϕ between engine and experimental conditions could be due to a combination of mismatches in both the Biot number and what can simply be called: fluidic effects. Therefore,

$$\Delta\phi_{Bi\,\&\,fluidic} = \phi_{Lab} - \phi_{Engine} \tag{5.3}$$

A novel technique was used to isolate the effects of mismatched *Bi* from those of the fluidic effects. With CFD, it is possible to set the thermal conductivity of a material to any value, however unrealistic. Therefore, an "ideal lab" material was conceived with a temperature-dependent thermal conductivity such that *Bi* number at any experimental conditions would match that of the real material at engine conditions (given the assumption of ϕ = 0.6). Any differences

in ϕ between the laboratory and engine conditions would then be attributable solely to fluidic effects that could cause mismatches in χ and $\frac{h}{h_i}$ between the two conditions.

$$\Delta\phi_{fluidic} = \phi_{Ideal\ Lab\ Mat,Lab\ T} - \phi_{Ideal\ Lab\ Mat,Engine\ T} \quad (5.4)$$

Of course, the ideal lab material must have a thermal conductivity that varies appropriately with temperature and its thermal conductivity must match that of the real material at engine conditions:

$$\phi_{Ideal\ Lab\ Mat,Engine\ T} = \phi_{Real\ Mat,Engine\ T} \quad (5.5)$$

With the fluidic effects on ϕ isolated, it is next possible to determine the contribution of the Biot number mismatch on the error in ϕ when an experiment is performed on the real material at laboratory conditions:

$$\Delta\phi_{Bi} = \phi_{Real\ Mat,Lab\ T} - \phi_{Ideal\ Lab\ Mat,Lab\ T} \quad (5.6)$$

5.2.3. Inconel 718

Inconel is used to demonstrate this technique first, then it is applied to composite materials. Figure 69 shows a comparison of *k* for Inconel, air, and the notional ideal lab material. The Inconel and ideal lab material thermal conductivities are matched at engine conditions, per the material definition. But the thermal conductivities are also very close over the range of temperatures shown, due to Inconel's similar Biot number.

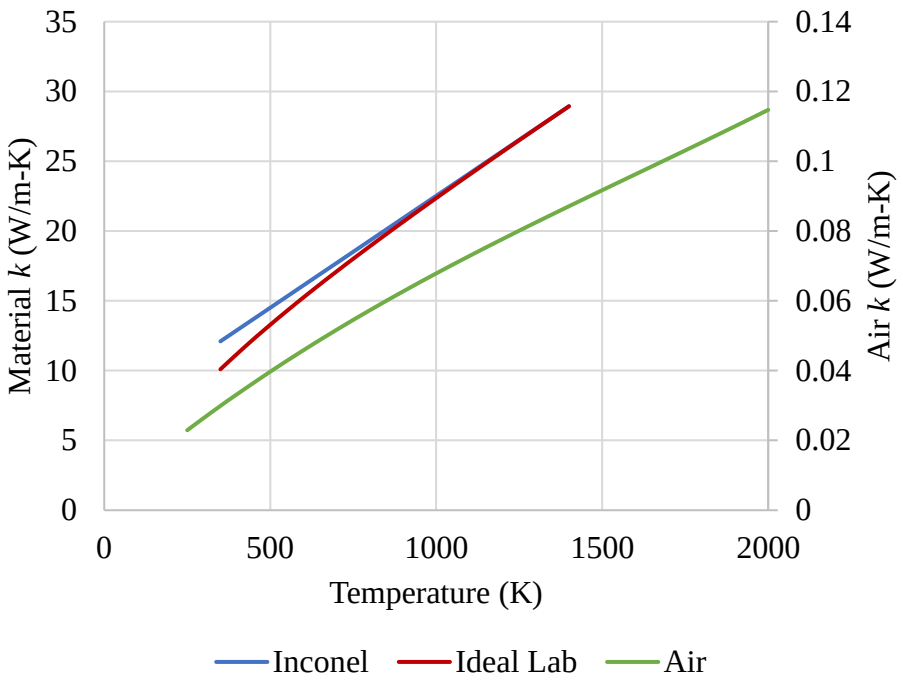

Figure 69: Thermal conductivities of Inconel, a notional ideal lab material with matched *Bi*, and air

These thermal conductivities were next applied to the computational model at both the 2000 K freestream engine condition and the 500 K freestream experimental condition. Figure 70 shows the resulting ϕ distributions. As previously discussed, the predicted Biot number error at the lab condition with $\bar{\phi} = 0.6$ is -17%. A lower than desired Biot number would contribute to an over prediction of ϕ; however, the low temperature experimental condition instead yields a ϕ distribution that is *lower* than at engine conditions. To further investigate the differences, $\Delta\phi$ plots were generated as shown in Figure 71. The differences in the ϕ distributions are shown in the top plot in Figure 71. As expected from the ϕ plots, the negative value in the $\Delta\phi_{Bi\ \&\ fluidic}$ plot shows that the lab condition is warmer than the engine condition, and therefore slightly under predicts the cooling effectiveness at the engine condition. The hypothetical ideal lab material offers little improvement over actual Inconel at the lab conditions, indicating that the

differences in ϕ between Inconel at lab and engine conditions is not dominated by Biot number effects. Indeed, the differences in ϕ due to the Biot number effects are shown to be less than 0.025 in Figure 71. Therefore, the differences in ϕ at lab conditions of up to 0.1 lower than at engine conditions are mostly due to fluidic effects (χ, $\frac{h}{h_i}$ and η mismatches), rather than Inconel's Biot number mismatch at lab conditions.

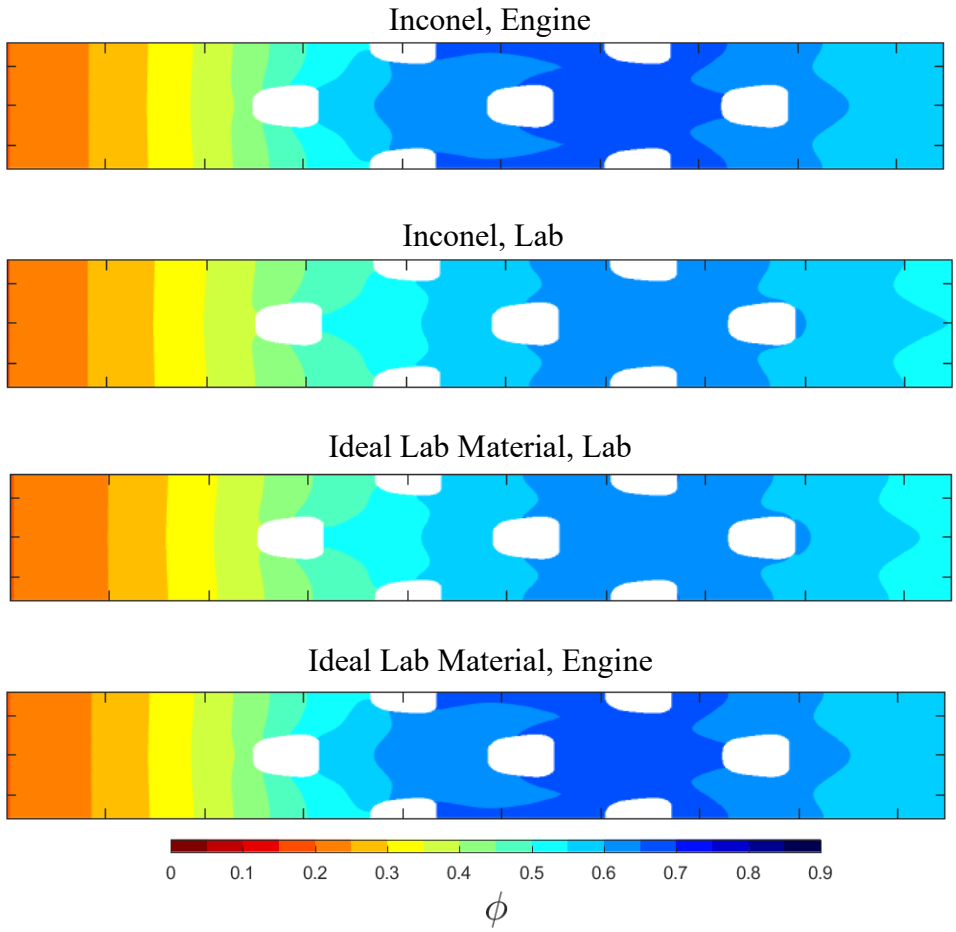

Figure 70: ϕ contours for Inconel and a notional ideal lab material with matched *Bi* at lab and engine conditions

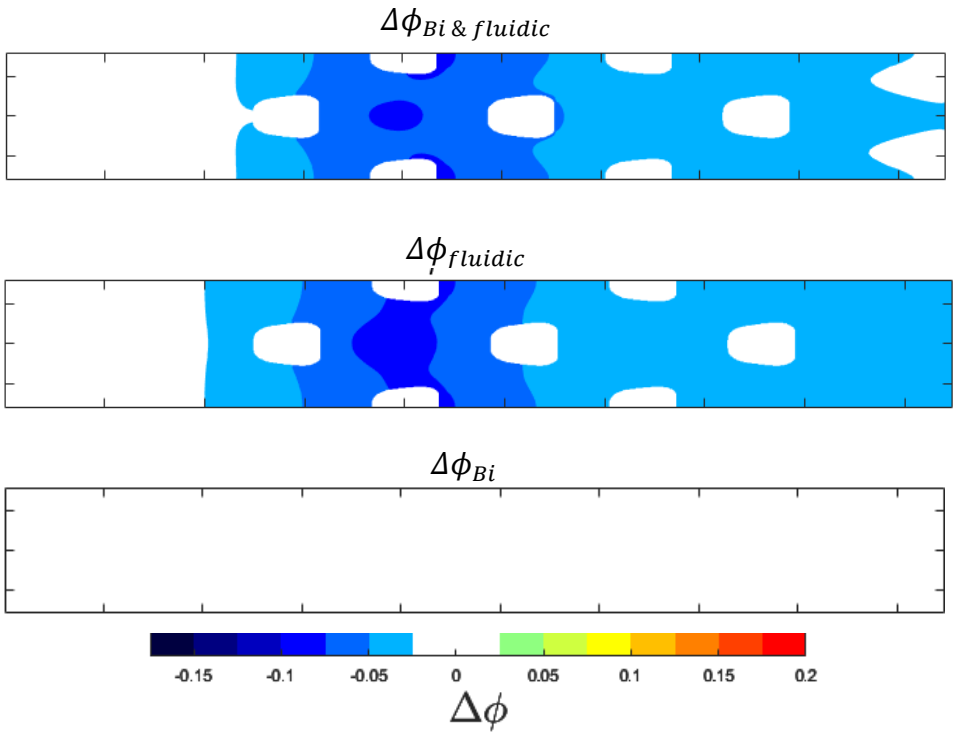

Figure 71: $\Delta\phi$ contours show the effects of Biot number and fluidic mismatches using Inconel at a lab condition

The difference between the two conditions is next investigated by examining the validity of the ϕ = 0.6 assumption that went into the definition of the ideal lab material. This is done by examining the ratio of thermal conductivities between the two materials. The thermal conductivity of the freestream air decreases by a factor of 2.9 from engine to lab conditions whereas the thermal conductivity of Inconel decreases by a factor of 2.4. Figure 72 shows that the *k* ratio distribution at the surface for the Inconel model is lower than desired. Of course, the *k* ratio is also not uniform owing to the non-uniform temperature distribution. The ideal lab material comes closer to the desired *k* ratio of 2.9, but naturally, that is only in the vicinity of where ϕ = 0.6.

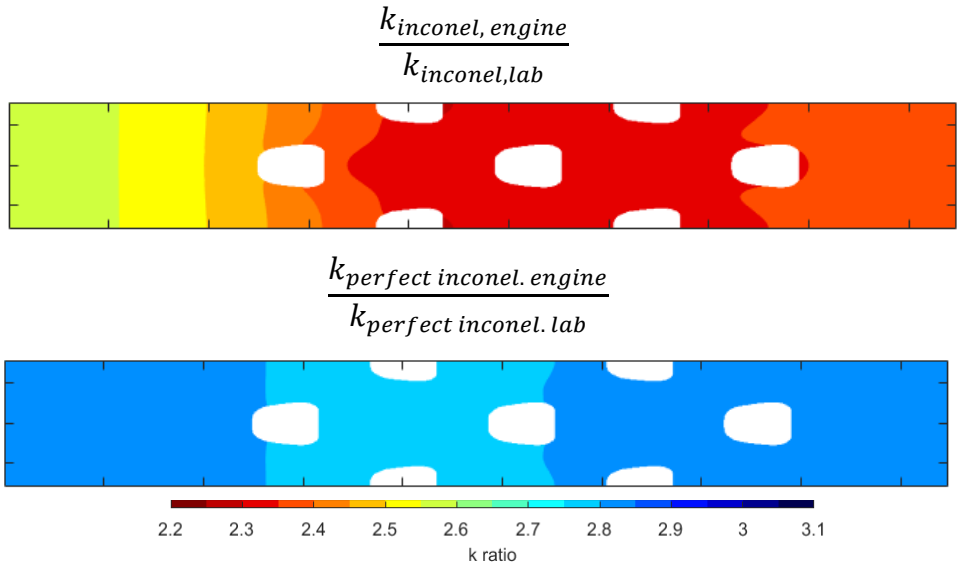

Figure 72: Thermal conductivity ratio contours for Inconel and a notional ideal lab material with matched *Bi*

With the $\Delta\phi_{Bi}$ of less than 0.025 in Figure 71, a 17% error in Biot number is quite likely acceptable to the experimentalist, provided that the fluidic effects are either mitigated or tolerated. Only by happenstance is it possible to test such a metallic turbine component at low temperature conditions and measure a ϕ distribution that is only minimally corrupted by a small Biot number mismatch, although it may well be corrupted due to other fluidic effects. While the turbine heat transfer community is accustomed to the serendipitous variation of metal thermal conductivity that makes such low temperature testing common, larger Biot number errors are predicted for composite materials.

5.2.4. SiC/SiC CMC

The next material investigated is the SiC/SiC CMC previously discussed. Figure 73 shows the thermal conductivities of the SiC/SiC, the ideal lab material, and air. Note that the SiC/SiC has two thermal conductivities—one each in the parallel and transverse directions. As such, the ideal lab material also requires anisotropy with two thermal conductivities. SiC/SiC has far higher thermal conductivities at low temperature, experimental conditions than at engine

conditions, which result in a predicted *Bi* error of -87% in the parallel direction and -82% in the transverse direction. Such a low Biot number would tend to contribute to an erroneously high ϕ measurement in the lab since ϕ increases with decreasing *Bi*. This would further reduce the surface temperature, exacerbating the Biot number mismatch.

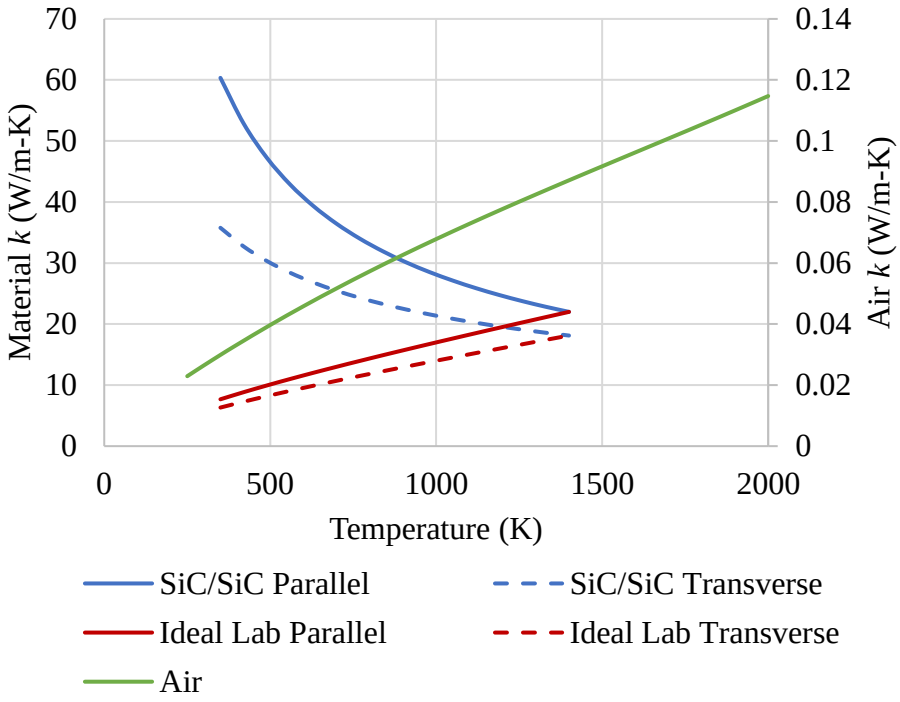

Figure 73: Thermal conductivities of the SiC/SiC CMC, a notional ideal lab material with matched *Bi*, and air

The ϕ plots for the SiC/SiC CMC material properties are shown in Figure 74 and the corresponding $\Delta\phi$ contours are shown in Figure 75. With the real material, the lab condition has a much higher ϕ, especially on the upstream edge compared to the engine condition. Ref. [27] showed this area is primarily affected by internal cooling in the plenum. The ideal lab material, however, gives a ϕ distribution at lab conditions much more like the real material at engine conditions, indicating that the Biot number mismatch is the primary reason that the real material is a poor choice for predicting ϕ at lab conditions. Nevertheless, the ideal lab material does yield

slightly different ϕ distributions at lab and engine conditions (most evident in Figure 75) due to some fluidic effects that cause mismatches in χ, η and $\frac{h}{h_i}$. It is no surprise that the fluidic effects are nearly identical to the Inconel case because they are dominated by the gas temperature differences which are the same here as they were with Inconel. The differences are not identical because the different thermal conductivity of the material affects the material temperature, and through convection, the freestream fluid. As predicted, the Biot number mismatch does cause an increased ϕ on the leading edge due to increased internal cooling. Because this area has no film cooling, the increase is due entirely to the mismatched Biot number. Therefore, this effect is expected regardless of the cooling hole arrangement. There is also an area of decreased cooling downstream of the cooling holes. This is a secondary effect of increased internal cooling. As discussed in Ref. [27], increased cooling on the upstream edge means more heat is transferred to the coolant as it travels through the coolant holes and forms the film on the downstream surface. Thus, the film coolant is warmer and less effective.

5.2.5. C_f-UHTCMC

The final material is the C_f-UHTCMC. Figure 76 shows the thermal conductivities for both the real and ideal lab materials as well as air. The predicted *Bi* error at laboratory condition is -50% in the parallel direction and -59% in the transverse direction, about halfway between the Inconel and SiC/SiC values. The $\Delta\phi$ plots are shown in Figure 77. The difference in ϕ between engine and lab conditions due to fluidic effects is again roughly the same as that obtained with the previously discussed materials due to identical inlet temperatures. The differences in material thermal conductivity mean that they will not be identical in this fully conjugate model. The error in ϕ introduced by the Biot number mismatch is not as extreme as with SiC/SiC, but more than that with Inconel. Interestingly, the upstream region where $\Delta\phi > 0$ might somewhat offset the

region farther downstream where $\Delta\phi < 0$ in an area averaged sense. Of course, how much offsetting occurs would be highly geometry dependent but could fortuitously help an experimentalist at least obtain slightly more correct area-averaged overall effectiveness values despite some significant errors in the spatially resolved values.

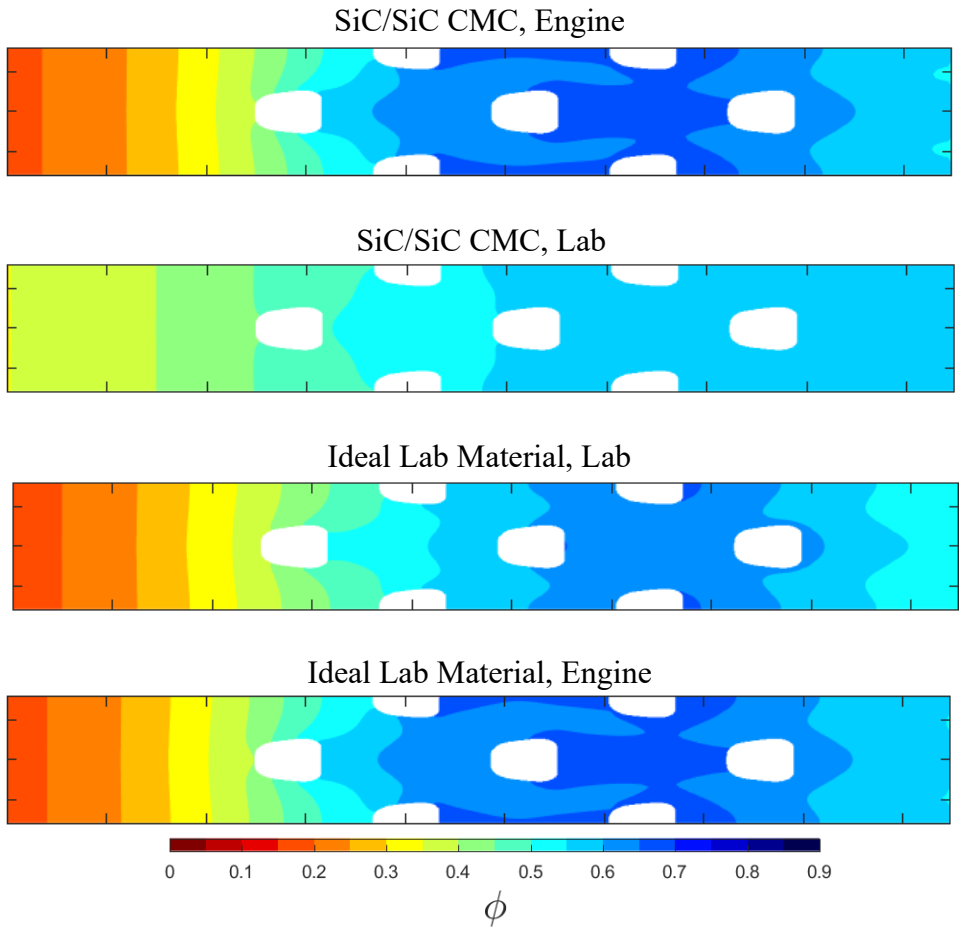

Figure 74: ϕ contours for a SiC/SiC CMC and a notional ideal lab material with matched *Bi* at lab and engine conditions

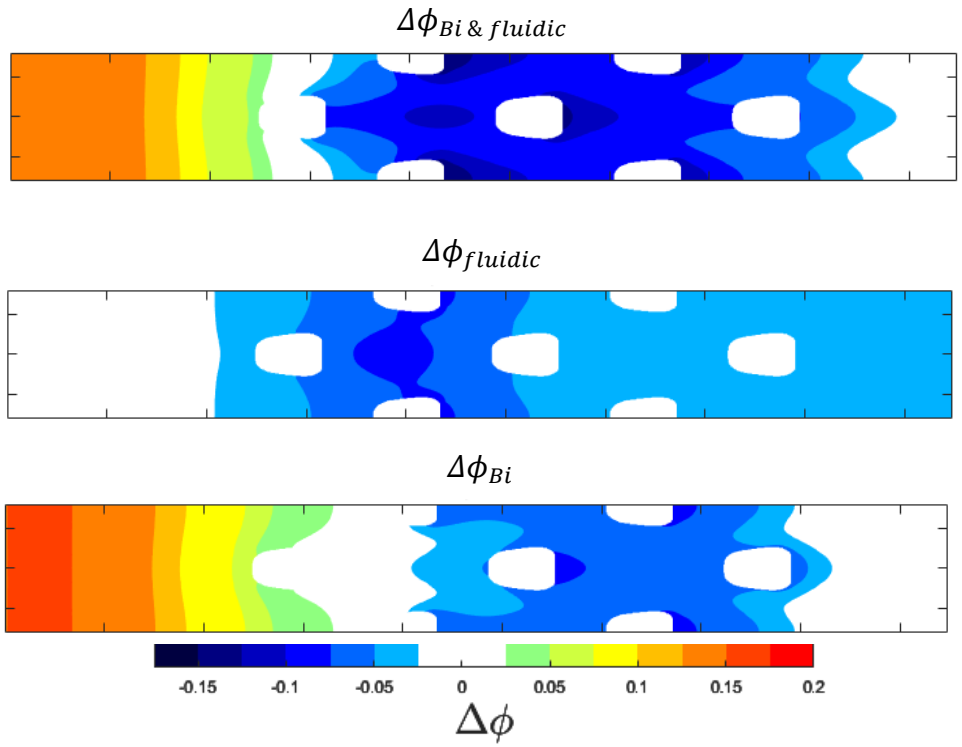

Figure 75: $\Delta\phi$ contours show the effects of Biot number and fluidic mismatches using a SiC/SiC CMC at a lab condition

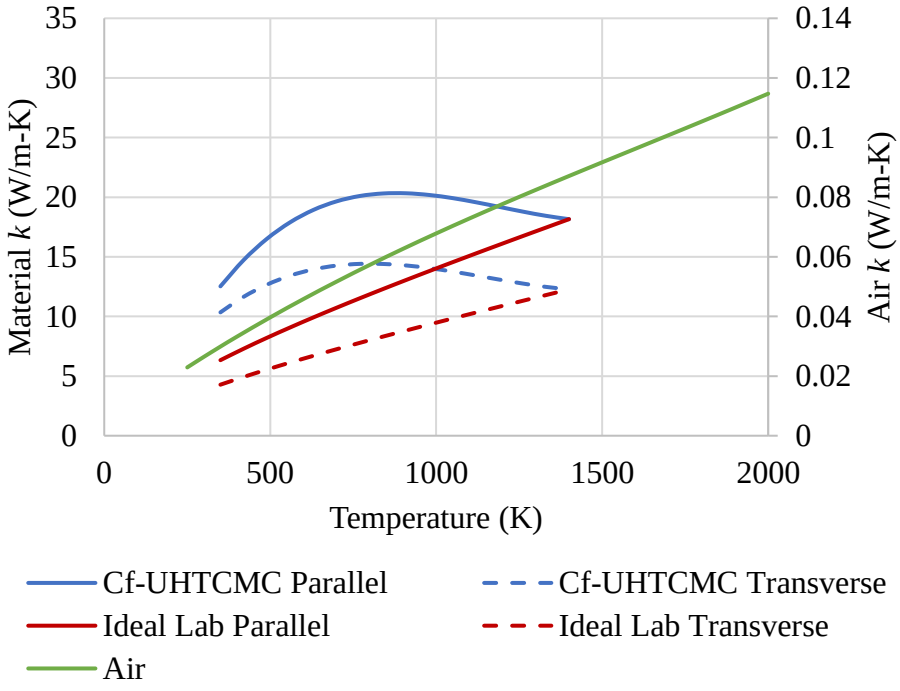

Figure 76: Thermal conductivities of a C_f-UHTCMC, a notional ideal lab material with matched *Bi*, and air

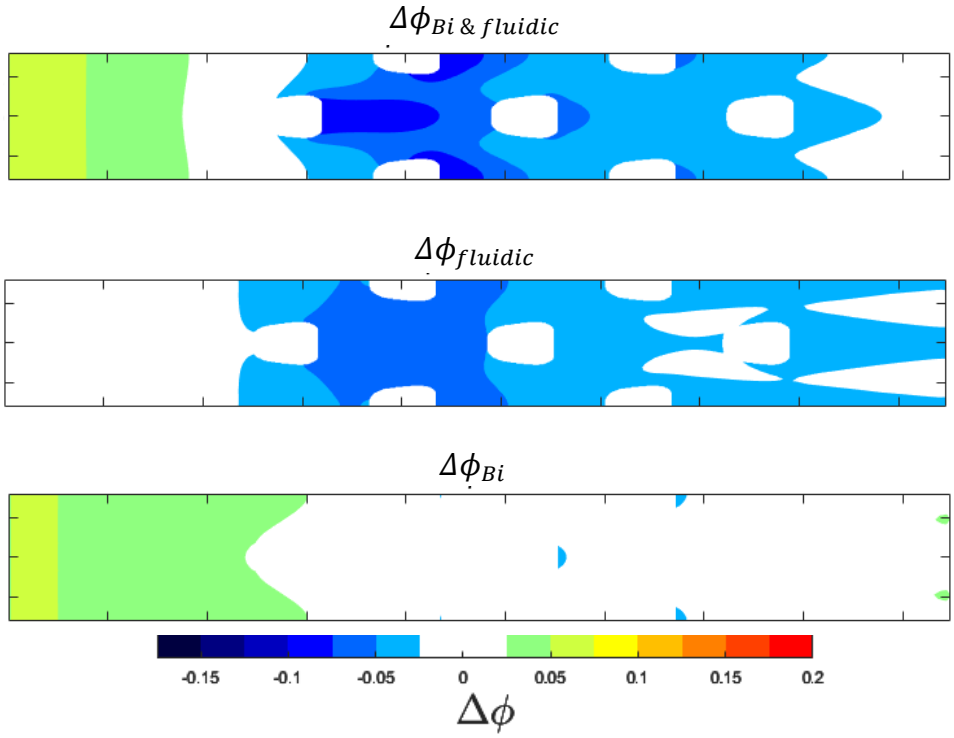

Figure 77: $\Delta\phi$ contours show the effects of Biot number and fluidic mismatches using a C_f-UHTCMC at a lab condition

5.3. Summary

In summary, this chapter showed that the ratio of material thermal conductivities must be matched to the freestream fluid thermal conductivity to scale the Biot number. This is regardless of whether the material is isotropic or anisotropic. Additionally, simulations using a SiC/SiC composite showed that the thermal conductivity ratio is not matched, so low temperature experiments on a SiC/SiC component could contribute to a misleading overall effectiveness result. This chapter made a significant step towards answering Objective 3. Recall that this objective is to scale overall effectiveness for both isotropic and anisotropic materials. Scaling the Biot number presents a unique challenge with anisotropic material, as this chapter thoroughly discussed. An experimentalist should use a material with thermal conductivity matched to the

ideal lab material to scale either anisotropic or isotropic materials. The next chapter will continue to progress towards answering Objective 3.

6. Scaling Internal Cooling

Chapter 5 showed the effects of Biot number and fluidic mismatches on scaling ϕ. This chapter will pivot to address the fluidic effects on overall effectiveness. Multiple components comprise the umbrella term of fluidic effects. One of them is adiabatic effectiveness, which has been addressed in previous scaling literature, as discussed in Chapter 2. The density ratio and more recently, the specific heat ratio, have been shown to play important roles in scaling adiabatic effectiveness. Another component is the heat transfer on the internal surfaces. Specifically, the ratio of the internal and external heat transfer coefficient must be matched. However, this chapter demonstrates the requirements for the coolant and freestream flow conditions to conduct an appropriately scaled overall effectiveness experiment. Since the viscosity and thermal conductivity of the fluids (in addition to density and specific heat) play significant roles that influence heat transfer coefficient behavior, this gives rise to an additional nondimensional parameter that should, in theory, be matched to properly execute an overall effectiveness experiment. This chapter will also help answer Objective 3 because scaling internal cooling is a key to scaling overall effectiveness.

6.1. Analysis

First, an analysis is conducted to determine the parameters important to match the heat transfer coefficient ratio. Because the Stanton number is dependent on the geometry and a function of the Reynolds number and Prandtl number, the external Stanton number distribution is:

$$St = \frac{h}{\rho_\infty u_\infty c_{p,\infty}} = f_1(Re_\infty, Pr_\infty) \tag{6.1}$$

where

$$f_1(Re_\infty, Pr_\infty) = C_1 Re_\infty^m Pr_\infty^n \tag{6.2}$$

The constant C_1, as well as the exponents on the Reynolds number and Prandtl number, are functions of the geometry and whether the flow is laminar or turbulent. Similarly, the internal St distribution may be written:

$$St_i = \frac{h_i}{\rho_c u_c c_{p,c}} = f_2(Re_c, Pr_c) \tag{6.3}$$

where

$$f_2(Re_c, Pr_c) = C_2 Re_c^p Pr_c^q \tag{6.4}$$

Therefore, the h ratio applicable to Eq. (2.17) may be written:

$$\frac{h}{h_i} = \frac{\rho_\infty u_\infty c_{p,\infty} C_1 Re_\infty^m Pr_\infty^n}{\rho_c u_c c_{p,c} C_2 Re_c^p Pr_c^q} \tag{6.5}$$

With Eq. (2.17) requiring that $\frac{h}{h_i}$ is matched, the requirement is:

$$\left(\frac{h}{h_i}\right)_{exp} = \left(\frac{h}{h_i}\right)_{eng} \tag{6.6}$$

or

$$\left(\frac{\rho_\infty u_\infty c_{p,\infty} C_1 Re_\infty^m Pr_\infty^n}{\rho_c u_c c_{p,c} C_2 Re_c^p Pr_c^q}\right)_{exp} = \left(\frac{\rho_\infty u_\infty c_{p,\infty} C_1 Re_\infty^m Pr_\infty^n}{\rho_c u_c c_{p,c} C_2 Re_c^p Pr_c^q}\right)_{eng} \tag{6.7}$$

$$\left(\frac{\rho_\infty u_\infty c_{p,\infty} Re_\infty^m Pr_\infty^n}{\rho_c u_c c_{p,c} Re_c^p Pr_c^q}\right)_{exp} = \left(\frac{\rho_\infty u_\infty c_{p,\infty} Re_\infty^m Pr_\infty^n}{\rho_c u_c c_{p,c} Re_c^p Pr_c^q}\right)_{eng} \tag{6.8}$$

Next, the issue of the coolant flow rate and the multiple options for coolant flowrate scaling parameters that must be matched are discussed. Considering Ref. [16] which established that the advective capacity ratio (ACR) tends to be a highly effective means of scaling adiabatic effectiveness provided the film coolant is not separated from the surface, it is assumed that *ACR* is matched. Matching *ACR* implies

$$\left(\frac{\rho_\infty u_\infty c_{p,\infty}}{\rho_c u_c c_{p,c}}\right)_{exp} = \left(\frac{\rho_\infty u_\infty c_{p,\infty}}{\rho_c u_c c_{p,c}}\right)_{eng} \tag{6.9}$$

This ratio appears in Eq. (6.8) which is why casting the heat transfer coefficient in terms of the Stanton number beginning in Eq. (6.3) rather than the Nusselt number was a convenient choice earlier, although it should be noted that an equivalent result could have been accomplished using the Nusselt number. Employing Eq.(6.9), Eq. (6.8) becomes:

$$\left(\frac{Re_\infty^m Pr_\infty^n}{Re_c^p Pr_c^q}\right)_{exp} = \left(\frac{Re_\infty^m Pr_\infty^n}{Re_c^p Pr_c^q}\right)_{eng} \tag{6.10}$$

Further, matching the external flow field requires matching Re_∞, which is almost always the case in experimental film cooling work. However, the same cannot be said of Re_c, which generally cannot be matched to engine conditions if any of the more typical coolant flow rate parameters (M, I, VR, or ACR) are matched to engine conditions instead. Indeed, only very few studies (cf. Refs. 67 and 14) have considered matching coolant Reynolds number as an alternative, but they have shown that η is not matched well in such cases. The resulting requirement to match $\frac{h}{h_i}$ may therefore be written:

$$\left(\frac{Pr_\infty^n}{Re_c^p Pr_c^q}\right)_{exp} = \left(\frac{Pr_\infty^n}{Re_c^p Pr_c^q}\right)_{eng} \tag{6.11}$$

Most film cooling experiments are performed with air freestream, whose Prandtl number is at most a weak function of temperature. If the Prandtl number of the freestream gas is the same at both engine and experimental conditions, a simplified version of the requirement would be

$$\left(Re_c^p Pr_c^q\right)_{exp} = \left(Re_c^p Pr_c^q\right)_{eng} \tag{6.12}$$

In many experimental situations that employ air as the coolant, the Pr_c may be approximated as matched. This would then lead to the unfortunate requirement that Re_c would need to be matched while simultaneously matching *ACR*, upon which the result of Eq. (6.9) is predicated. Avoidance of that requirement would require the use of a foreign coolant gas whose Prandtl number differs

from that of the engine coolant air in such a way as to compensate for a mismatch in the Re_c. Of course, this would require knowledge of the exponent: p and q, thereby creating even additional complexity. Setting aside the complexity of simultaneously matching what this theory suggests are the relevant nondimensional parameters, next the validity of the underlying theory developed is examined.

6.2. Internal Cooling Model

To investigate this theory, a simple conjugate heat transfer simulation was performed with computational fluid dynamics. The model is of a conducting wall with parallel flows in the same direction on each side of the wall. As shown in Figure 78, hot air flows over the top and cold gas flows underneath, creating a conjugate model analogous to an internally cooled turbine component. All the boundaries were non-slip walls. Several gases with a wide range of properties were selected to determine how well Eq. (6.11) accounts for those property variations in scaling the heat transfer coefficient ratio. The properties were set to be constant to ensure they are invariant with temperature changes due to conduction and convection. For instance, helium has a high heat capacity: five times as much as air and ten times as much as argon. Helium also has higher thermal conductivity: more than six times as much as air and nearly ten times as much as argon. The selected gases, shown in Table 6, have been used in prior experimental work, such as Ref. 16, to study how η scales.

Table 6: Selected gas properties

Gas	$\rho\ \left(\frac{\mathrm{kg}}{\mathrm{m^3}}\right)$	$c_p\ \left(\frac{\mathrm{J}}{\mathrm{kg\cdot K}}\right)$	$k\ \left(\frac{\mathrm{W}}{\mathrm{m\cdot K}}\right)$	$\mu\ \left(\frac{\mathrm{kg}}{\mathrm{m\cdot s}}\right)$
Air	1.2250	1006.4	0.0242	1.79×10^{-5}
Argon	1.6228	520.6	0.0158	2.13×10^{-5}
CO_2	1.7878	848.8	0.0145	1.37×10^{-5}
Helium	0.1625	5193.0	0.1520	1.99×10^{-5}

The geometry and fluid inlet temperatures are identical for all the cases. The only changes are to fluid velocity and fluid properties. The model is simple due to the complex nature of this problem. By eliminating film cooling and fluid mixing, the only parameters remaining in Eq. (2.17) are the Biot number and the ratio of heat transfer coefficients. Any changes in the nondimensional surface temperature between different coolants are due to changes in *Bi* and *h* only. The conductivity of the solid material is set to 0.1 W/m-K, selected not to match any Biot number, but rather to accentuate differences in the manner that gas selection impacts the temperature distribution within the solid material. The height of both the freestream and coolant channels is identical, h = 0.635 cm, as shown in Figure 78. The channels extend 48h.

Each simulation used air as the fluid along the top; this is a proxy for what is labeled the freestream (FS) gas. Simulations were initiated by setting both the freestream and coolant inlet to uniform velocity and temperature profiles. The freestream was set to 320 K and the coolant to 300 K like what is used in typical laboratory experiments, such as Ref. [55]. Both inlets were set at one atmosphere of pressure. The simulations were run in ANSYS Fluent using its laminar flow solver for the simple flow field with only a warm freestream and internal cooling.

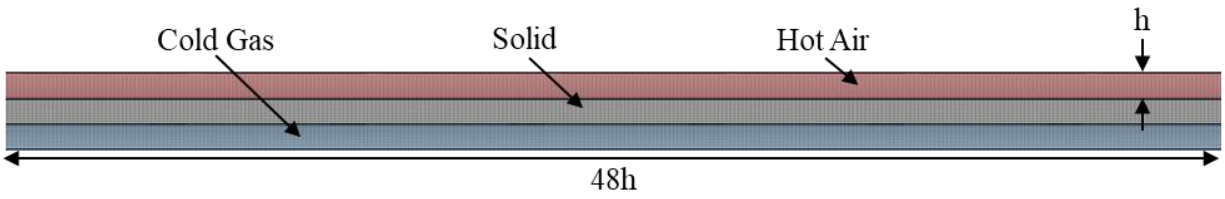

Figure 78: Mesh close-up and zone descriptions of internal cooling geometry

Table 7 lists the sets of simulations to be discussed. Each set of simulations involves multiple cases for which gas properties are varied and within each set, the parameters or properties marked with a check mark identify those that are matched in each of the simulations in the set. Only the first four sets use the internal cooling (IC) geometry. Set 5 adds film cooling (FC),

whose geometry is described later. The table lists all the parameters necessary to match Eq. (6.9): Pr_∞, Pr_c, and Re_c. It was assumed in the development of this ratio that *ACR* and Re_∞ are matched. Finally, because this geometry is also sensitive to *Bi*, the solid material thermal conductivity, k_s, is also listed. Each set of simulations is discussed in detail in the following sections. In every set, there is a case where air is both the coolant and the freestream; that is the baseline to which the other cases are compared.

Table 7: List of sets with properties matched in each case

Set	*ACR*	Re_∞	Pr_∞	Re_c	Pr_c	k_s	*Geometry*
1	✓	✓	✓			✓	IC
2a	✓	✓	✓	✓	✓	✓	IC
2b	✓	✓	✓	✓	✓	✓	IC
3	✓	✓	✓	✓	✓		IC
4	✓	✓	✓	✓	✓	✓	IC
5	✓	✓	✓	✓	✓	✓	FC

6.2.1. Set 1: Internal Cooling Temperature Distribution with Matched ACR

The resulting temperature distributions on the upper and lower surfaces of the solid material were extracted and nondimensionalized using

$$\theta = \frac{T_\infty - T}{T_\infty - T_c} \tag{6.13}$$

This set of cases matches *ACR* and Pr_∞ only. As discussed with Eq. (6.9), adiabatic effectiveness is effectively scaled using *ACR* when I is less than approximately 0.7 and it would therefore be convenient if *ACR* also scaled the internal heat transfer coefficient appropriately. Pr_∞ is matched in all the cases within Set 1 because air is used as the freestream gas for all four tests. The four test runs in this set are shown in Table 8. The coolants are air, argon (Ar), carbon dioxide (CO_2),

and helium (He). The freestream flow rate is constant between each gas. The coolant flow rate is varied to match *ACR* across the various densities and specific heats of the coolant gases.

Table 8: Properties of cases with matched ACR (Set 1)

Coolant	Re_c	Pr_c	***FS***	Re_∞	Pr_∞	***DR***	***VR***	***M***	***I***	***ACR***
Air	5000	0.74	Air	**5000**	**0.74**	1.00	1.00	1.00	1.00	**1**
Ar	8139	0.70	Air	**5000**	**0.74**	1.32	1.46	1.93	2.82	**1**
CO_2	7744	0.80	Air	**5000**	**0.74**	1.46	0.81	1.19	0.96	**1**
He	871	0.68	Air	**5000**	**0.74**	0.13	1.46	0.97	1.01	**1**

The nondimensional temperature distributions are plotted for the upper and lower surfaces in Figure 79. Because the freestream gas is identical for all four cases, the temperature distribution on the upper surface is impacted less than the lower surface where the coolant gas is varied. The resulting θ distributions are widely varied which shows that *ACR* by itself does not scale h/h_i well. The relative order is most closely correlated to Re_c. This finding follows the theory previously discussed: Re_c must be included in the scaling parameter.

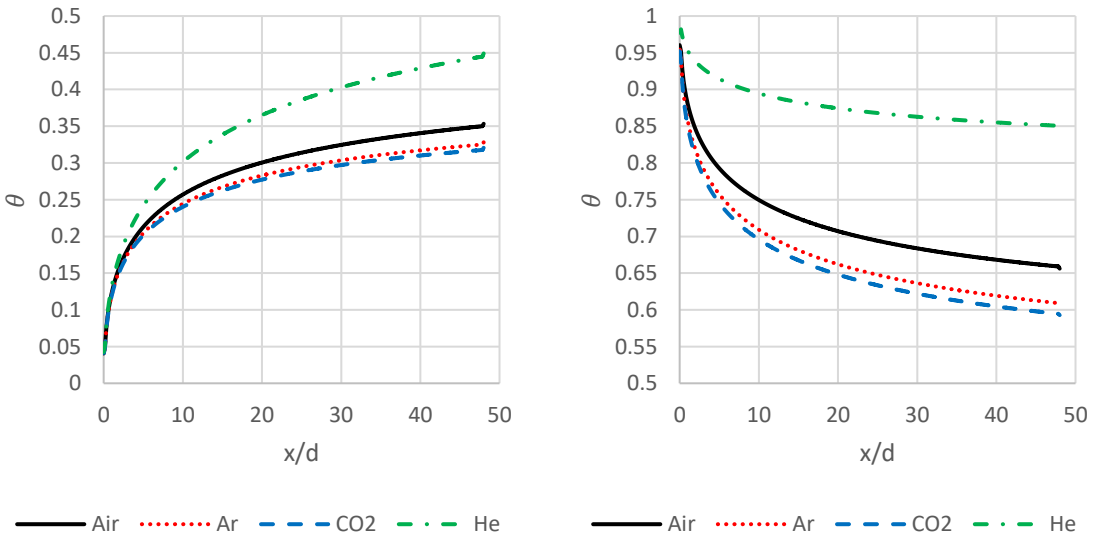

Figure 79: Internal cooling temperature distribution on the upper (left) and lower (right) surfaces with $ACR = 1$

6.2.2. Set 2: Internal Cooling Temperature Distribution with Matched ACR, Coolant Reynolds Number, and Coolant Prandtl Number

The fact that matching ACR alone does not give matched nondimensional surface temperature at least lends some credibility to the theory of Eq. (6.11), which suggests that Re_c and Pr_c, are also important to match h/h_i. In this section, those previous simulations are modified to also match Re_c and Pr_c, thus satisfying the requirement of Eq. (6.11). The method chosen is to match each parameter individually instead of the product because the exponents p and q are generally unknown (although they may be known for certain canonical geometries). Previously, to match ACR alone, it was only necessary to adjust the coolant velocity. Now with the additional requirement to match the coolant Reynolds number and coolant Prandtl number, there are two additional requirements to simultaneously satisfy.

A unique advantage of using CFD, rather than experiments, is the possibility of creating nonphysical, fictional gases. This has been done before (cf. Ref. [67]) and is used presently to test the scaling theory. With the coolant flowrate already set previously through the requirement to match ACR, the viscosity of the coolant gas is modified such that the coolant Reynolds number is matched to the case with air coolant. Finally, the coolant thermal conductivity is selected to match Pr_c to the case with air coolant. Table 9 lists the properties for this set of simulations (Set 2a). The asterisks indicate the gas has been modified. The values of k_c are identical to match Pr_c, not because k_c matching is required. There are other methods that will be discussed in the following sections that show scaling can be accomplished without the same k_c. The highlighted properties are changed from their nominal values to match the simulation with air as both the coolant and freestream gas. The θ distribution is shown in Figure 80. The θ

distributions collapse on top of each other on both surfaces, proving the ratio $\frac{Pr_\infty^n}{Re_c^p Pr_c^q}$ in Eq. (6.11) does scale the *h* ratio.

Table 9: Properties of cases with matched *ACR*, Re_c, and Pr_c by changing coolant μ and *k* as indicated by the highlighted values (Set 2a)

Coolant	$\mu\left(\frac{kg}{m\cdot s}\right)$	$k\left(\frac{W}{m\cdot K}\right)$	Re_c	Pr_c	*FS*	Re_∞	Pr_∞	*DR*	*VR*	*M*	*I*	*ACR*
Air	1.79x10^{-5}	0.0242	**5000**	**0.74**	Air	**5000**	**0.74**	1.00	1.00	1.00	1.00	**1**
*Ar**	3.46x10^{-5}	0.0242	**5000**	**0.74**	Air	**5000**	**0.74**	1.32	1.46	1.93	2.82	**1**
*CO_2**	2.12x10^{-5}	0.0242	**5000**	**0.74**	Air	**5000**	**0.74**	1.46	0.81	1.19	0.96	**1**
*He**	3.47x10^{-5}	0.0242	**5000**	**0.74**	Air	**5000**	**0.74**	0.13	1.46	0.19	0.28	**1**

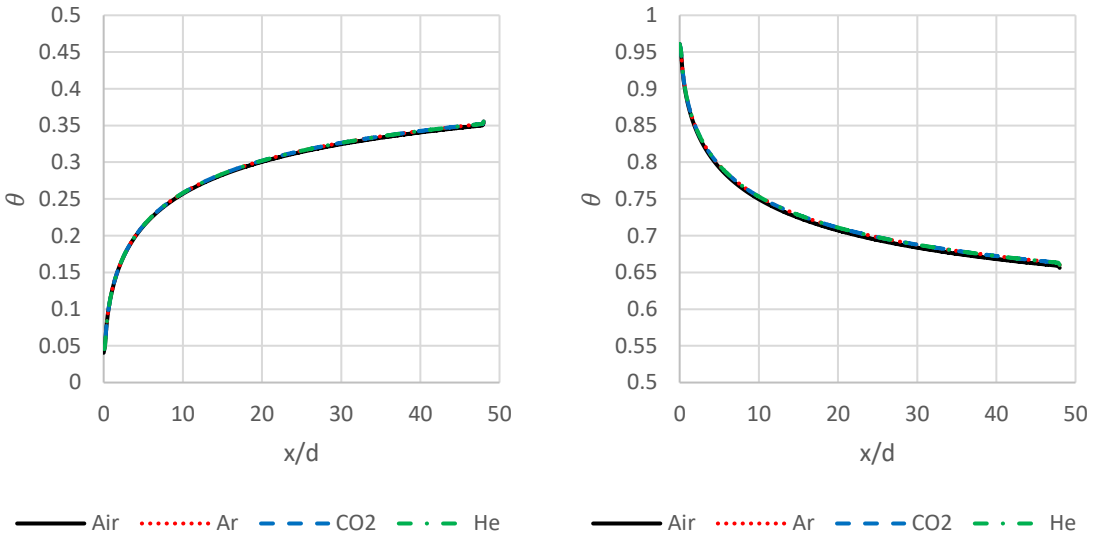

Figure 80: Internal cooling temperature distribution on the upper (left) and lower (right) surfaces with matched ACR, Re_c, and Pr_c by changing coolant *k* and μ (Set 2a)

To further test the robustness of the theory, an alternative technique to simultaneously match all relevant nondimensional parameters was accomplished. Whereas in Set 2a, the flow rate was set via ACR based on the real density and specific heat of the coolant gas, now the coolant flow rate is set to match Re_c based on the coolant real density and viscosity of the coolant gas. From that point, the coolant specific heat is modified to match ACR to that of the air case and finally,

the coolant thermal conductivity is adjusted to match Pr_c. Table 10 lists the properties for this set of simulations (Set 2b). The coolant velocity was set to match Re_c, the coolant specific heat was changed to match *ACR*, and the coolant thermal conductivity was changed to match Pr_c. Because air is used for each run, Pr_∞ is already matched. The θ distribution is shown in Fig 81. Again, the θ distributions collapse on top of each other on both surfaces, providing further credibility supporting the assertion that Eq. (6.12) is required to scale the *h* ratio, regardless of how Re_c and Pr_c are matched.

Table 10: Properties of cases with matched *ACR*, Re_c, and Pr_c by changing coolant *k* and c_p as indicated by the highlighted values (Set 2b)

Coolant	$c_{p,c}\left(\frac{J}{kg\cdot K}\right)$	$k_c\left(\frac{W}{m\cdot K}\right)$	Re_c	Pr_c	*FS*	Re_∞	Pr_∞	*DR*	*VR*	*M*	*I*	*ACR*
Air	1006.43	0.0242	**5000**	**0.74**	Air	**5000**	**0.74**	1.00	1.00	1.00	1.00	**1**
*Ar**	847.49	0.0242	**5000**	**0.74**	Air	**5000**	**0.74**	1.32	0.90	1.19	1.06	**1**
*CO_2**	1314.53	0.0242	**5000**	**0.74**	Air	**5000**	**0.74**	1.46	0.52	0.77	0.40	**1**
*He**	904.98	0.0242	**5000**	**0.74**	Air	**5000**	**0.74**	0.13	8.38	1.11	9.32	**1**

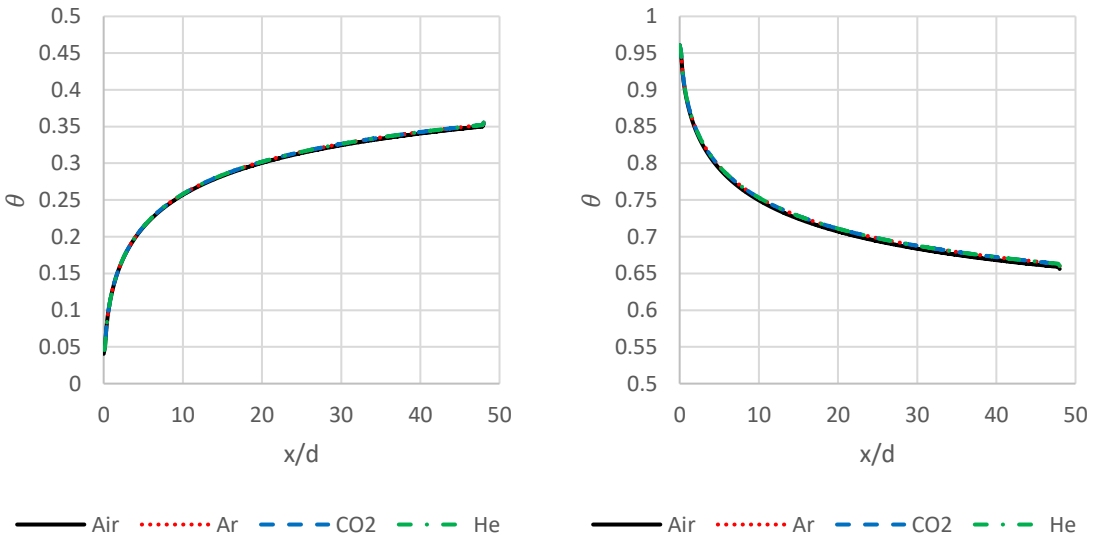

Figure 81: Internal cooling temperature distribution on the upper (left) and lower (right) surfaces with matched ACR, Re_c, and Pr_c by changing coolant *k* and c_p (Set 2b)

6.2.3. Set 3: Internal Cooling Temperature Distribution with Air as the Coolant

These results support the validity of Eq. (6.12) to match h/h_i when the freestream flow is fixed and thus Re_∞ and Pr_∞ were trivially matched. Next, the role of the freestream gas selection is examined in the context of Eq. (6.11) which means a conscious effort must be made to match Pr_∞. In the following simulations air is used on the coolant side of the wall and foreign gases are used on the freestream side. The coolant (now air) velocity is set to match Re_c, the coolant's specific heat is changed to match *ACR*, and the coolant's thermal conductivity is changed to set Pr_c. Because different gases are used as the freestream gas, Pr_∞ is no longer constant and so the thermal conductivity of the freestream gas is changed to match Pr_∞. The properties for each simulation are shown in Table 11, where the highlight indicates that the property has been changed to match a parameter. Note that this set of cases requires three fluid properties to be altered from their real values, whereas Sets 2a and 2b required only two properties to be altered.

The resulting θ distributions are shown in Figure 82. Although similar in principle to Set 2a, thereby satisfying Eq. (6.11) and ensuring h/h_i is matched, the θ distributions no longer match. This discrepant event is explained in the context of Eq. (2.26) and Chapter 5, which shows that the Biot number is sensitive to the thermal conductivity of the freestream gas. Whereas in Sets 2a and 2b k_∞ was held constant, now in Set 3, k_∞ varies while k_c is constant. The gravity of this seemingly innocuous distinction is rooted in the fact that although Nu_∞ remains constant throughout all these simulations. h and thus, h_i, differ only among the simulations in Set 3 since k_∞ varies in Set 3. With a varying h but a fixed solid thermal conductivity, k_s, the Biot number naturally differs among the simulations of Set 3.

Table 11: Properties of cases with matched *ACR*, Re_c, and Pr_c with air as the coolant (Set 3)

Coolant	$c_{p,c}\left(\frac{J}{kg\cdot K}\right)$	$k_c\ \left(\frac{W}{m\cdot K}\right)$	$Re\ c$	$Pr\ c$	*FS*	k_∞	Re_∞	Pr_∞	*DR*	*VR*	*M*	*I*	*ACR*
Air	1006.4	0.0242	**5000**	**0.74**	Air	0.0242	**5000**	**0.74**	1.00	1.00	1.00	1.00	**1**
*Air**	618.3	0.0149	**5000**	**0.74**	Ar*	0.0149	**5000**	**0.74**	0.75	1.12	0.84	0.94	**1**
*Air**	649.8	0.0156	**5000**	**0.74**	CO_2*	0.0156	**5000**	**0.74**	0.69	1.91	1.32	2.52	**1**
*Air**	5775.2	0.1389	**5000**	**0.74**	He*	0.1389	**5000**	**0.74**	7.54	0.12	0.90	0.11	**1**

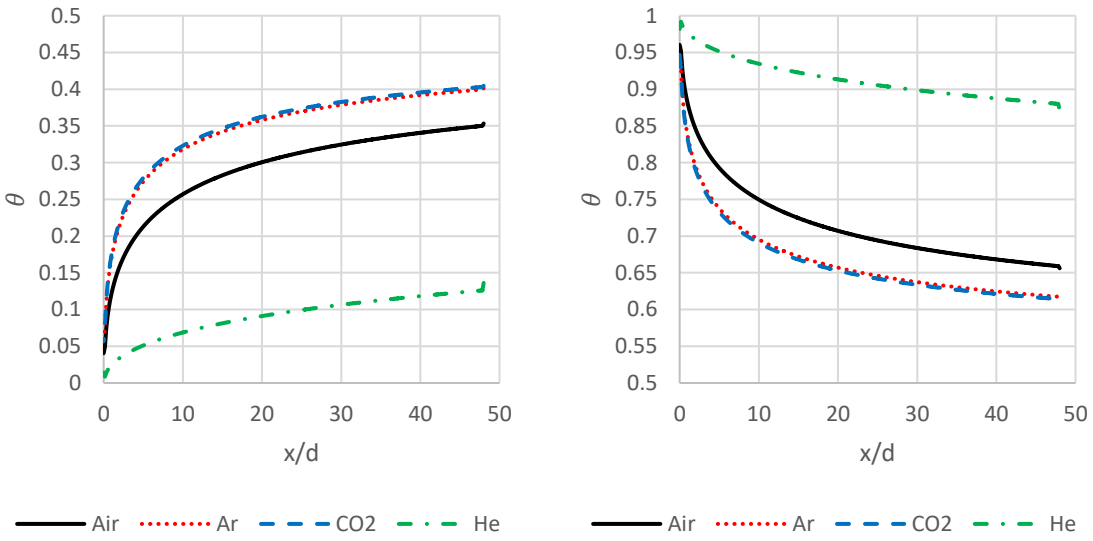

Figure 82: Internal cooling temperature distribution on the upper (left) and lower (right) surfaces with matched ACR, Re_c, and Pr_c with air as the coolant (Set 3)

6.2.4. Set 4: Internal Cooling Temperature Distribution with Air as the Coolant and Matched Biot Number

To demonstrate that the Biot number is indeed the cause of the mismatched θ distributions in Figure 82, the next case is a repeat of the simulations of Table 11, but change the thermal conductivity of the solid material to match the Biot number according to the requirement specified in Eq. (2.26). That is, the thermal conductivity of the solid was changed by the same ratio that the thermal conductivity of the freestream gas was changed from the baseline air case as shown in Table 12. The resulting θ distribution is shown in Figure 83. As expected, the θ distributions are again matched.

Table 12: Variation in *k* to match *Bi* in Set 4

Coolant	$k_c \left(\frac{W}{m \cdot K}\right)$	*FS*	$k_\infty \left(\frac{W}{m \cdot K}\right)$	$k_s \left(\frac{W}{m \cdot K}\right)$
Air	0.0242	Air	0.0242	0.1000
*Air**	0.0149	Ar*	0.0149	0.0614
*Air**	0.0156	CO_2*	0.0156	0.0646
*Air**	0.1389	He*	0.1389	0.5738

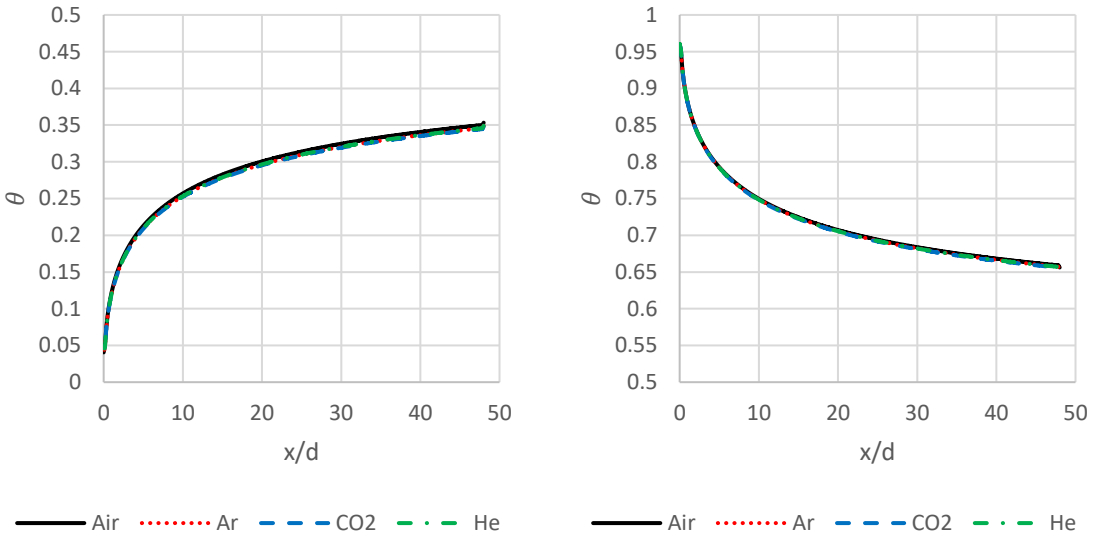

Figure 83: Internal cooling temperature distribution on the upper (left) and lower (right) surfaces with matched ACR, Re_c, Pr_c, and Bi with air as the coolant (Set 4)

The preceding computational simulations were performed on a simple geometry to test the efficacy of the nondimensional parameters appearing Eqs. (6.11) and (6.12) to match h/h_i as required to match ϕ as suggested by Eq. (2.17). It is unknown whether this theory applies to a more engine representative flow field with turbulence, an engine representative Biot number, and most importantly, the additional complexity of film cooling. After all, the need to match η prompted matched *ACR* to begin with. More practically, the objective is to understand how to appropriately scale gas turbine heat transfer experiments. Therefore, a more turbine-relevant geometry with both internal cooling and film cooling is examined next.

6.3. Film Cooled Flat Plate CFD

To further verify the utility of the Eqs. (6.11) and (6.12), the same gas properties are next tested on a more complex geometry: the flat plate with shaped film cooling holes. This is the same film cooled geometry previously used. Set 5 was constructed in the same manner as Set 2b but with the film cooled geometry and at a lower ACR. The freestream gas in again air at 320 K and the coolants are varied gases at 300 K. That is, the coolant flow rate was selected such that Re_c would be matched to the baseline air case. Then, to match *ACR*, the specific heat of the coolant gas was modified as indicated by the highlighted $c_{p,c}$ values in Table 13. Finally, the thermal conductivity of the coolant gas was modified to ensure Pr_c was matched. In this way, Re_∞, Pr_∞, Re_c, and Pr_c are all matched while *ACR* is matched, thereby satisfying Eq. (6.11) such that $\frac{h}{h_i}$ should be matched. Further, with both the freestream flow and k_s fixed throughout Set 5, the Biot number should be matched, thereby avoiding the insidious problem seen in Set 3. The resulting ϕ contours are shown in Figure 84 and the η distributions are shown in Figure 85.

Table 13: Properties of each run in Set 5

Coolant	$c_{p,c}\left(\frac{J}{kg\cdot K}\right)$	$k_c\left(\frac{W}{m\cdot K}\right)$	Re_c	Pr_c	***FS***	Re_∞	Pr_∞	***DR***	***VR***	***M***	***I***	***ACR***
Air	1006.4	0.0242	**2500**	**0.74**	Air	**5000**	**0.74**	1.00	0.50	0.50	0.25	**0.5**
*Ar**	847.5	0.0242	**2500**	**0.74**	Air	**5000**	**0.74**	1.32	0.45	0.59	0.27	**0.5**
*CO_2**	1314.5	0.0242	**2500**	**0.74**	Air	**5000**	**0.74**	1.46	0.26	0.38	0.10	**0.5**
*He**	905.0	0.0242	**2500**	**0.74**	Air	**5000**	**0.74**	0.13	4.19	0.54	2.28	**0.5**

Eq. (2.17) showed four properties must be matched to scale ϕ: χ, *Bi*, η, and the *h* ratio. As evident in Figure 85, each simulation agrees with common sense that $\eta = 0$ in the region upstream of the first coolant hole. In that region, only internal cooling is significant, as it was in Sets 1 through 4. Bryant et al. [27] showed that plenum and hole cooling are the two primary forms of cooling in this area and the film cooling effect on ϕ is negligible, but not exactly zero

due to streamwise conduction within the solid. Indeed, the ϕ distributions in that region are nearly identical in Figure 84, showing χ, *Bi*, and the *h* ratio are all matched there. The situation becomes more complex downstream of the first cooling hole for two reasons:

1) The adiabatic effectiveness, η, is nonzero so the ability of the scaling scheme to match η becomes critical to the ability to match ϕ.
2) The introduction of coolant to the hot gas side of the plate causes the gas properties within the boundary to differ somewhat from the freestream properties, especially directly in the film cooling plumes.

The experimental results of Fischer et al. [16] suggest matching *ACR* is effective at matching η with the 7-7-7 cooling hole geometry if the momentum flux ratio, *I*, is less than 0.6. Table 13 shows this is the case for air, argon, and CO_2; however, helium has a very high *I* value, as seen in Ref. [16] far exceeds the optimal value of $I \approx 1$ for η as much of the coolant mass is separated from the surface, providing little benefit in terms of η. While it is no surprise that air and argon both have very similar η contours, it was surprising, though, that the CO_2 case yielded somewhat lower η values than air and argon. Recall, however, that the CO_2 used in these simulations has altered c_p and *k* values so a direct comparison to experiment is impossible here. Further, *VR* with CO_2 is substantially lower than *VR* with both argon and air coolants. A stronger shear layer with the CO_2 may contribute to greater mixing with the freestream and therefore lower η values as predicted by the computational simulation.

While the lower ϕ obtained with CO_2 can be attributed at least partially to its lower η distribution in the region downstream of the coolant hole, the explanation for the behavior of the helium case is more complex. Indeed, the separation of the helium jet and its low η distribution compared to air and argon contributed to its lower ϕ distribution. Even with the generally lower

η distribution with helium, it is noteworthy that ϕ in that region is slightly greater than that of CO_2. Although it is difficult to say with certainty what causes this behavior, recall Note 2. That is, the introduction of coolant into the boundary layer would be expected to alter the external heat transfer coefficient from what it would be if it were influenced by the freestream gas alone. This demonstrates a possible deficiency in the formulation of Eq. (6.11) with the intent of matching h/h_i. Simply put, the formulation does not account for the introduction of coolant in the boundary layer and the associated property differences that influence the external heat transfer coefficient distribution.

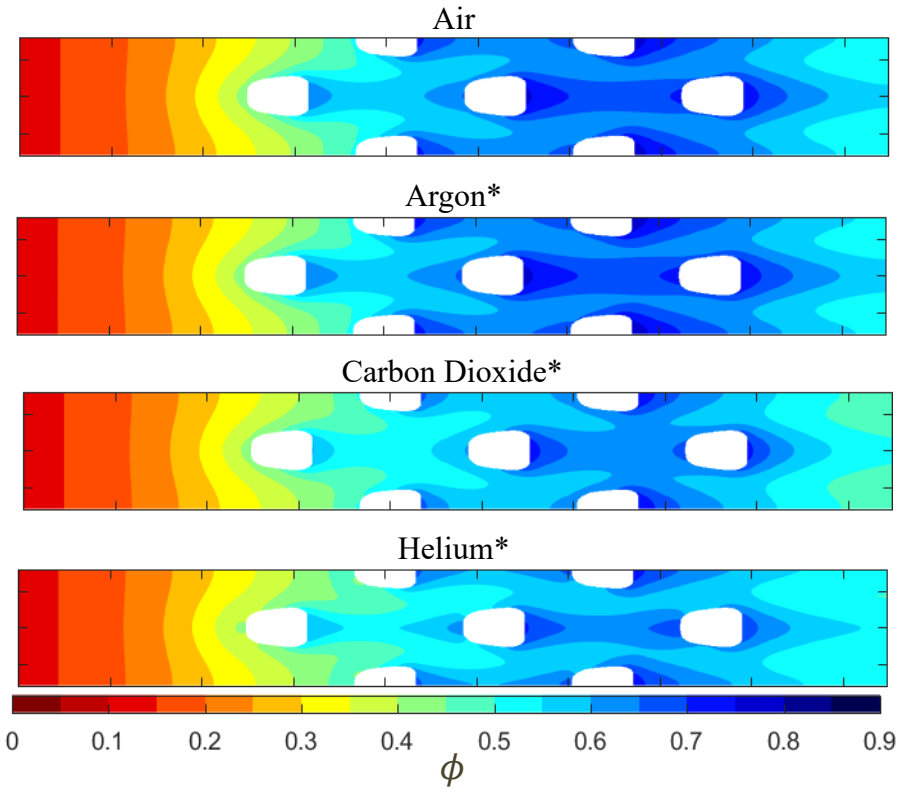

Figure 84: ϕ contours for Set 5 (film cooled plate)

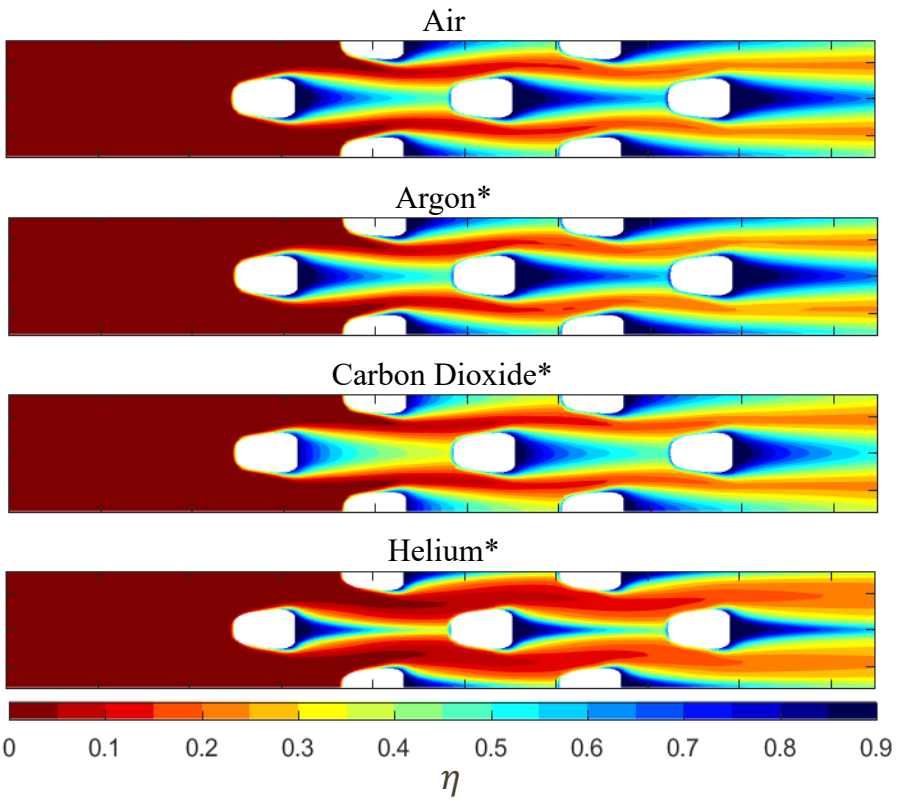

Figure 85: η contours for Set 5 (film cooled plate)

There is another technique to investigate heat transfer without mixing from film cooling. CFD can be used to remove the effect of film cooling, as discussed in Ref. 27 and shown in Chapters 3 and 4. Figure 86 shows the same conditions as the previous figure, with film cooling removed. The contours are nearly identical which shows that internal and external heat transfer are identical for each gas when the contribution of the coolant to the external heat transfer is eliminated. The freestream is identical for each gas; therefore, the external heat transfer is constant between gases. This further proves that matching the parameters previously discussed is sufficient to match the ratio of heat transfer coefficients.

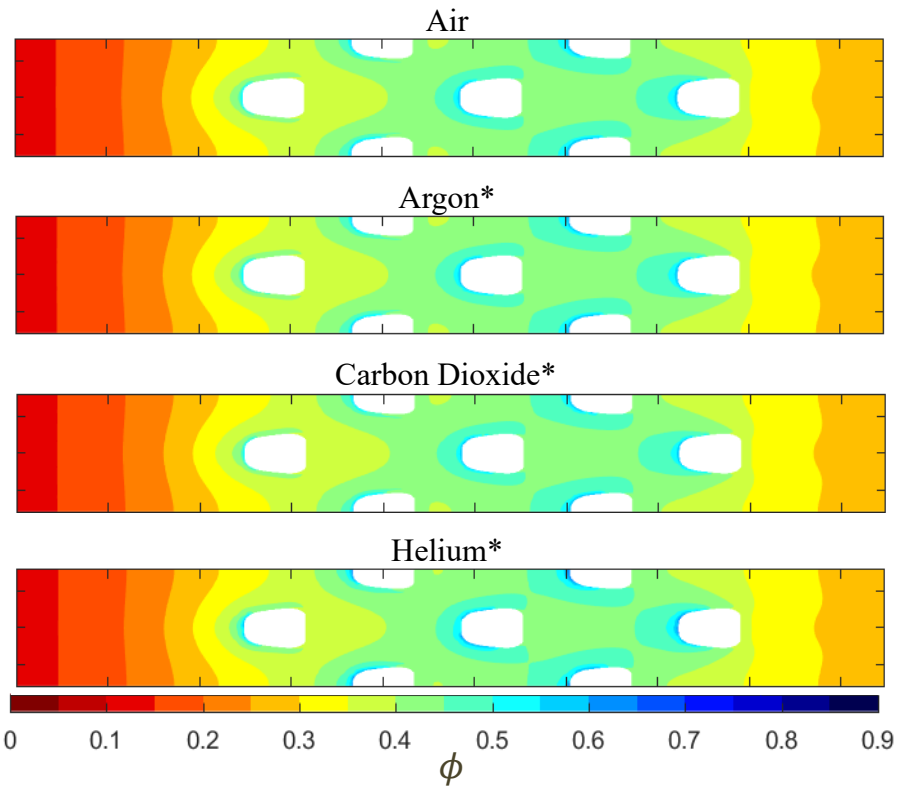

Figure 86: ϕ with film cooling removed, contours for Set 5 (film cooled plate)

6.4. Summary

This chapter established a theory to scale the ratio of internal and external heat transfer coefficients. It showed that matching Re_∞, ACR, and the ratio $\frac{Pr_\infty^q}{Re_c^p Pr_c^q}$ is necessary, though impossible without determining the coefficients p, q, and r. To circumvent this difficulty, each parameter was matched separately instead. Because matching five parameters individually over constrains the problem, individual gas properties were modified to confirm the theory on a simplified internal cooling geometry and the film cooled flat plate. This chapter accomplished a considerable portion of Objective 3. Part of Objective 3 was to find the necessary parameters to scale overall effectiveness. Combining this Chapter with Chapter 5 and the previous research fulfills two of the parameters needed to scale an overall effectiveness experiment. This is novel

because it is the first time any research has demonstrated the parameters needed to match heat transfer coefficients on a film cooled component and shown the effects on ϕ.

This page is intentionally left blank

7. Scaling Overall Effectiveness

Previous research and the last two chapters have shown the requirements necessary to match each parameter individually, but unfortunately, the problem generally becomes over-constrained when all the relevant parameters need to be matched simultaneously. While it is important to properly scale all parameters to conduct effective laboratory experiments, there have not been recommendations in the research regarding how to perform low temperature experiments most effectively under attainable conditions that will best allow matching the relevant parameters. This chapter accomplishes Objective 3 by demonstrating a methodology that an experimentalist may follow to help select low temperature experimental conditions that will allow for accurate prediction of the thermal state of turbine components at engine-relevant conditions.

7.1. Coolant Hole Warming Factor

The final parameter to match ϕ is the coolant warming factor χ, or how much heat is transferred to the coolant as it travels through coolant holes and channels. Wiese et al. [28] theorized that when ACR and Re_∞ are matched, the ratio

$$\xi = \frac{\mu_\infty c_{p,\infty}}{k_c} \tag{7.1}$$

must be matched to scale the coolant warming factor, χ. Conveniently, when ACR, Re_∞, Re_c, and Pr_c are matched for the ratio of heat transfer coefficients, the coolant warming factor is also matched. To show this, consider if each term was multiplied. Because each term is matched, then the product of them is also matched.

$$(ACR \cdot Re_\infty \cdot Re_c \cdot Pr_c)_{exp} = (ACR \cdot Re_\infty \cdot Re_c \cdot Pr_c)_{eng} \tag{7.2}$$

Since each term is matched, then the inverse of an individual term is also matched.

$$\left(\frac{1}{ACR}\cdot\frac{1}{Re_\infty}\cdot Re_c\cdot Pr_c\right)_{exp}=\left(\frac{1}{ACR}\cdot\frac{1}{Re_\infty}\cdot Re_c\cdot Pr_c\right)_{eng} \quad (7.3)$$

Expanding and reducing terms leaves only the ratio necessary to scale the coolant warming scaling, ξ.

$$\left(\frac{\mu_\infty c_{p,\infty}}{k_c}\right)_{exp}=\left(\frac{\mu_\infty c_{p,\infty}}{k_c}\right)_{eng} \quad (7.4)$$

The theory they developed indicates that this parameter, ξ, scales coolant warming when ACR and Re_∞ are matched.

Wiese et al. conducted a set of experiments to measure χ using a single hole on the leading edge model discussed in Chapter 4. Table 14 shows the ξ values for the four coolant gases used in the tests. Figure 87 shows the resulting variation in χ with matched ACR. Overall, all four gases collapse together moderately well. This outcome is surprising because the theory states that to match χ, then ACR, Re_∞, and ξ must all be matched. But Table 14 shows that ξ is only matched with Argon and CO_2. There were a few sources of experimental uncertainty that could be the cause. They could not verify whether the coolant flow was fully developed or whether the bulk temperature was correctly measured. In conclusion, though experiments were not able to confirm the theory, the theory Wiese et al. developed is a theoretical basis for scaling coolant warming.

Table 14: Mean ξ values and maximum deviation for cases with matched ACR [28]

Gas	ξ
Air	0.75 ± 1%
Argon	1.10 ± 1%
CO_2	1.15 ± 3%
Helium	0.13 ± 2%

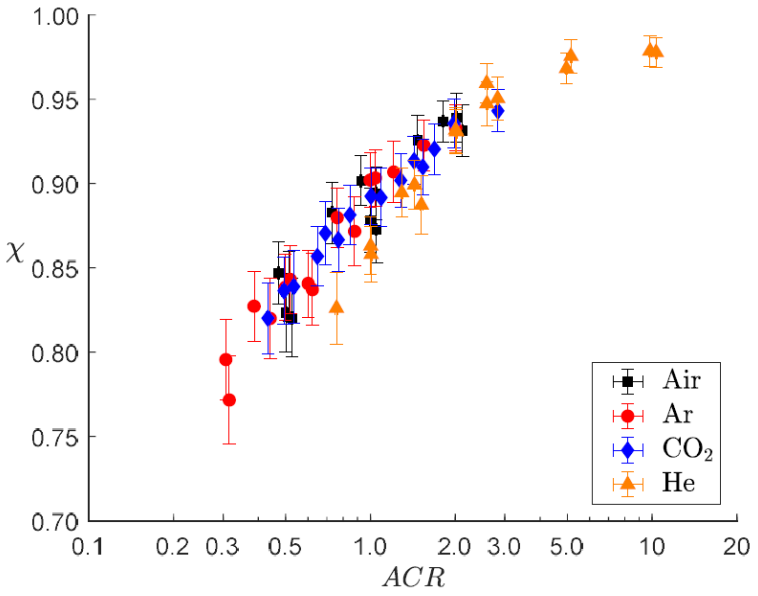

Figure 87: χ variations with ACR for four gases

Coolant warming was the final parameter in Eq. (2.17) needed to scale overall effectiveness with an anisotropic material, as Objective 3 requires. The first was adiabatic effectiveness, which Fischer [16] and McNamara [29] showed can be scaled using ACR. Next, Chapter 5 showed how to scale the Biot number with an isotropic or anisotropic material. Third, Chapter 6 explained and demonstrated the parameters necessary for scaled internal cooling and h/h_i. Finally, Wiese [28] developed a theory for scaling coolant warming. Overall effectiveness can be scaled at low temperature by using experimental conditions which satisfy the scaling requirements for all four parameters simultaneously.

7.2. Analysis

Before a laboratory test can be designed, the engine case must first be identified. This is the condition that the lab experiment attempts to match. Table 15 describes the engine representative condition used in the present analysis, identical to Chapter 5.

Table 15: Engine condition

Freestream Gas	Air
Freestream Temperature	2000 K
Coolant Gas	Air
Coolant Temperature	1000 K
Overall Pressure Ratio	40
Re_∞	5000
ACR	0.5

Several laboratory conditions must be chosen carefully to ensure $\eta, Bi, h/h_i$, and χ are approximately matched simultaneously. The design of the test cases in the following sections follows the same criteria, regardless of the chosen conditions. First, the freestream and coolant gases are selected so that Pr_∞ and Pr_c are approximately matched, which are conveniently at most weak functions of temperature. Next, the temperatures of the gases are carefully selected such that when the freestream flowrate is chosen such that Re_∞ is matched and the coolant flowrate selected such that *ACR* is matched, Re_c is at least not far off, although the problem is generally over-constrained at this point. Finally, the model material itself must have a thermal conductivity as close as possible to the ideal lab material which is driven by Eq. (2.17), informed by the selection of gas and temperature. This material thermal conductivity selection is complicated because the thermal conductivity of the material at both engine and lab conditions is a function of the unknown material temperature. As a first approximation, assuming ϕ = 0.6 is reasonable, but computational simulations like those performed here can help evaluate the validity of such an approximation.

The freestream and coolant fluid choice and temperature choice have effects on Pr_∞, Re_c, Pr_c and ξ. The difference between a parameter at any condition and the engine condition is quantified using the residual. An ideal lab condition minimizes the normalized residual difference in each of the four quantities. The normalized residual difference, r, is

defined as the difference between the lab condition and the engine condition, normalized by the engine condition. For example, the residual in Pr is defined as

$$\mathrm{r}_{Pr} = \frac{Pr_{lab} - Pr_{eng}}{Pr_{eng}} \tag{7.5}$$

This residual is then converted to a percentage for visualization. For simplicity, air is analyzed first as both the coolant and freestream gases. The freestream Reynolds number is set to $Re_\infty = 5{,}000$ and the coolant flow rate is set to maintain $ACR = 0.5$ to match the engine condition in Table 4. The chosen design space is 200-700 K which encompasses a variety of low temperature experiments in the literature. Figure 88 shows the normalized residual in percentage for Pr_∞ and Pr_c. Pr varies with temperature in the same way for both the coolant and the freestream since both are air. However, the values differ because of the different temperatures, and therefore different Pr, between the coolant and freestream at engine condition.

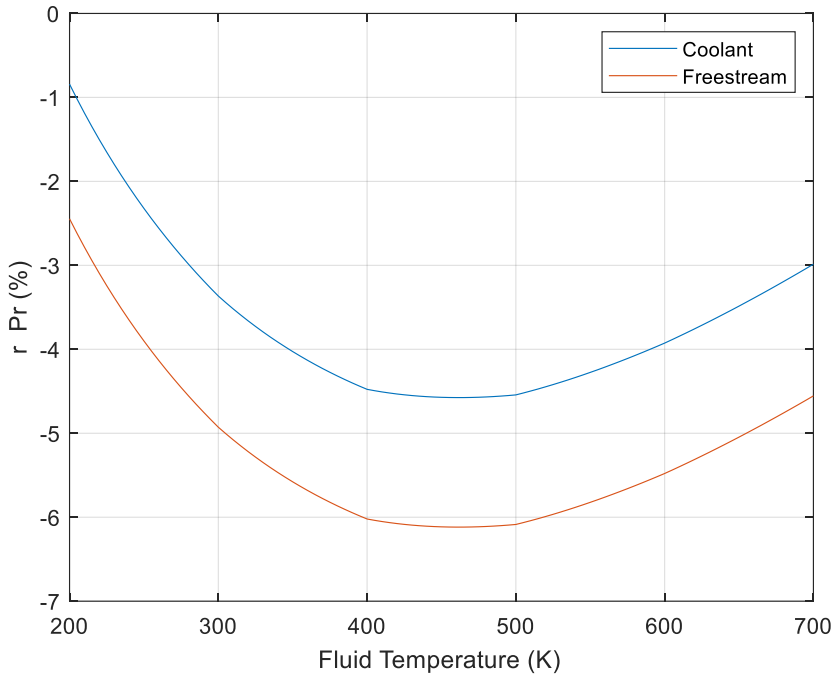

Figure 88: Normalized residual difference for Pr_c and Pr_∞ with temperature

The Re_c residual is affected by the properties of both the coolant and freestream changing with temperature. These changes affect the Reynolds number because V_c is set to ensure ACR is matched, and *ACR* includes freestream properties. Therefore, the difference in Re_c is a two-dimensional map for variations in coolant and freestream temperature, as shown in Figure 89. With Figure 89 it is clear what the ideal T_c is for a given T_∞ such that Re_c is matched at the same time as ACR: any area with low residual, white in Figure 89. The exact threshold for what is permissible or not for an experimentalist is unique to each geometry and purpose. The generalized code for calculating each residual is provided in Appendix B: Code for Calculating NRMSD. Given any engine condition and coolant gas properties, anyone can calculate the ideal conditions for their experiment using this code.

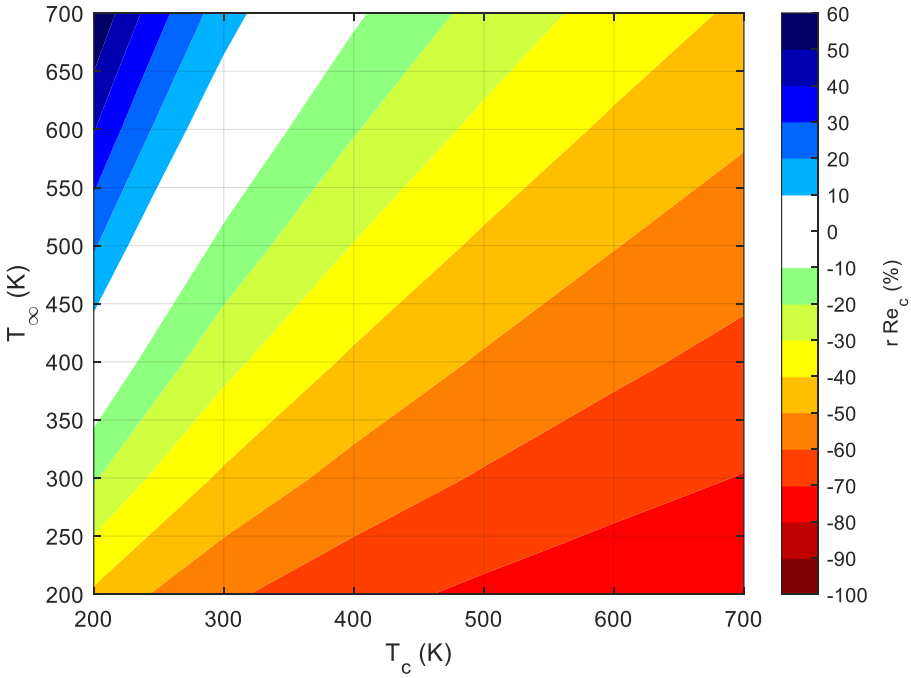

Figure 89: Normalized residual difference in Re_c with coolant and freestream temperatures

The last parameter to match is the coolant warming factor, χ, which is scaled by ξ. Figure 90 shows the normalized residual map. It looks nearly identical to the Re_c map because it is also

affected by changes in both freestream and coolant properties; however, there are small differences between the two because ξ is defined using different coolant and freestream parameters. Nevertheless, the similarity between Figures 89 and 90 is convenient in that errors in both Re_c and ξ can be minimized approximately simultaneously as required for such an experiment.

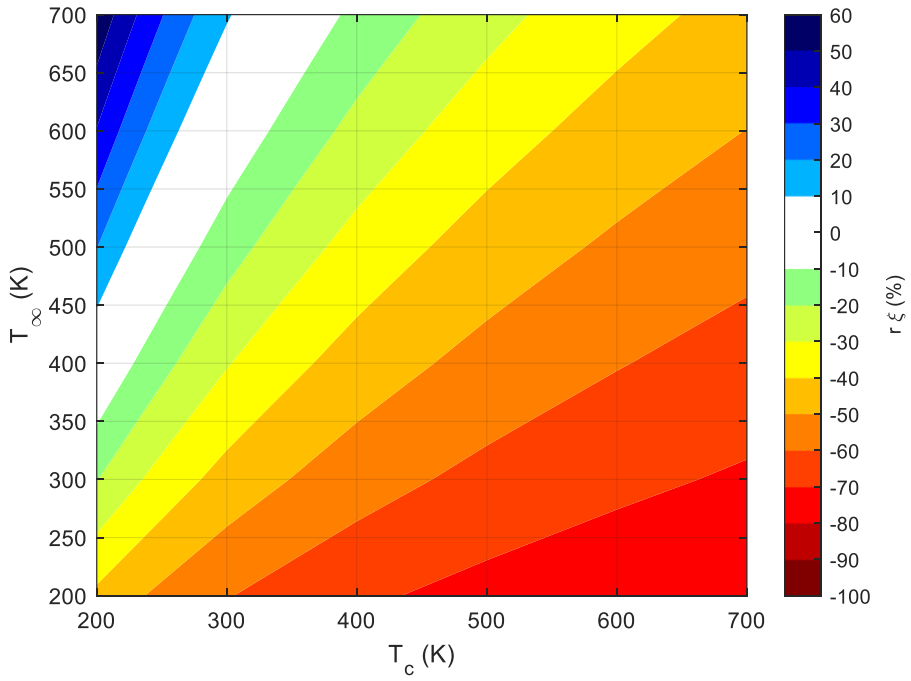

Figure 90: Normalized residual difference in ξ with coolant and freestream temperatures

7.2.1. Selection of Laboratory Fluid Conditions

To quantify the difference in these four quantities at any laboratory condition versus the engine condition the Normalized Root Mean Square Difference (NRMSD) is used. This quantity uses the previously defined normalized residuals, then the residuals are squared, summed, divided by the number of terms, and the square root is taken:

$$NRMSD = \sqrt{\frac{r_{Pr_c}^2 + r_{Re_c}^2 + r_{Pr_\infty}^2 + r_\xi^2}{4}} \tag{7.6}$$

Finally, the NRMSD is converted to a percentage for clearest visualization. Ultimately, this method produces a clear comparison of unlike terms. As an initial starting point, the ideal lab condition minimizes all four residuals with equal weighting given to each. It is evident that some parameters are more influential than others at various parts of the coolant flow path. Additional refinement will be done in the future to tailor NRMSD to the sensitivity to each parameter. The NRMSD is used to quantify the overall difference in relevant parameters between a set of experimental conditions and the engine conditions they are intended to simulate. Therefore, the fluid and temperature with the lowest NRMSD are hypothesized to be the best conditions for an experiment intended to yield an engine-relevant ϕ distribution.

Figure 91 shows the NRMSD for air using the same engine condition identified in Table 15. In the contour plot, blue levels have the lowest difference from the engine condition. White areas have NRMSD higher than 30%. The ideal lab conditions according to the plot have a higher T_∞ than T_c. For example, a test at the lab conditions described by Stewart and Dyson [20], $T_\infty = 500\ K, T_c = 250\ K$ has NRSMD under 5% whereas the lab condition in Chapter 6 ($T_\infty = 320$ K, $T_c = 300$ K) has NRSMD between 25% and 30%. One interesting aspect to this contour is the centerline of the low NRMSD band is also the line where the freestream temperature is twice the coolant temperature. This line is a common choice for experimental test conditions because the density of air approximately doubles with temperature. Therefore, test points along this line will have matched density ratio. It is important to emphasize that the sensitivity of ϕ to each parameter is yet unknown and equal sensitivity to each parameter is assumed in the NRMSD. As such, two test conditions with equal NRMSD may have different ϕ contours because the parameters that make up NRMSD vary between the two conditions.

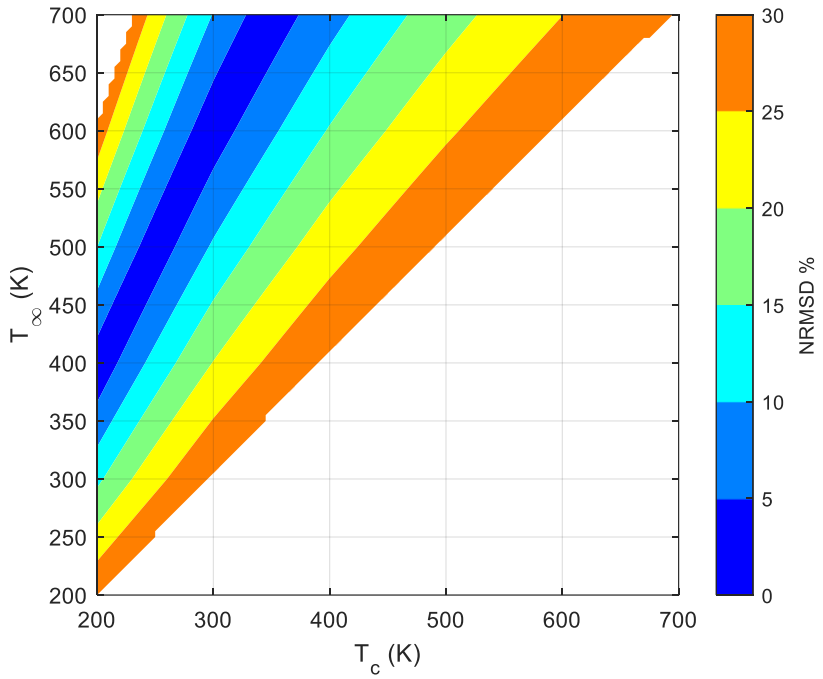

Figure 91: Ideal lab conditions with air coolant (white regions have NRMSD > 30%)

Similar plots can be generated for a variety of gases, and these can be used to determine the optimal test conditions for a given operating range and constraints. Carbon dioxide (CO_2) has been used in laboratory-scale film cooling experiments because its elevated density compared to air conveniently allows the experimentalist to have a density ratio of two by having the CO_2 coolant only moderately cooler than the freestream air. As shown in Figure 92, the ideal lab conditions with CO_2 are different from the ideal lab conditions with air due to the differences in properties. Some low temperature experiments with CO_2 have a lower NRMSD than the same temperatures with air coolant. For the experimentalist limited to approximately room temperature freestream air, a CO_2 coolant experiment appears particularly attractive and for that reason, further analysis of such CO_2 coolant experiments is conducted herein. Other gases, such as Argon or Helium have much smaller areas of low NRMSD at atypical lab conditions.

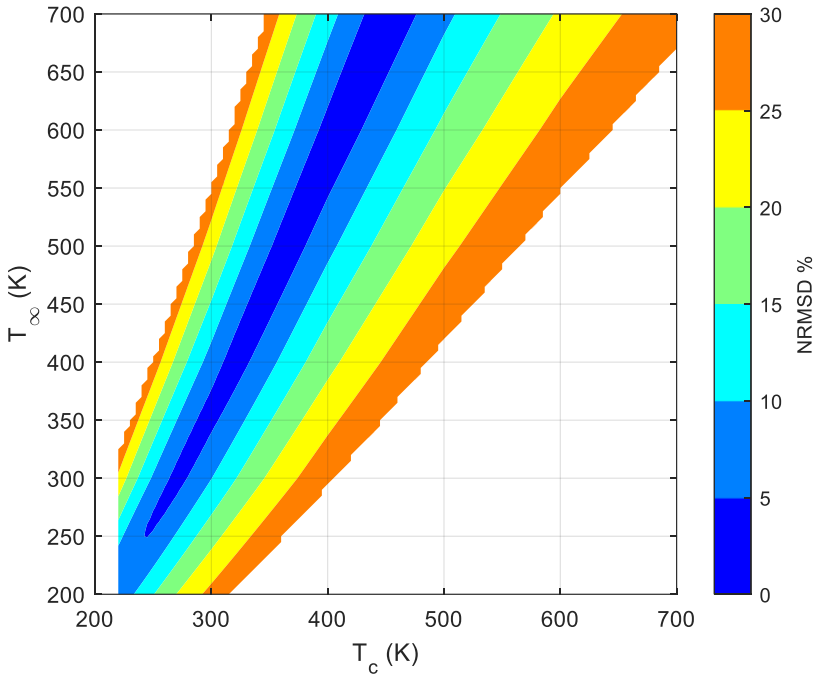

Figure 92: Ideal lab conditions with carbon dioxide coolant

7.2.2. Selection of Laboratory Material

Model material choice is another important factor in measuring appropriate overall effectiveness in an experiment. As previously discussed, the material thermal conductivity must be selected to closely match the ideal lab material. This ideal lab material depends on the thermal conductivity of the freestream gas at engine condition, the material used at engine condition, and the thermal conductivity of the freestream gas at the lab condition, as shown in Eq. (2.22). For this analysis, the freestream gas at engine conditions is assumed to be pure air and the turbine components are either Inconel 718 or a SiC/SiC CMC like that used in Chapter 5. As previously discussed, a different material is necessary for scaling a SiC/SiC CMC in laboratory conditions. Figure 93 shows how poorly a SiC/SiC at laboratory conditions scales ϕ. The ideal material thermal conductivity should approximately match air's k ratio between the engine and laboratory

condition. Chapter 5 showed the ideal material thermal conductivity for the specific condition where the coolant temperature is exactly half the freestream ratio and the average $\phi = 0.6$.

Figure 94 shows the ideal material k for this condition. Note that air's thermal conductivity is shown on a separate axis on the right. The actual material temperature varies based on the freestream temperature, coolant temperature, and average ϕ. Because the variation of thermal conductivity with temperature for Inconel is like air's, Inconel is naturally very close to the ideal k for most of the temperature range. Conversely and unlike air, the SiC/SiC CMC thermal conductivity *decreases* with increasing T and therefore another material is needed to conduct scaled ϕ experiments. If the same CMC is used in a low-temperature experiment, its thermal conductivity is too high to appropriately match the Biot number, contributing to an uncharacteristically large amount of internal cooling and the erroneously large prediction of ϕ observed in Figure 93.

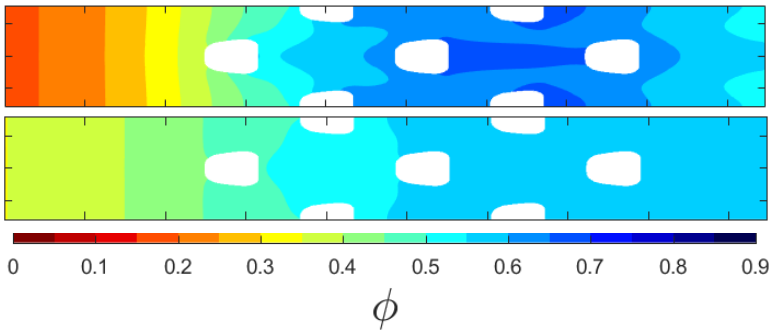

Figure 93: ϕ contours for (top) a SiC/SiC CMC with air freestream at 2000K and air coolant at 1000 K and (bottom) a SiC/SiC CMC with air freestream at 320 K and air coolant at 300 K

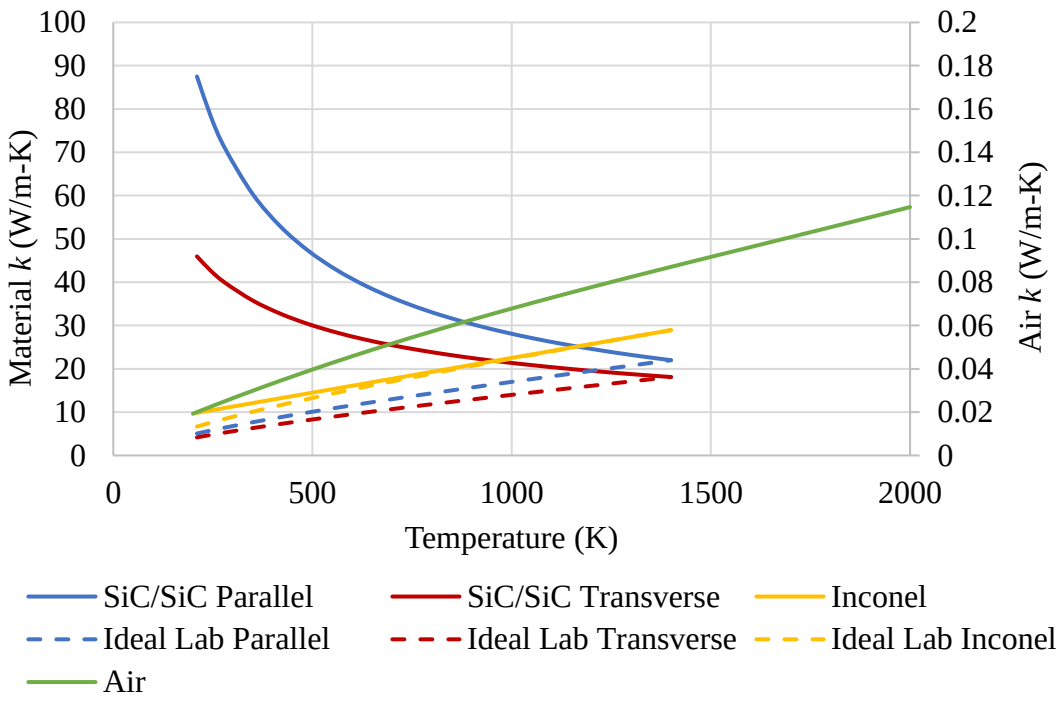

Figure 94: Air and ideal material thermal conductivity for Inconel and a SiC/SiC CMC (for a temperature ratio of 2.0)

7.3. Lab Conditions

To demonstrate this technique, two lab temperature conditions are compared next: one optimized for air coolant and the other CO_2 coolant, via Figures 91 and 92, respectively. However, for completeness, each condition has also been simulated with both air and CO_2 coolant to evaluate the non-optimum cases. The results of these four total simulations of experiments are compared to the simulation of the high temperature, high-pressure engine condition. The fluid properties for the engine and all four lab cases are shown in Table 16. The two cases with low NRMSD would be expected to have smaller differences from the engine condition than the two cases with higher NRMSD. Lab Case 1 has a low predicted error, NRMSD=3.4%. It uses air as the coolant gas at 250 K and air as the freestream gas at 500 K. The total difference is derived from the four parameters that comprise NRMSD. The coolant Prandtl

number is 2% lower than the engine condition, the coolant Reynolds number is 1% higher, the freestream Prandtl number is 6% lower, and finally, the coolant warming factor is 1% lower. These values constitute the low NRMSD for this case. *ACR* and the freestream Reynolds number are already matched. Additionally, I is below the threshold value, so ACR is still expected to scale η. The lowest NRMSD for air across the given operating range is 3.1%. It never reaches zero because the residuals, such as the Prandtl numbers, are never zero.

Table 16: Properties at all four lab conditions

Case	T_∞	T_c	Coolant	Re_∞	ACR	I	Pr_c	Re_c	Pr_∞	ξ	NRMSD
Engine	2000	1000	Air	5000	0.50	0.15	0.73	4282	0.74	1.25	
1	500	250	Air	5000	0.50	0.13	0.71	4325	0.70	1.24	3.4%
2	350	300	CO_2	5000	0.50	0.20	0.77	4111	0.70	1.26	4.2%
3	350	300	Air	5000	0.50	0.22	0.70	2822	0.70	0.79	25.1%
4	500	250	CO_2	5000	0.50	0.13	0.78	6894	0.70	2.16	47.7%

Next, the best material must be chosen to scale Bi. The freestream and coolant temperatures are now known, and the material temperature can be estimated, at least for material selection purposes, by assuming an average $\phi = 0.6$ (Chapter 5). Using the methodology to create Figure 94, but for the temperatures used presently ($T_\infty = 500\ K, T_c = 250\ K$), the ideal lab condition thermal conductivity can be determined for simulating either the engine condition CMC or Inconel. Several materials with thermal conductivities close to these ideal values are plotted in Figure 95 using data compiled from Refs [68], [69], [70], and [71]. The red markers in the figure are the ideal *k*. There are two markers for the CMC because it has anisotropic *k*. The higher value is the thermal conductivity in the parallel direction and the lower value is the transverse direction. Chapter 4 showed that an isotropic material with thermal conductivity equal to only the parallel component of *k* in an anisotropic material comes closest to matching ϕ. Therefore, the isotropic material with *k* closest to the higher, parallel component is chosen to scale *Bi* for the

anisotropic CMC. For all four laboratory cases, the engine condition uses the CMC rather than Inconel. For both lab conditions in Table 16, Ti-6Al-4V (Ti64) is used because it has the closest thermal conductivity to the ideal material. Ref. [72] also used this material to conduct matched Biot number experiments for a similar range of laboratory conditions. As a bonus, this is a relatively inexpensive and easily machined material.

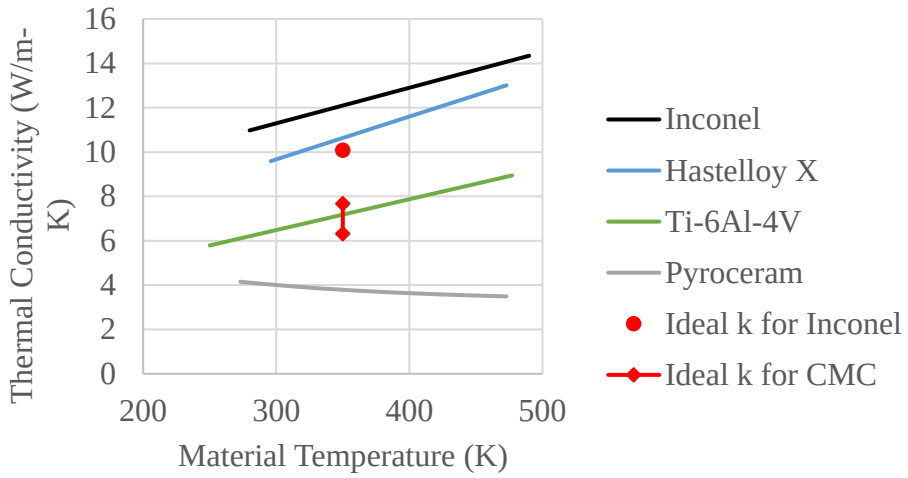

Figure 95: Thermal conductivities of various materials and the ideal material thermal conductivities (shown in red) for $T_\infty = 500\ K, T_c = 250K$

Now that the fluidic and material conditions have been identified, the next step is to compare adiabatic and overall effectiveness for the engine and laboratory conditions. Recall that η is one of the factors that must be matched to scale ϕ, per Eq. (2.17). Figure 96 shows the η contour for the engine and lab conditions. It is identical to Figure 68 because the conditions are the same. Chapter 5 showed that a 0.08 mismatch in η would be expected to cause a 0.05 difference in ϕ. The overall effectiveness plots for both conditions are shown in Figure 97. At lab condition, the overall effectiveness is slightly underpredicted over the entire surface, by 0.05 maximum. Upstream of the first film cooling hole, where $\eta = 0$, there is good agreement between the engine and lab condition. This shows that the internal heat transfer and conduction heat transfer

are scaled well. Downstream of the cooling holes, where $\eta \neq 0$, the differences increase. Therefore, it is likely that mixing is imperfectly matched between the two cases. This is supported by the differences in the η plots. Overall, this result shows that film cooling experiments using Ti64, air freestream at 500 K, and air coolant at 250 K scale very well to a SiC/SiC component at engine condition.

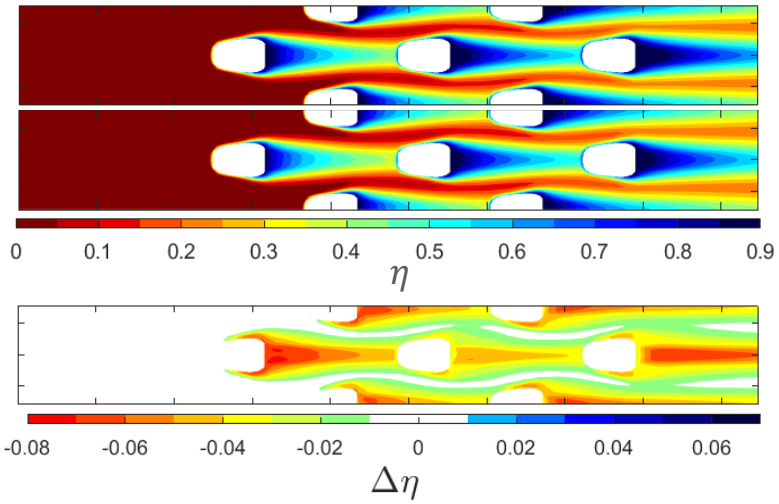

Figure 96: Contours of (top) η for air freestream at 2000K and air coolant at 1000 K, (middle) η for air freestream at 500 K and air coolant at 250 K, and (bottom) $\Delta\eta\ (\eta_{lab} - \eta_{engine})$

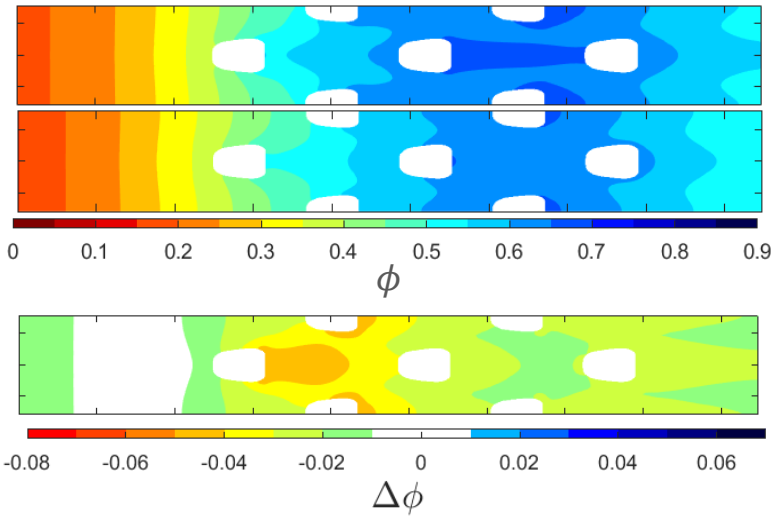

Figure 97: Contours of (top) ϕ for a SiC/SiC CMC with air freestream at 2000K and air coolant at 1000 K, (middle) ϕ for Ti64 with air freestream at 500 K and air coolant at 250 K, and (bottom) $\Delta\phi\ (\phi_{lab} - \phi_{engine})$

An interesting aspect of this specific experimental flow condition occurs if the engine condition uses Inconel instead of the CMC. According to Figure 95, Hastelloy X is the closest ideal material at the lab condition for an engine case with Inconel. This is notable because Ref. [20] and Chapter 5 have demonstrated that Inconel has low Bi error at lab conditions. Figure 98 shows a comparison of the engine condition with Inconel (top) to the lab condition with Hastelloy (middle) and Inconel (bottom). Figure 99 shows the $\Delta\phi$ contours that compare the two lab materials to the engine case. Overall, both materials scale ϕ well, within 0.02 of the engine condition; however, Hastelloy does slightly better, on average, than Inconel at matching the engine condition. The largest benefit of using Hastelloy instead of Inconel to simulate Inconel at engine conditions is evident on the upstream and downstream edges, where conduction effects from internal and hole cooling dominate, and the influence of the Biot number is largest.

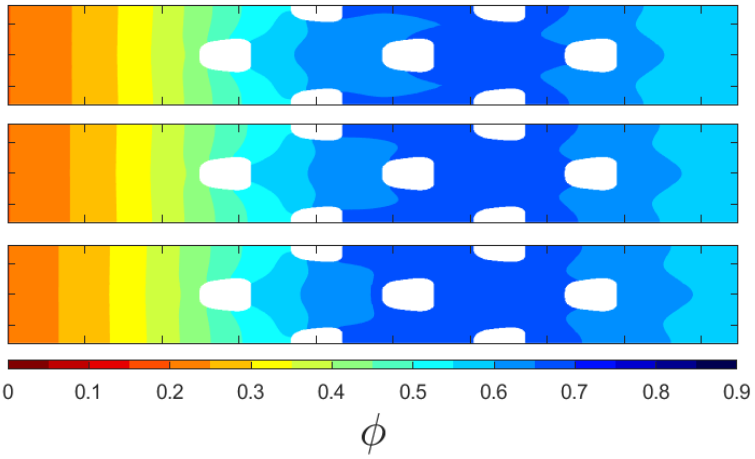

Figure 98: ϕ contours for (top) Inconel 718 with air freestream at 2000K and air coolant at 1000 K, (middle) Hastelloy X with air freestream at 500 K and air coolant at 250 K, and (bottom) Inconel 718 with air freestream at 500 K and air coolant at 250 K

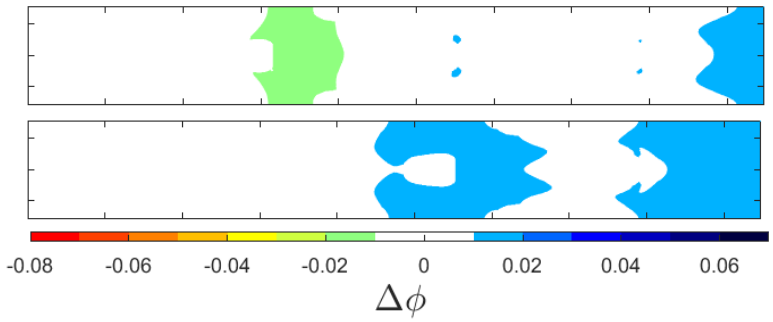

Figure 99: $\Delta\phi$ $(\phi_{lab} - \phi_{engine})$ contours for (top) Hastelloy X with air freestream at 500 K and air coolant at 250 K, and (bottom) Inconel 718 with air freestream at 500 K and air coolant at 250 K

Next, another case with low NRMSD is examined. Lab Case 2 uses freestream air at 350 K and CO_2 coolant at 300 K. The NRMSD is calculated from the properties shown in Table 16, to be 4.2%, similar in magnitude to that of Case 1. The lowest NRMSD for CO_2 across the given operating range is 2.4%, but this occurs at the highest freestream temperature, as shown in Figure 92. A lower temperature test point was chosen to align with typical experimental temperatures, albeit with a slightly higher NRMSD. Because this case has a different freestream and coolant temperature than Case 1, the material temperature is also different and material choice must be reexamined. Figure 100 shows that the ideal material for this case has a parallel thermal conductivity slightly lower than Ti64, but it is still the closest material shown. Therefore, Ti64 is again chosen with more error expected in this case due to mismatched *k*.

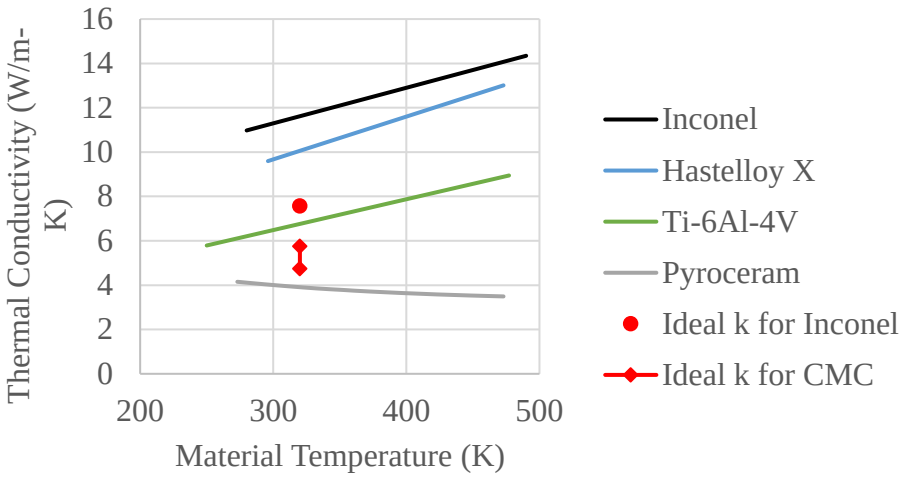

Figure 100: Thermal conductivities of various materials and the ideal material thermal conductivities (shown in red) for $T_\infty = 350\ K, T_c = 300K$

The adiabatic and overall effectiveness contours at this condition are examined next. The plots are shown in Figure 101. The adiabatic effectiveness contours match within $\eta < 0.03$, which indicates any differences in ϕ are not due to mismatched η. Figure 102 shows the overall effectiveness plots. Overall, the differences in ϕ are less than 0.03 across the entire surface. The upstream edge has a comparatively lower ϕ than the center, film cooled region where ϕ is more closely matched. This region is dominated by internal heat transfer and conduction through the material since $\eta = 0$ there. One possible cause for the slight mismatches could be the material choice. Recall that according to Figure 100, the thermal conductivity of the chosen material, Ti64, is only slightly higher than would be desired to simulate a CMC at engine conditions, in addition to being isotropic, unlike the CMC to which it is compared.

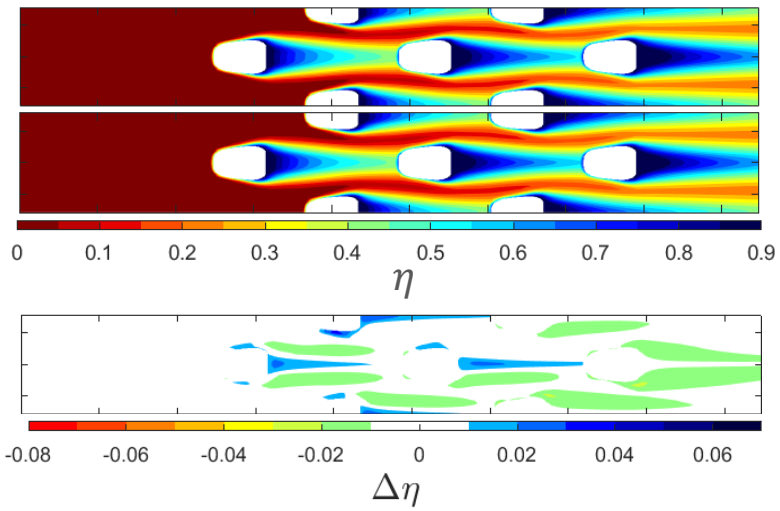

Figure 101: Contours of (top) η for air freestream at 2000K and air coolant at 1000 K, (middle) η for air freestream at 350 K and air coolant at 300 K, and (bottom) $\Delta\eta\ (\eta_{lab} - \eta_{engine})$

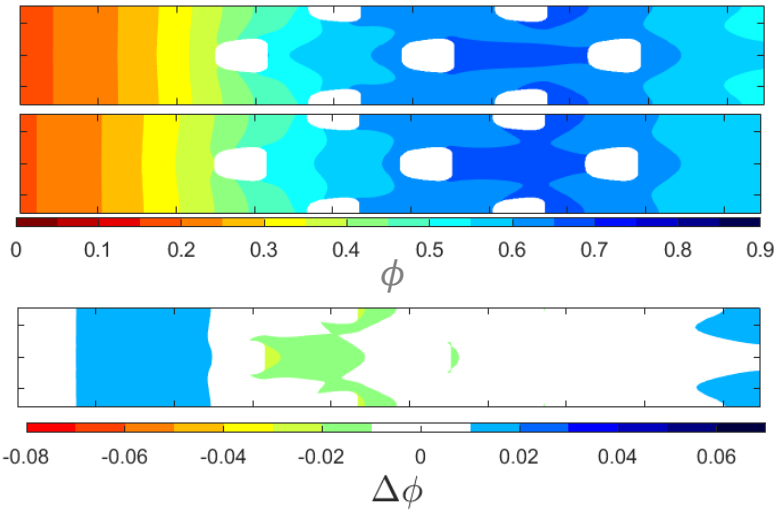

Figure 102: Contours of (top) ϕ for a SiC/SiC CMC with air freestream at 2000K and air coolant at 1000 K, (middle) ϕ for Ti64 with air freestream at 350 K and air coolant at 300 K, and (bottom) $\Delta\phi\ (\phi_{lab} - \phi_{engine})$

Now that experimental conditions with low NRMSD have been shown to be effective in scaling, ϕ, the next two cases demonstrate the effect of conducting experiments at conditions with higher NRMSD. These two test points are Cases 3 and 4 shown in Table 16. The cases also use Ti64 since they are at the same conditions that have been previously described. The

centerline ϕ plots are shown in Figure 103. The difference between each lab case and the engine case is plotted in Figure 104 which shows centerline $\Delta\phi$. The gaps in the lines are due to the film cooling hole exits. The cases with air coolant are plotted with solid lines and the cases with CO_2 coolant are plotted with dashed lines. Additionally, the cases with the hotter freestream, $T_\infty = 500\ K$ are plotted in red and the cooler freestream $T_\infty = 350K$ are plotted in blue. The cases are listed in order in the legend. Cases 3 and 4, with larger NRMSD, are plotted using asterisks. Despite large NRMSD, neither Case 3 nor 4 show large $\Delta\phi > 0.06$ from the engine case. In fact, downstream of the first coolant hole, Case 3 more closely matches the engine case than Case 1 despite having a much higher NRMSD.

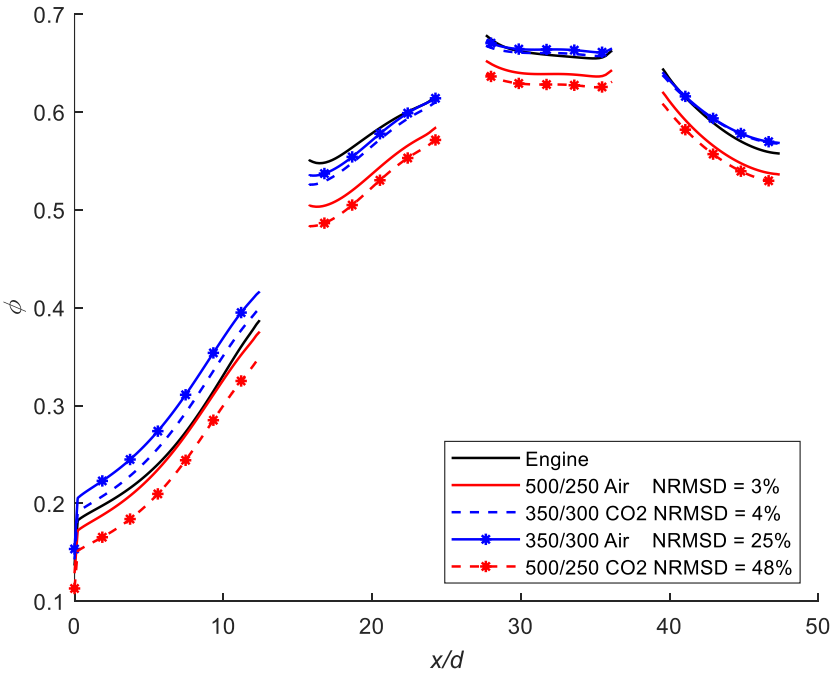

Figure 103: Centerline ϕ for the SiC/SiC CMC engine case and four lab cases using Ti64

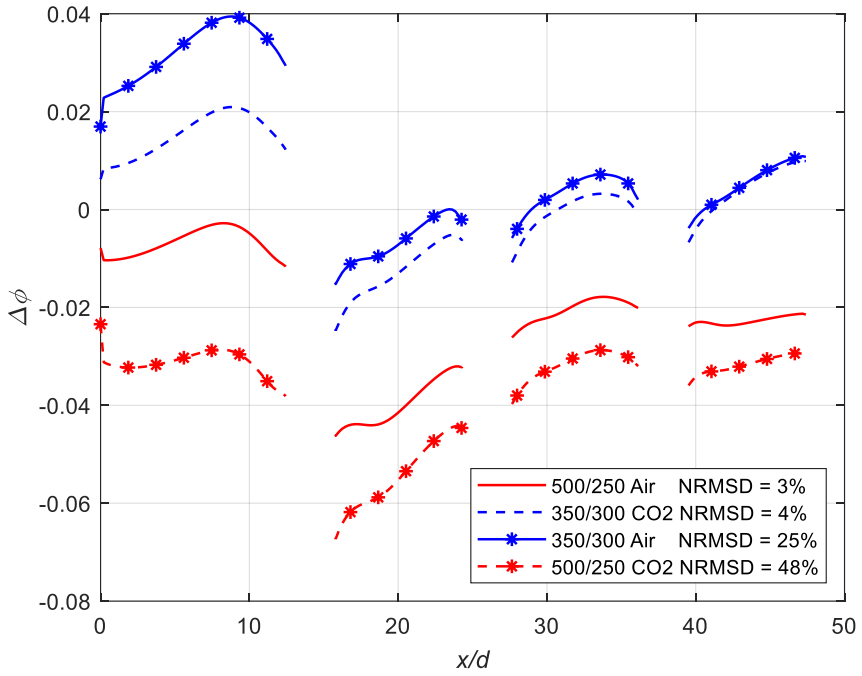

Figure 104: Centerline $\Delta\phi$ for the SiC/SiC CMC engine case and four lab cases using Ti64

There are several possible sources for this unexpected result. To begin, the differences in each parameter in Eq. (2.17) are examined. Though the primary focus of this chapter, NRMSD accounts for only two parameters: h/h_i and χ, neither of which influence η since it was assumed that η would at least be approximately matched through *ACR* (provided $I < 0.6$ as indicated in Ref. [16]) The fluidic heat transfer effects are also influenced by η. The adiabatic effectiveness plot for Case 1, Figure 96, shows that there are some differences between the engine and lab cases. Figure 105 shows the adiabatic effectiveness centerline values for all four cases. The centerline η values differ by less than 0.06 everywhere and there is not a strong correlation between NRMSD and the quality of η matching. In the film cooling dominated regions, the two cases with freestream at 500 K and coolant at 250 K yield the greatest differences from the engine condition. Therefore, it is likely that these cases will have the most different heat transfer due to the coolant and freestream mixing to form the film downstream of the coolant hole exits.

Because the η in these two cases is too low, this helps explain why ϕ is also lower downstream of the film cooling hole exits.

Another method to quantify the differences due to film cooling is to use artificial boundary conditions, as demonstrated in Ref. [27]. This method uses a one-sided outlet condition at the exit of each film cooling hole. The other side, which faces the freestream, is assigned a wall condition. Therefore, only the effect of film cooling is removed, and all internal cooling is unaffected. Figure 106 shows the centerline ϕ with film cooling removed for the engine and all four lab conditions. Unlike ϕ in Figure 103, removing film cooling shows that the first two cases with low NRMSD come closest to matching the engine condition. This finding shows the importance of matching η and mixing to match ϕ. Take the freestream at 500 K and air coolant at 250 K case (Case 1) as an example: with film cooling, this experimental condition appeared to not match ϕ well in the film cooling region (Figure 103). However, when film cooling is removed (Figure 106), it's clear that the mismatch in η and mixing was at least partially responsible for the mismatch in fluidic conditions.

The effect of film cooling is more than just η. As the coolant exits the film cooling holes, it mixes with the freestream as it travels downstream. This mixing means that the film properties, such as $\rho, c_p, k,$ and μ, vary depending on how the film mixes and spreads over the surface. The film itself has properties somewhere between the freestream and the coolant. The analysis for matching internal cooling and the Biot number assumes constant properties on each side of the surface. Therefore, the film mixing likely causes mismatches in both parameters.

The Biot number must also be considered. Recall from Figure 95 and Figure 100, that the material choice was not perfect for either condition. In particular, Ti64 was higher than the ideal

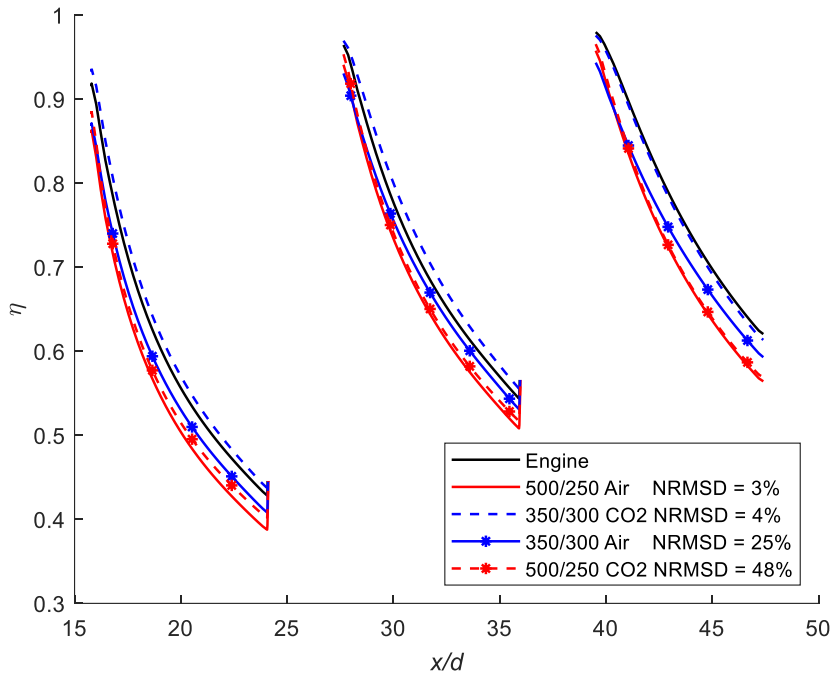

Figure 105: Centerline η for the SiC/SiC CMC engine case and four lab cases using Ti64

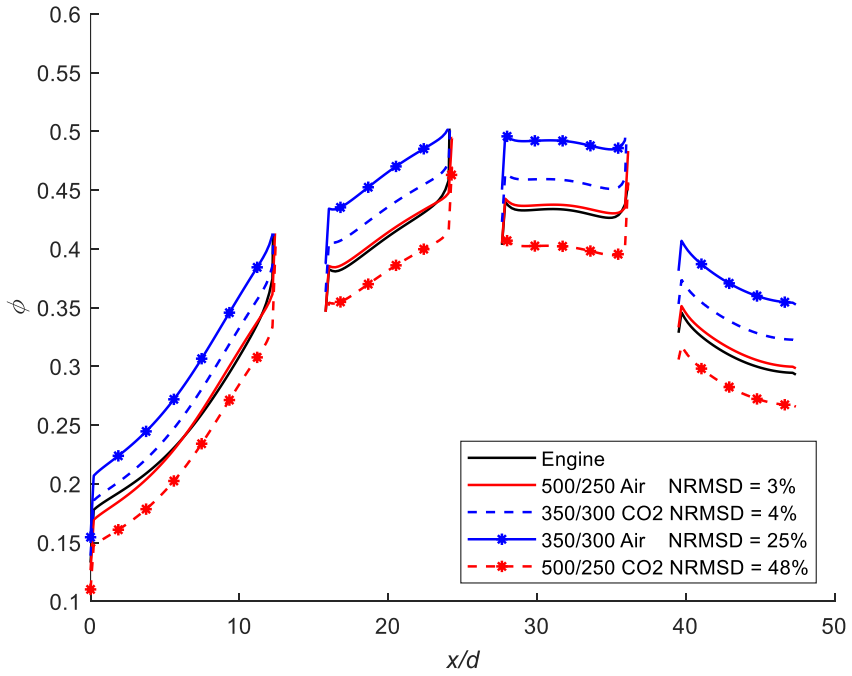

Figure 106: Centerline ϕ for the SiC/SiC CMC engine case and four lab cases using Ti64 with film cooling removed

material in the cases with air freestream at 350 K and coolant at 300 K. Figure 107 shows the effect of using an ideal anisotropic material with matched Bi instead in Case 2. Overall, there is

less than $\phi < 0.05$ difference between Ti64 and the ideal material, though the matched Bi case has slightly lower ϕ, by less than one contour level. If another case were run with film cooling removed and the matched Bi material, then it's reasonable to expect that both the blue lines in Figure 106 would move down and more closely match the engine condition. Overall, the differences between the NRMSD values and Figure 103 show the importance of matching both η and *Bi* in scaling ϕ. Though a lab condition with low NRMSD is important, ϕ will not be scaled if η and *Bi* are not also matched. *Bi* effects dominate upstream of the first film cooling outlet and η effects dominate downstream, as shown by an adiabatic effectiveness contour, such as Figure 101.

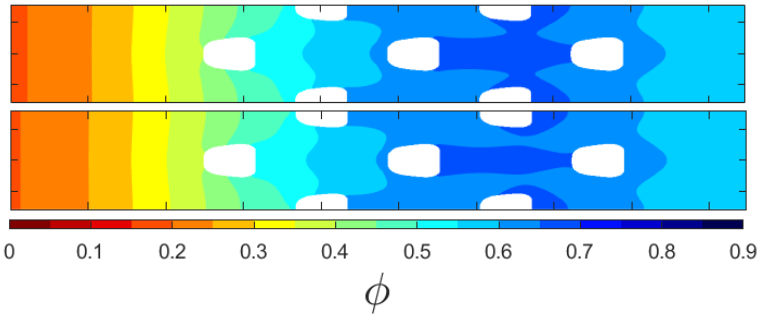

Figure 107: ϕ contours for air freestream at 350 K and CO_2 coolant at 300 K (top) Ti64 and (bottom) a notional matched Biot number material with anisotropic *k*

7.4. Summary

This chapter demonstrated a method for identifying testing conditions for conducting matched overall effectiveness experiments for both isotropic and anisotropic materials. The previous two chapters outlined the parameters necessary to scale the Biot number and the ratio of heat transfer coefficients. This chapter used that knowledge to make practical recommendations for how to conduct experiments for scaling overall effectiveness. These three chapters combined fully accomplish Objective 3.

8. Conclusions and Significance

The research described in this document shows numerous interesting conclusions about anisotropic thermal conductivity and scaling in film cooling. First, CFD was used to examine the effect of anisotropic thermal conductivity on ϕ on a flat plate and a leading edge. Next, this knowledge was leveraged to find ways to increase ϕ in film cooling by changing only the thermal conductivity tensor. Finally, analysis and CFD were utilized to determine the parameters important in scaling ϕ in anisotropic materials, and that knowledge was combined to find ideal conditions for conducting low temperature experiments. The following sections discuss conclusions and significance from each objective in-depth.

8.1. Objective 1: Characterize the effects of anisotropic thermal conductivity on overall cooling effectiveness

Chapter 3 addressed Objective 1 by rotating the thermal conductivity tensor of a flat plate so that heat was conducted in different directions to examine the effect of anisotropic thermal conductivity. In a physical sense, rotating the k tensor would be accomplished by stacking the composite layers in different orientations. It was found that simple one-axis rotations could have a profound effect on the overall effectiveness. Chapter 4 also focused on Objective 1 using a leading edge geometry. This geometry is more complex due to the showerhead film cooling design, compound angle film injection, and curvature which causes the layers to potentially be built in different orientations throughout the shape. The effect of anisotropic thermal conductivity on a leading edge was investigated by examining five different lay-up examples. Different forms of cooling were isolated to further investigate the effect of varying the *k* tensor. The results showed that lay-ups with tows running directly between the two surfaces and intersecting the coolant holes resulted in the highest cooling effectiveness.

8.2. Objective 2: Determine methods to increase the overall cooling effectiveness by varying the thermal conductivity tensor

Objective 1 is closely tied to the second objective and both Chapters 3 and 4 also address Objective 2. First, Chapter 3 satisfied Objective 2 through a compound two-axis rotation to find the optimal 2-axis orientation for the specific geometry. The optimized film cooled flat plate orientation has a $\phi = 0.048$ improvement over the baseline 0/90 lay-up. Moreover, the baseline case, representing the standard 0/90 lay-up technique for making CMC components, had nearly the worst orientation for cooling performance. This research provides an improved understanding of how to design CMC parts to maximize overall cooling effectiveness. To increase cooling performance in layered CMCs, designs should incorporate as many tows oriented in the through-thickness direction as possible to increase the effective thermal conductivity in the through-thickness direction. Conduction paths directly through the material and intersecting coolant holes lead to more effective cooling designs. Naturally, any recommendations based on cooling performance must also be evaluated in terms of manufacturability and structural performance which were out of the scope of the present research.

Chapter 4 also answered Objective 2 on a more complex geometry. As previously mentioned with Objective 1, like the flat plate, the highest cooling effectiveness was found using lay-ups with tows running directly between the two surfaces and intersecting the coolant holes. The high degree of curvature in the leading edge region can also result in a great deal of disparity in the overall cooling effectiveness for layups that are not curved with the leading edge but are instead aligned with a Cartesian coordinate system. For this reason, the importance of external film cooling can vary greatly over the surface of such a turbine blade in ways that would not be evident through traditional experimental and computational work involving only isotropic

thermal conductivity. If such geometries were to be used for structural reasons, for instance, designers should be aware of the thermal repercussions. Furthermore, the techniques used herein could be applied to industry-relevant geometries to tailor the film cooling design to the CMC layup. For instance, in regions where the layup design is not amenable to conductive cooling, additional film cooling holes could be implemented while fewer film cooling holes may be required in regions with conduction enhanced by CMC layers oriented perpendicular to the wall.

Together, the research addressing the first two objectives opens the door for turbine designers to incorporate CMC properties in a way never considered before. Previously, mechanical properties and reliability have been the sole focus for CMC gas turbine hot path components. Using this research, thermal optimization is an additional consideration for designers to enhance the film cooling performance of a part.

8.3. Objective 3: Identify scaling parameters and testing methodology for overall effectiveness experiments with isotropic and anisotropic thermal conductivity

Chapters 5-7 combined fulfilled Objective 3. First, in Chapter 5, the thermal conductivity of Inconel 718 and three composite materials was compared to air at a range of temperatures to determine the expected error in the Biot number in a low temperature experiment intended to determine the overall effectiveness. Computational simulations showed that low temperature experiments using turbine-relevant materials with low Biot numbers will overpredict the effect of internal cooling at engine conditions. While the effect of the 17% Biot number mismatch on ϕ is quite small (<0.025) for Inconel, it can be far more significant for composite materials. An 82-87% Biot number mismatch for the SiC/SiC material causes ϕ to be 0.2 higher on the upstream edge at lab condition. The overall effect of the mismatch is due to the anisotropic thermal conductivity not varying with temperature in the same manner as that of air. The result is

that the mismatch in Biot number in a low temperature experiment on a SiC/SiC component could contribute to a misleading ϕ value as much as 0.2 higher or 0.1 lower (depending on position) than the engine condition of interest to the experimentalist.

The temperature effect on Biot number is only part of the story. The lower gas temperature at lab conditions also affects matching χ, h/h_i, and to a lesser extent η, all of which also need to be matched to measure the correct overall effectiveness in a low temperature experiment. These fluidic effects tend to cause the ϕ distribution measured in a low temperature experiment to be up to approximately 0.1 lower than at engine conditions, partially offsetting the problems due to Biot number mismatch with CMC materials that are too low at experimental conditions in regions that are conduction dominated. In regions where film cooling dominates, this compounded an already negative error in predicted $\Delta\phi$ due to fluidic effects. The analysis with Inconel 718 shows that the errors from testing at low temperatures are due almost entirely to inherent mismatches in scaling fluidic effects, rather than Biot number mismatch.

This research shows that errors up to $\phi = 0.2$ are inevitable when testing composite materials at low temperatures due to mismatches in the Biot number because some of the conveniences of testing metal components at low temperatures don't apply to similar tests with composite materials. The experimentalist interested in predicting the behavior of CMC turbine components at high-temperature conditions is advised to exercise great care and a healthy degree of caution when interpreting experimental CMC data's applicability at a higher temperature than that at which it was acquired.

Next, Chapter 6 also resolved part of Objective 3. Experiments to measure overall effectiveness have seen an increase in use and it is well-recognized that in addition to selecting a coolant flow that would give rise to the appropriate adiabatic effectiveness, the thermal

conductivity of the solid material must be selected to ensure that the Biot number is also matched. Until now, however, little attention has been paid to the requirement that the ratio of the internal and external heat transfer coefficient distributions must also be matched. Since the coolant flow rate is usually selected such that a parameter such as the blowing ratio or the advective capacity ratio is matched, this means that the Reynolds number of the coolant is generally not matched in film cooling experiments. With Stanton number a function of the Reynolds number, the experimentalist cannot take it for granted that the ratio, $\frac{h}{h_i}$, is necessarily matched.

If the freestream Reynolds number is matched (as it almost always is in film cooling experiments) and the coolant flow rate is selected such that *ACR* is matched, then the heat transfer coefficient ratio depends upon the quantity $\frac{Pr_\infty^n}{Re_c^p Pr_c^q}$ being matched. Since the exponents, *n*, *p*, and *q*, are geometry and spatially dependent and most likely unknown, the practical implication is that Pr_∞, Pr_c, and Re_c must each be matched, individually. A low temperature experiment performed with air as the freestream would likely have a freestream Prandtl number rather closely matched to that at engine conditions; however, the same may not be said for Pr_c if a foreign gas is used for the coolant. Even with air as the coolant, the requirement to match Re_c over-constrains the problem. In the present work, this constraint is overcome by altering the fluid properties that were used in the computational simulations. In this way, the scaling theory was demonstrated to be correct, and a novel technique was demonstrated to overcome the difficulty that this over-constraint presents to the experimentalist who cannot alter individual fluid properties as desired. For instance, comparing a simple internal cooling simulation (even with no film cooling) between air coolant and CO_2 coolant, with matched ACR, show that the overall

effectiveness can differ by 0.04 between those two gases. Considering that both CO_2 and air are commonly used as coolants in gas turbine heat transfer experiments, this could be a source of error in overall effectiveness predictions. Additional problems can be encountered with film cooling where the introduction of foreign coolant into the external boundary layer alters the fluid properties on the hot gas side.

Chapter 7 fulfilled the final part of Objective 3. Ideal lab conditions for scaled overall effectiveness experiments to engine conditions were determined by minimizing the differences in parameters necessary to scale internal heat transfer. The relative influence of each of the parameters in NRMSD on overall effectiveness is not considered. Two ideal lab flow conditions and material were identified for a theoretical engine condition. CFD showed that these matched experiments accurately scaled the engine condition overall effectiveness within $\phi < 0.05$. Interestingly, cases with higher expected differences also matched the engine condition within $\phi = 0.07$. Further analysis showed that matching η and *Bi* has a large influence on ϕ. Overall, this research lays out the methodology for identifying test conditions and materials for any matched ϕ experiment.

8.4. Future Work

There are numerous topics for future work in this area. First, this research used 2D tow architecture for every anisotropic material. Additional work is needed on the effect of 3D architectures on heat transfer in film cooled regions. 3D architectures have thermally conductive tows in all three principal directions. These materials will have a different thermal conductivity tensor from the 2D materials examined in depth in Chapters 3 and 4 and could be optimized in another, unknown way.

Next, additional research should be conducted to determine the sensitivity of overall effectiveness to each parameter in NRMSD: Pr_c, Re_c, Pr_∞, and ξ. Now that the conditions necessary to scale each parameter are known, the relative importance of each must be determined. Without this piece, the problem is over-constrained and parameters such as NRMSD lack a strong basis. The relative importance for each parameter is likely geometry-dependent, but there is a potential for trends across a variety of film cooling geometries. There are several ways the sensitivity to each parameter could be identified and then used to calculate the likelihood of matching ϕ at engine condition. More research will help to fine-tune this important step forward.

Finally, experiments must be conducted to further examine the simulations conducted in this research. To examine the effects of anisotropic *k*, film cooled composite materials with various *k* tensors should be tested. Low and high temperature testing would be useful to refine the research done in Chapter 5 on scaling the Biot number on both isotropic and anisotropic materials. The two temperature experiments would also be useful to hone the work started in Chapter 7 on scaling internal cooling and overall effectiveness between two temperatures. These areas of future work will both deepen and broaden the research on the effect of anisotropic materials on scaled film cooled components.

This page is intentionally left blank

Appendix A: Computational Fluid Dynamics Procedure

This appendix covers some of the parameters used to prepare both geometries in this research. This section should prove useful to anyone interested in running conjugate heat transfer CFD in Fluent. All the models were meshed using Pointwise. Each geometry had at least three meshes: one was a standard mesh, the second had the plenum and hole walls separated, and the third had the film cooling hole outlets separated. The second and third meshes were used for the cases where plenum, hole, and film cooling were removed. In these cases, some walls needed to be assigned as a separate wall boundary. More unusual, when film cooling was removed, then the domain at the hole outlet was assigned two boundaries. To do this, the option to select connections was enabled. Next, the side of the hole outlet facing the film hole was assigned as an outlet. Then the opposite side of the outlet, facing the freestream, was assigned as a wall. The rest of the meshing process was ordinary for both geometries. The only other unusual mesh setup was zone type assignment. It was easiest to assign all the zones as fluid in Pointwise and later, correctly identify them as fluid or solid in Fluent. Once the mesh was created and the zone and boundary conditions assigned, the mesh was exported.

After importing the mesh into Fluent as a case file, the mesh was scaled, and zones were assigned as fluid or solid as appropriate. It was important to verify that the boundaries between the fluid and solid zones were split correctly during this process for fully conjugate heat transfer. Next, interface pairs were assigned, depending on the geometry used. When assigning interface zones, the translation or rotation distance was double-checked for each pairing. When auto-compute was used, Fluent tended to assign different values for different interfaces. After this, the mesh quality was checked and any locations with poor quality were fixed.

Next, the material conditions were set. First, if multiple species were used, such as air and CO_2, the mixing model was chosen. Models for each gas parameter (c_p, k, μ) were chosen because a constant value for any parameter in the mixing menu result in errors. The species were chosen using Fluent's built-in list, then each parameter was modified. The default values had to be modified for each condition, depending on the temperature and pressures at each inlet. The extraneous materials were deleted. The last gas on the mixture species list is Fluent's default if no other gas is chosen for an inlet, so air was always used as the final gas on the list. Next, the solid material thermal conductivity was set. For adiabatic and metallic materials, this was a constant value. However, for anisotropic material the orthotropic, cyl-orthotropic, or anisotropic material setting was used, depending on the coordinate system needed. If using the orthotropic coordinate system, then the primary and secondary axes were verified.

The next step was to set the boundary conditions. All the non-participating boundaries (like simulated tunnel walls) were set as either symmetry boundary conditions or adiabatic slip walls to prevent any boundary layers from interfering with the area of interest. The freestream inlet was set as a velocity inlet, calculated to match the freestream Reynolds number. The plenum coolant inlet was set as a mass flow inlet to match the desired coolant flow rate. The outlet was set as either an outlet or pressure-outlet, depending on the model. In the cases with plenum or hole cooling removed, then the designated walls were assigned zero heat flux. If film cooling is removed, then the freestream side of the wall boundary at the hole outlet was made adiabatic. The temperature boundary conditions were also set at each of the inlets. Finally, the overall pressure was set using the operating pressure instead of assigning the pressure at each inlet and outlet.

Next, the solver conditions were set. The realizable $k - \varepsilon$ model was used for both geometries. The exact wall functions depended on the model being used. Enhanced wall treatment was found to cause convergence issues if the mesh spacing was too small near the wall. It could only be used in models with larger wall mesh spacing. In the Solutions Methods menu, the standard scheme was used with Green-Gause Node Based spatial discretization. In the Solution Controls menu, temperature limits just above and below the inlet range greatly helped convergence. Finally, the simulations were initialized using hybrid initialization and solved until convergence was achieved. In some cases, especially those with very anisotropic materials, it was useful to solve the flow field first without the energy equation, then run additional iterations with the energy equation until convergence.

This page is intentionally left blank

Appendix B: Code for Calculating NRMSD

This code calculates the Normalized Root Mean Standard Deviation for a range of laboratory conditions. See Eqs. (7.5) and (7.6) for calculation details. The code needs input from prop.m, a function that outputs gas properties.

```
%% Engine Condition
Tc_e = 2000;
Tinf_e = 1000;
Pressure = 40;

Pamb_e = Pressure*101325;
Re_inf = 5000;
ACR = 0.5;

L = 0.00643;
A = 5*pi()*(L/2)^2;

% From CoolProp at 40 atm
rho_c_e = 13.94182728;
cp_c_e = 1144.583063;
mu_c_e = 4.34881E-05;
k_c_e = 0.068028617;

% From CoolProp at 40 atm
rho_inf_e = 7.009917021;
cp_inf_e = 1250.722667;
mu_inf_e = 6.81706E-05;
k_inf_e = 0.114644669;

Vinf_e = Re_inf*mu_inf_e/(rho_inf_e*L);
Prinf_e = mu_inf_e*cp_inf_e/k_inf_e;
Vc_e = ACR*rho_inf_e*cp_inf_e*Vinf_e/(rho_c_e*cp_c_e);
Rec_e = rho_c_e*Vc_e*L/mu_c_e;
Prc_e = mu_c_e*cp_c_e/k_c_e;
mdotc_e = rho_c_e*Vc_e*A;
ReR_e = Rec_e/Re_inf;
chi_e = mu_inf_e*cp_inf_e/k_c_e;

for h = 1:101
   Tinf = 195+h*5;
for j = 1:101
    Tc = 195+j*5;
Pamb = 101325;

for gas = 1 %Air_ = 1, Ar_ = 2, CO2_ = 3, He_ = 4, N2_ = 5, Xe_ = 6;
    %% Calculate Freestream Properties
    [rho_inf,cp_inf,k_inf,mu_inf] = prop(Tinf,Pamb,1);
    Vinf = Re_inf*mu_inf/(rho_inf*L);
    Prinf = mu_inf*cp_inf/k_inf;
```

```
    %% Calculate Coolant Properties
    [rho_c,cp_c,k_c,mu_c] = prop(Tc,Pamb,gas);
    Vc = ACR*rho_inf*Vinf*cp_inf/(rho_c*cp_c);

    Rec = rho_c*Vc*L/mu_c;
    Prc = mu_c*cp_c/k_c;
    Prinf = mu_inf*cp_inf/k_inf;
    ACR_ref = rho_c*cp_c*Vc/(rho_inf*cp_inf*Vinf);
    chi = mu_inf*cp_inf/k_c;
    I = rho_c*Vc*Vc/(rho_inf*Vinf*Vinf);

        Prinf_err(h,j) = (Prinf-Prinf_e)/Prinf_e;
        Rec_err(h,j) = (Rec-Rec_e)/Rec_e;
        Prc_err(h,j) = (Prc-Prc_e)/Prc_e;
        ACR_err(h,j) = (ACR_ref-ACR)/ACR;
        chi_err(h,j) = (chi-chi_e)/chi_e;
end

Tinf_store(h,j) = Tinf;
Tc_store(h,j) = Tc;
I_store(h,j) = I;

end
end

NRMSD = sqrt((Prc_err.^2 + Rec_err.^2 + Prinf_err.^2 +
chi_err.^2)/4)*100;

for i=1:size(NRMSD,1)
    for j=1:size(NRMSD,2)
        if NRMSD(i,j)>30
            NRMSD30(i,j)=NaN;
        else
            NRMSD30(i,j)=NRMSD(i,j);
        end
    end
end

figure
[n,n] = contourf(Tc_store(1,:),Tinf_store(:,1),NRMSD30);
set(n, 'LineStyle','none')
c = jet(6);
colormap(c)
caxis([0 30])
B = colorbar;
xlabel('T_c (K)')
ylabel('T_\infty (K)')
B.Label.String = 'NRMSD %';
axis square equal
grid on
```

Bibliography

[1] Gocha, April, "GE Aviation Invests Additional $105M to Manufacture Ceramic Matrix Composites for Jet Engines," Ceramics.org, 9 Mar 2018.

[2] Derber, Alex, "Rolls-Royce Invests in Ceramic Composites," MRO-Network.com, 14 Nov 2016.

[3] Haillan, Le, "Safran Inaugurates Ceramic Matrix Composites Research Center," Safran-Group.com, 6 Nov 2018.

[4] Perry, Dominic, "Honeywell Eyes CMC Materials for Helicopter Engines," FlightGlobal.com, 12 May 2016.

[5] Kiser, D., Almansour, A., Smith, C., Gorican, D., Phillips, R., Bhatt, R., & McCue, T., 2017, "Evaluation of CVI SiC/SiC Composites for High Temperature Applications," Conference presentation, *41st Annual Conference on Composites, Materials, and Structures*, Cocoa Beach, FL.

[6] Bogard, D.G. and Thole, K.A., 2006, "Gas Turbine Film Cooling," *Journal of Propulsion and Power*, **22**(2), 249-270.

[7] Albert, J. E. and Bogard, D. G., 2013, "Measurements of Adiabatic Film and Overall Cooling Effectiveness on a Turbine Vane Pressure Side with a Trench," *Journal of Turbomachinery*, **135**(9), 051007.

[8] Incropera, F. P., DeWitt, D. P., 2002, Fundamentals of Heat and Mass Transfer, 5th ed., John Wiley & Sons.

[9] Eberly, M. K., Thole, K. A., 2013, "Time-Resolved Film-Cooling Flows at High and Low Density Ratios," *Journal of Turbomachinery*, **136**(6), 061003.

[10] Greiner, N. J., Polanka, M. D., Rutledge, J. L., 2015, "Scaling of Film Cooling Performance from Ambient to Engine Temperatures," *Journal of Turbomachinery*, **137**(7), 1–11.

[11] Nathan, M. L., Dyson, T. E., Bogard, D. G., Bradshaw, S. D., 2014, "Adiabatic and Overall Effectiveness for the Showerhead Film Cooling of a Turbine Vane," *Journal of Turbomachinery*, **136**(3), pp. 310051–310059.

[12] Sinha, A.K., Bogard, D.G., Crawford, M.E., 1991, "Film-Cooling Effectiveness Downstream of a Single Row of Holes with Variable Density Ratio," *Journal of Turbomachinery*, **113**(7), 442-449.

[13] Haas, W., Rodi, W. Schönung, B., 1992, “The Influence of Density Difference Between Hot and Coolant Gas on Film Cooling by a Row of Holes: Predictions and Experiments,” *Journal of Turbomachinery*, **114**(4), October, 747-755.

[14] Rutledge, J.L, and Polanka, M.D., 2014, “Computational Fluid Dynamics Evaluations of Unconventional Film Cooling Scaling Parameters on a Simulated Turbine Blade Leading Edge,” *Journal of Turbomachinery*, **136**(10), 101006.

[15] Schroeder, R. P. & Thole, K. A., 2014, "Adiabatic Effectiveness Measurements for a Baseline Shaped Film Cooling Hole,” *ASME Turbo Expo 2014*, GT2014-25992.

[16] Fischer, J. P., McNamara L. J., Rutledge J. L., Polanka, M. D., 2020, “Scaling Flat Plate, Low-Temperature Adiabatic Effectiveness Results Using the Advective Capacity Ratio,” *Journal of Turbomachinery,* **142**(8), 081010.

[17] Fischer, J. P., 2018, “Influence of Coolant Flow Rate Parameters in Scaling Gas Turbine Cooling Effectiveness on a Flat Plate,” Master’s Thesis, Air Force Institute of Technology, Wright-Patterson AFB, OH.

[18] Rutledge, J.L., King, P.I., and Rivir, R.B., 2012, “Influence of Film Cooling Unsteadiness on Turbine Blade Leading Edge Heat Flux,” *Journal of Engineering for Gas Turbines and Power*, **134**(7), 071901.

[19] Pietrzyk, J.R., Bogard, D.G. and Crawford, M.E., 1990, “Effects of Density Ratio on the Hydrodynamics of Film Cooling,” *Journal of Turbomachinery,* **112**(3), 437-443.

[20] Stewart, W. R., Dyson, T. E., 2017, “Conjugate Heat Transfer Scaling for Inconel 718,” *ASME Turbo Expo 2017*, GT2017-64873.

[21] Polanka, M. D., Rutledge, J. L., Bogard, D. G., and Anthony, R. J., 2017, “Determination of Cooling Parameters for a High Speed, True Scale, Metallic Turbine Vane”, *Journal of Turbomachinery,* **139**(1), 011001.

[22] Terrell, E. J., Mouzon, B. D., & Bogard, D. G., 2005, “Convective Heat Transfer Through Film Cooling Holes of a Gas Turbine Blade Leading Edge,” *ASME Turbo Expo 2005*, GT2005-69003.

[23] Chavez, K., Slavens, T. N., & Bogard, D., 2016, “Effects of Internal and Film Cooling on the Overall Effectiveness,” *ASME Turbo Expo 2016*, GT2016-57992.

[24] Kays, W., Crawford, M., & Weigand, B., 2004 Convective Heat and Mass Transfer, 4th ed. McGraw-Hill.

[25] Jones, T.V., 1999, “Theory for the Use of Foreign Gas in Simulating Film Cooling,” *International Journal of Heat and Fluid Flow*, **20**(3), 349-354.

[26] Williams, R.P., Dyson, T.E., Bogard, D.G., Bradshaw, S.D., 2014, “Sensitivity of the Overall Effectiveness to Film Cooling and Internal Cooling on a Turbine Vane Suction Side,” *Journal of Turbomachinery*, **136**(3), p. 031006.

[27] Bryant, C. E. and Rutledge, J. L., 2020, “A Computational Technique to Evaluate the Relative Influence of Internal and External Cooling on Overall Effectiveness,” *Journal of Turbomachinery*, **142**(5), 051008.

[28] Wiese, C. J., Bryant, C. E., and Rutledge, J. L., 2022 “Flow Scaling Considerations for Coolant Warming,” *ASME Turbo Expo 2022*, GT2022-81510.

[29] McNamara, L.J., Anthony Fischer, J.P., Kernan, M., Rutledge, J.L., 2022, “Scaling Flat Plate Overall Effectiveness Measurements,” *ASME Turbo Expo 2022*, GT2022-81826.

[30] Simiriotis, N., 2016, “Large Eddy Simulation of the Film Cooling Flow System of Turbine Blades: Public Shaped Holes,” Master’s Thesis, Institut Superieur de l’Aeronautique et de l’Espace, Toulouse, France.

[31] DiCarlo, J.A., van Roode, M., 2006, “Ceramic Composite Development for Gas Turbine Engine Hot Section Components,” *ASME Turbo Expo 2006*, GT2006-90151.

[32] DiCarlo, J. A., 2013, “Advances in SiC/SiC Composites for Aero-Propulsion,” NASA/TM—2013-217889.

[33] Morscher, G. N., DiCarlo, J. A., Kiser, J. D. and Yun, H. M., 2010, “Effects of Fiber Architecture on Matrix Cracking for Melt-Infiltrated SiC/SiC Composites,” *International Journal of Applied Ceramic Technology*, **7**(3), 276-290.

[34] Lukaszewicz, D. H. -J. A., Ward, C., Potter, K. D., 2012, “The Engineering Aspects of Automated Prepreg Layup: History, Present and Future,” *Composites Part B: Engineering*, **43**(3), 997-1009.

[35] National Research Council, 1996, Accelerated Aging of Materials and Structures: The Effects of Long-Term Elevated-Temperature Exposure, Washington, DC: The National Academies.

[36] DiCarlo, J. A., Yun, H. M., Morscher, G. N., & Bhatt, R. T., 2004, “SiC/SiC Composites for 1200 °C and Above,” NASA/TM—2004-213048.

[37] Yang T., Wang L., Qui H., Wang X., Zhang D., & Qian K., 2020, "Bending Property and Damage Mechanism of Three-Dimensional Woven Angle Interlock SiC_f/SiC Composites," *Journal of Textile Research,* **41**(12), 73-80.

[38] Tian, T., Cole, K. D., 2012, "Anisotropic Thermal Conductivity Measurements of Carbon Fiber/Epoxy Composite Materials," *International Journal of Heat and Mass Transfer,* **55**(23), 6530-6537.

[39] Dasgupta, A., Agarwal, R. K., 1992, "Orthotropic Thermal Conductivities of Plain-Weave Fabric Composites Using Homogenization Technique," *Journal of Composite Materials*, **26**(18), 2736-2758.

[40] Sweeting, R. D., 2004, "Measurement of Thermal Conductivity for Fibre-Reinforced Composites," *Composites Part A: Applied Science and Manufacturing*, **35**(7-8), 933-938.

[41] Borca-Tasciuc, T., Chen, G., 2005, "Anisotropic Thermal Properties of Nanochanneled Alumina Templates," *Journal of Applied Physics*, **97**(8), 505-513.

[42] Özışık, M. N., 1980, Heat Conduction, 2nd ed., John Wiley & Sons.

[43] Onsagar, L., 1931, "Reciprocal Relations in Irreversible Processes I", *Physical Review,* **37**, 405-426.

[44] Onsagar, L., 1931, "Reciprocal Relations in Irreversible Processes II", *Physical Review,* **38**, 2265-2279.

[45] Casimir, H. B. G., 1945, "On Onsager's Principle of Microscopic Reversibility" *Reviews of Modern Phyics*, **17**, 343-350.

[46] Formalev, V. F., 2001, "Heat and Mass Transfer in Anisotropic Bodies," *Teplofizika Vysokikh Temperatur* **39**(5), 810-832.

[47] Appleby, M. P., Morscher, G. N., & Zhu, D., 2016, "Temperature Dependence of Electrical Resistance of Woven Melt-Infiltrated SiC_f/SiC Ceramic Matrix Composites," NASA/TM-2016-219095.

[48] Tu, Z., Mao, J., Jiang, H., Han, X., & He, Z., 2017, "Numerical Method for the Thermal Analysis of a Ceramic Matrix Composite Turbine Vane Considering the Spatial Variation of the Anisotropic Thermal Conductivity," *Applied Thermal Engineering*, **127**(25), 436-452.

[49] Tu, Z., Mao, J., & Han, X., 2017, "Numerical Study of Film Cooling Over a Flat Plate with Anisotropic Thermal Conductivity," *Applied Thermal Engineering*, **111**, 968-980.

[50] Tu, Z., Mao, J., Han, X., & He, Z. 2019, "Experimental Study of Film Cooling Over a Fiber-Reinforced Composite Plate with Anisotropic Thermal Conductivity," *Applied Thermal Engineering*, **148**, 447-456.

[51] Xu, Y., Kiochi, Y., 2004, "Automatic FEM Model Generation for Evaluating Thermal Conductivity of Composite with Random Materials Arrangement," *Computational Materials Science*, **30**(3), 242-250.

[52] Panton, R. L., 2013, Incompressible Flow, 4th Ed., John Wiley & Sons, Inc., Hoboken, New Jersey.

[53] Rutledge, J. L., Polanka, M. D., Bogard, D. G., 2016, "The Delta Phi Method of Evaluating Overall Film Cooling Performance," *Journal of Turbomachinery*, **138**(7), 071006.

[54] Deckers, J., Vleugels, J., & Kruth, J. P., 2014, "Additive Manufacturing of Ceramics: A Review," *Journal of Ceramic Science and Technology*, **5**(4), 245-260.

[55] Bryant, C. E., Wiese, C. J., Rutledge, J. L., Polanka, M. D., 2019, "Experimental Evaluations of the Relative Contributions to Overall Effectiveness in Turbine Blade Leading Edge Cooling." *Journal of Turbomachinery*, **141**(4), 041007.

[56] Ekkad, S. V., Ou, S., Rivir, R. B., 2004, "A Transient Infrared Thermography Method for Simultaneous Film Cooling Effectiveness and Heat Transfer Coefficient Measurements from a Single Test," *Journal of Turbomachinery*, **126**(4), 597-603.

[57] DiCarlo, J. A., van Roode, M., 2006, "Ceramic Composite Development for Gas Turbine Engine Hot Section Components," *ASME Turbo Expo 2006*, GT2006-90151.

[58] Boyle, R. J., Parikh, A. H., Nagpal, V. K., 2019, "Design Considerations for Ceramic Matrix Composite High Pressure Turbine Blades," *ASME Turbo Expo 2019*, GT2019-91787.

[59] Bryant, C. E., Rutledge, J. L., 2021, "Conjugate Heat Transfer Simulations to Evaluate the Effect of Anisotropic Thermal Conductivity on Overall Cooling Effectiveness," *Journal of Thermal Science and Engineering Applications*, **13**(6), 061013.

[60] Lemmon, E.W., Bell, I.H., Huber, M.L., McLinden, M.O., 2018, "NIST Standard Reference Database 23: Reference Fluid Thermodynamic and Transport Properties-REFPROP, Version 10.0, National Institute of Standards and Technology, Standard Reference Data Program".

[61] Publication Number SMC-045, Copyright © Special Metals Corporation, 2007.

[62] Sen, B., Schmidt, D. L., and Bogard, D. G., 1996, "Film Cooling with Compound Angle Holes: Heat Transfer," *Journal of Turbomachinery*, **118**(4), 800–806.

[63] Williams, R. P., Dyson, T. E., Bogard, D. G., and Bradshaw, S. D., 2014, "Sensitivity of the Overall Effectiveness to Film Cooling and Internal Cooling on a Turbine Vane Suction Side," *Journal of Turbomachinery*, **136**(3), 031006.

[64] Rubio, V, Ramanujam, P, Cousinet, S, LePage, G. Ackerman, T., Hussain, A., Brown, P., Dautremonte I., Binner, J., 2020, "Thermal Properties and Performance of Carbon Fiber-Based Ultra-High Temperature Ceramic Matrix Composites (C_f-UHTCMCs)," *Journal of the American Ceramic Society*, **103**(6), 3788– 3796.

[65] Mills-Brown, J., Potter, K., Foster, S., Batho, T., 2013, "Thermal and Tensile Properties of Polysialate Composites," *Ceramics International*, **39**(8) 8917-8924.

[66] Wiese, C. J., Rutledge, J. L., 2021, "The Effects of Specific Heat and Viscosity on Film Cooling Behavior," *Journal of Turbomachinery*, **143**(4), 041008.

[67] Wiese, C. J., Rutledge, J. L., Polanka, M. D., 2018, "Experimental Evaluation of Thermal and Mass Transfer Techniques to Measure Adiabatic Effectiveness with Various Coolant to Freestream Property Ratios," *Journal of Turbomachinery*, **140**(2), 021001.

[68] Shivpuri, R., 2004, "Advances in Numerical Modelling of Manufacturing Processes: Application to Steel, Aerospace and Automotive Industries," *Transactions of the Indian Institute of Materials*, 57(4): 345-366.

[69] "Hastelloy X Technical Data," https://www.hightempmetals.com/techdata/hitempHastXdata.php.

[70] Special Metals Corporation, 2007, "INCONEL Alloy 718", SMC-045, 1-28.

[71] Tleoubaev, A., Brzezinski, A., & Braga, L. C., 2004, "Accurate Simultaneous Measurements of Thermal Conductivity and Specific Heat of Rubber, Elastomers, and Other Materials," *12th Brazilian Rubber Tech. Congress.*

[72] Sweeney, P.C., Rhodes, J.F., 2000, "An Infared Technique for Evaluating Turbine Airfoil Cooling Designs," *Journal of Turbomachinery*, **122**(1), 170-177.

REPORT DOCUMENTATION PAGE

Form Approved
OMB No. 074-0188

PLEASE DO NOT RETURN YOUR FORM TO THE ABOVE ADDRESS.

1. REPORT DATE *(DD-MM-YYYY)*	**2. REPORT TYPE**	**3. DATES COVERED** *(From – To)*
24-03-2022	Doctoral Dissertation	January 2018 – March 2022

TITLE AND SUBTITLE

Thermal Considerations for Film Cooling Materials with Anisotropic Thermal Conductivity

5a. CONTRACT NUMBER

5b. GRANT NUMBER

5c. PROGRAM ELEMENT NUMBER

6. AUTHOR(S)

Bryant, Carol E., Captain, USAF

5d. PROJECT NUMBER

5e. TASK NUMBER

5f. WORK UNIT NUMBER

7. PERFORMING ORGANIZATION NAMES(S) AND ADDRESS(S)

Air Force Institute of Technology
Graduate School of Engineering and Management (AFIT/EN)
2950 Hobson Way
WPAFB OH 45433-7765

8. PERFORMING ORGANIZATION REPORT NUMBER

AFIT-ENY-DS-22-M-281

9. SPONSORING/MONITORING AGENCY NAME(S) AND ADDRESS(ES)

Air Force Research Lab, Turbine Engine Division, Turbomachinery Branch
Dr. Andrew T. Lethander
1950 5th St
Wright-Patterson AFB, OH 45433
Andrew.Lethander@us.af.mil

10. SPONSOR/MONITOR'S ACRONYM(S)

AFRL/RQTT

11. SPONSOR/MONITOR'S REPORT NUMBER(S)

12. DISTRIBUTION/AVAILABILITY STATEMENT

Distribution Statement A. Approved for Public Release; Distribution Unlimited

13. SUPPLEMENTARY NOTES

14. ABSTRACT

Higher performance requirements and reduced core sizes are driving increases in turbine inlet temperature in gas turbine engines, surpassing the melting point of advanced materials. Newer materials, such as composites, are being introduced into the hot sections of gas turbine engines. Components in the hot section use film cooling to prevent melting. One unique aspect of some high-temperature composites is they have a bulk anisotropic thermal conductivity, therefore heat flow differs relative to traditional metallic components. Film cooling designs can be revolutionized by leveraging anisotropy in high-temperature materials. The purpose of this research is to examine thermal considerations for using materials with anisotropic thermal conductivity in film cooling designs. Results show that leveraging anisotropy in film cooling designs can improve cooling effectiveness without changing any other aspect of the cooling architecture. The research also identifies ideal laboratory conditions and materials for well-scaled, film cooled experiments using isotropic and anisotropic material.

15. SUBJECT TERMS

Film Cooling, Ceramic Matrix Composites, Scaling, Gas Turbine Engines

16. SECURITY CLASSIFICATION OF:			**17. LIMITATION OF ABSTRACT**	**18. NUMBER OF PAGES**	**19a. NAME OF RESPONSIBLE PERSON**
a. REPORT	**b. ABSTRACT**	**c. THIS PAGE**			Lt Col James L. Rutledge, AFIT/ENY
U	U	U	UU	183	**19b. TELEPHONE NUMBER** *(Include area code)* (937) 255-6565 x4734 James.Rutledge@afit.edu

Standard Form 298 (Rev. 8-98)
Prescribed by ANSI Std. Z39-18